RICE UNIVERSITY

Understanding Structure-Property Relationships for Palladium-Gold Nanoparticles as Colloidal Catalysts

by

Yu-Lun Fang

A THESIS SUBMITTED
IN PARTIAL FULFILLMENT OF THE
REQUIREMENTS FOR THE DEGREE

Doctor of Philosophy

APPROVED, THESIS COMMITTEE:

Michael S. Wong, Chair
Professor in Chemical and Biomolecular Engineering and Chemistry

Rafael Verduzco
Louis Owen Assistant Professor in Chemical and Biomolecular Engineering

Pedro J. J. Alvarez
George R. Brown Professor of Engineering in Civil and Environmental Engineering, Chair

Jeffrey T. Miller
Group Leader in Heterogeneous Catalysis, Chemical Sciences and Engineering Division, Argonne National Laboratory

HOUSTON, TEXAS
MAY 2011

ABSTRACT

Understanding Structure-Property Relationships for Palladium-Gold Nanoparticles as Colloidal Catalysts

by

Yu-Lun Fang

Bimetallic palladium-gold (PdAu) nanoparticle (NP) catalysts have been demonstrated for the better catalytic performance than monometallic Pd catalysts in various reactions; however, the enhancement mechanism is not completely clear for most reactions. This thesis addresses the investigation of PdAu NP catalysts with emphasis on the structure-property relationships in water-phase reactions, using hydrodechlorination (HDC) of trichloroethene (TCE) as the model reaction. Catalyzed TCE HDC is a potential approach for water pollution control, in which colloidal Pd-decorated Au NPs (Pd/Au NPs) are known to be significantly better catalysts than monometallic Pd ones.

X-ray absorption spectroscopy (XAS) of carbon-supported Pd/Au NPs with different surface Pd coverages verified their core-shell structure (Au-rich core and Pd-rich shell). Structure evolution was observed upon heat treatment, in which Pd was in the form of surface Pd ensembles at room temperature. The metals formed a surface PdAu alloy or a bulk PdAu alloy above 200 °C, as determined from the average coordination environment. Results suggested a new way to promote Pd catalysis, namely, by impregnating supported Pd catalysts with gold salt followed by thermal annealing; such post-impregnation with different heat treatments could lead to >15-fold increase in TCE HDC activity.

Pd ensembles on the Au NP surface were demonstrated to be major active sites for TCE HDC as the reaction rates correlated strongly with the size of Pd ensembles determined from XAS. The geometric effect, in which atomic ensembles act as active sites, appeared to dominate over the mixed metal site effect and the electronic effect. Au NPs could stabilize surface Pd atoms in the metallic form, possibly leading to a set of highly active sites that is not present in monometallic Pd NPs.

The TCE HDC reaction with Pd/Au NPs and Pd NPs was conducted as a closed batch system. Mass transfer effects in this three-phase reaction were assessed and quantified by analyzing observed reaction rates as functions of stirring rates and initial catalyst charges. The largest effect on observed reaction rates came from gas-liquid mass transfer. TCE HDC was modeled as a Langmuir-Hinshelwood mechanism involving competitive chemisorption of dihydrogen and TCE molecules.

Acknowledgments

I would like to express my sincere gratitude to Prof. Michael S. Wong for being my thesis advisor. I have learned so much from him in every aspect to become a better human being. All praise goes to him if I could make any contribution in the future. I would like to express my great appreciation to Dr. Jeffrey T. Miller not only for being my committee member but also for his generous guidance on X-ray absorption spectroscopy and catalysis science. It has been always precious time for me to work or discuss with him. I would like to thank Prof. Pedro J. J. Alvarez for being my committee member and his expertise from environmental viewpoints. I would also like to thank Prof. Rafael Verduzco for being my committee member and very helpful discussion.

I would like to thank my colleagues in the Catalysis and Nanomaterials Laboratory for the wonderful experience during these years. To Dr. Kimberly N. Heck, Dr. William V. Knowles, Dr. Michael O. Nutt, Dr. Hitesh G. Bagaria, Dr. Jie Yu, Dr. Sukit Leekumjorn, Dr. Vinit S. Murthy, Dr. Subashini Asokan, Ms. Regina M. Yoo, Dr. M. Abbas Yaseen, and Dr. Zhiqing Yuan, I would like to thank you for all the project instruction, research discussion, experience sharing, and even career consultation. To Mr. Juan C. Velázquez Santana, Mr. Nikolaos Soultanidis, Ms. Lori A. Pretzer, Mr. Zhun Zhao, Dr. Nurgül Akçin, Mr. Ramsey J. Smith, Dr. Shyam B. Kadali, Mr. Gautam C. Kini, Mr. Quang X. Nguyen, Dr. Wen-Yin Ko, Dr. Xi Liang, and Dr. Shujing Li, I would like to thank you for all the research collaboration, experiment help, problem solving, and story sharing. The life in our group with all of you and many other members is unforgettable for me.

I would like to thank people at Rice University for helpful experiment assistance and inspiriting discussion, especially to Prof. Clarence A. Miller, Prof. Marc A. Robert, Prof. Qilin Li, Prof. Xianhuai Huang, Dr. Yu-Chang Tsai, Mr. Chun-Jen Lin, Dr. Ping Zhang, Dr. Haiping Lu, Dr. Tianmin Jiang, Dr. Xuan Guo, Mr. Ruiqiang Sun, Dr. Feng Li, Dr. Zheng Yang, Mr. Hao Sun, and Dr. Kai-Wei Liu.

I would like to acknowledge collaborators at several organizations. I thank Dr. Neng Guo and Dr. Tianpin Wu at Argonne National Laboratory for beamline experiments, data analysis, and insightful discussion. I thank Prof. Martin Reinhard, Mr. Gary D. Hopkins, and Dr. Sujie Qin at Stanford University for field testing and expertise in environmental engineering. I thank Dr. Xiankuan Zhang and Dr. Jillian Horn at SABIC Americas for sample providing and helpful discussion.

I would also like to acknowledge all the funding sources, which support the Catalysis and Nanomaterials Laboratory and my studies, including Rice University, Center for Biological and Environmental Nanotechnology (CBEN) at Rice University, Advanced Photon Source, Argonne National Laboratory, Department of Energy, National Science Foundation, Welch Foundation, SABIC Americas, World Gold Council, Mintek, DuPont, and 3M.

Finally, I would like to thank my family and friends for all the support. I thank my parents, Mr. Jui-Chang Fang and Ms. Yu-Ying Tsai, and my brother, Mr. Wei-Lun Fang, for their lifetime love and care. I thank all my friends at Houston, in the United States, in Taiwan, and in many other places for all the patience, help, and encouragement. I could not achieve anything without my family and friends.

To readers who might follow my work, thank you for reading my acknowledgments and good luck for your future research. I hope my thesis could provide some insight for you and lead to further advancement.

Yu-Lun Fang

May 2011

Table of Contents

List of Figures

List of Schemes

List of Tables

Chapter 1

Background and Research Overview

1.1. Bimetallic palladium-gold catalysis

Palladium-gold (PdAu) catalysts have been investigated for several decades; the PdAu system, like other bimetallic catalysts, attracts researchers' interest due to better catalytic performance, including activity, selectivity, and stability, than monometallic catalysts in various reactions [1-4]. The explanation of such bimetallic enhancement has been concluded as three different effects: (1) the geometric effect, in which atomic ensembles act as active sites; (2) the electronic effect, in which interaction among surrounding atoms gives rise to electron density dislocation; (3) the bifunctional effect, in which each metal promotes different reaction step [3-8]. For the PdAu system, the geometric effect (like Pd ensembles on Au surface, or PdAu mixed sites) [5, 6, 9-14] and/or the electronic effect [15-21] have been proposed as the dominant effects for many cases.

Pd itself, as one of the platinum group metals (PGMs), is well known for the broad range of catalytic applications [22, 23]. On the other hand, Au itself was considered as an inert metal till the 1980s when the research groups of Haruta and Hutchings re-discovered that Au nanoparticles (Au NPs) were catalytically active [24-27]. The group of Bond reported the earliest known observation of Au catalysis in 1973 [28].

The field of Au catalysis continues to grow and mature, representing the well-cited example of nanotechnology in catalysis [29-34].

PdAu catalysts have been used in the industrial process of vinyl acetate monomer (VAM) production since the 1970s [30, 35]. This is the first major industrial application of PdAu catalysts, and is the only known industrial catalytic application of Au. Studies of PdAu catalysts have focused on selective oxidation of hydrocarbons [6, 36-42], direct synthesis of hydrogen peroxide (H_2O_2) [32, 43, 44], fuel cells [45-49], and environmental pollution control [50-52].

1.2. Environmental issues of chlorinated hydrocarbons

Chlorinated hydrocarbons, a major category of the dense non-aqueous phase liquids (DNAPLs), are among the national list of toxic substances. Like other DNAPL compounds, chlorinated hydrocarbons are usually hard to be removed from the contaminated groundwater because they can migrate deeply below the water table and dissolve slowly into groundwater for long-term contamination due to their high density and low solubility in water (Fig. 1.1) [53]. DNAPLs and chlorinated hydrocarbons have been significantly recognized by U. S. Environmental Protection Agency (USEPA) in Superfund Sites, as reflected in the CERCLA Priority List [54]. Superfund Sites are uncontrolled or abandoned places where hazardous waste is located; the CERCLA Priority List represents the priority of such hazardous substances for their high frequency, toxicity, and potential of human exposure at Superfund Sites. In the top thirty of the CERCLA Priority List, 21 substances fall into DNAPLs while 16 substances fall into chlorinated hydrocarbons, meaning that DNAPLs and chlorinated hydrocarbons really

need people's attention for clean-up (Table 1.1) [54]. On the other hand, contamination can also be found in corporate industrial sites due to leakage and improper disposal; moreover, in wells for drinking water. According to a national water quality assessment program by U. S. Geological Survey (USGS), DNAPLs or chlorinated hydrocarbons were found over regulatory levels in ~1% of total 3497 domestic and public wells [53], resulted from hydrogeologic transport (aquifer recharge from remote locations) or anthropogenic leakage (urban pollution) as shown in Fig. 1.2.

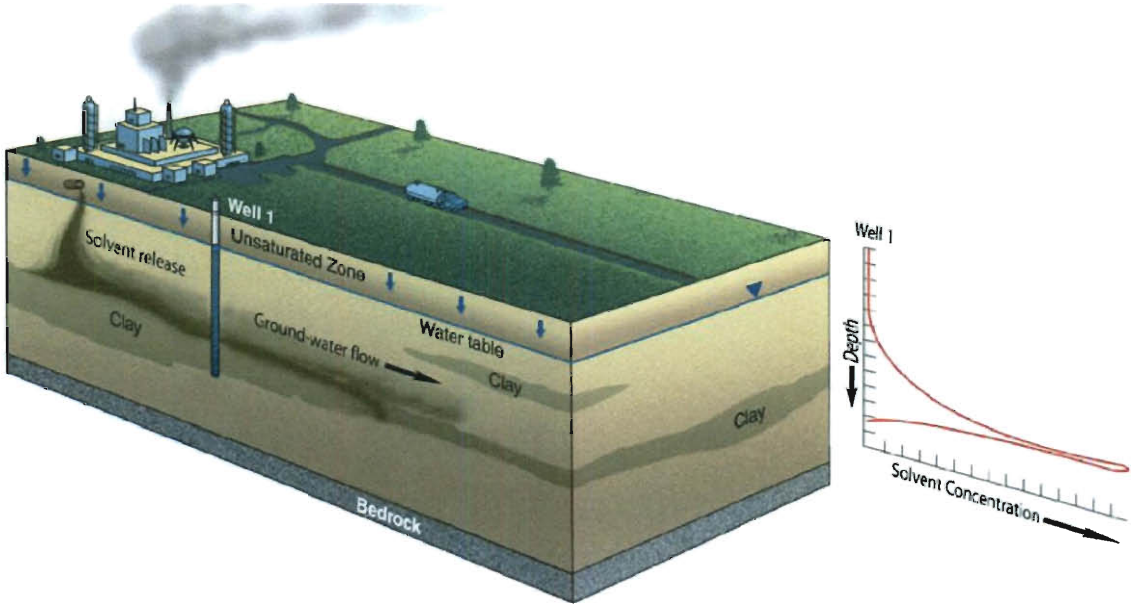

Figure 1.1. Distribution of DNAPL compounds in an aquifer [53].

Table 1.1. CERCLA Priority List of hazardous substances (top thirty only; bold: DNAPLs, italic: chlorinated hydrocarbons) [54].

Rank	Substance	Rank	Substance
1	Arsenic	16	***Trichloroethene***
2	Lead	17	***Dieldrin***
3	Mercury	18	Chromium, Hexavalent
4	*Vinyl Chloride*	19	Phosphorus, White
5	***Polychlorinated Biphenyls***	20	***Chlordane***
6	Benzene	21	***DDE, P,P'-***
7	Cadmium	22	***Hexachlorobutadiene***
8	**Polycyclic Aromatic Hydrocarbons**	23	**Coal Tar Creosote**
9	**Benzo(A) Pyrene**	24	***Aldrin***
10	**Benzo(B) Fluoranthene**	25	***DDD, P,P'-***
11	***Chloroform***	26	**Benzidine**
12	***DDT, P,P'-***	27	***Aroclor 1248***
13	***Aroclor 1254***	28	Cyanide
14	***Aroclor 1260***	29	***Aroclor 1242***
15	**Dibenzo(A,H) Anthracene**	30	***Aroclor***

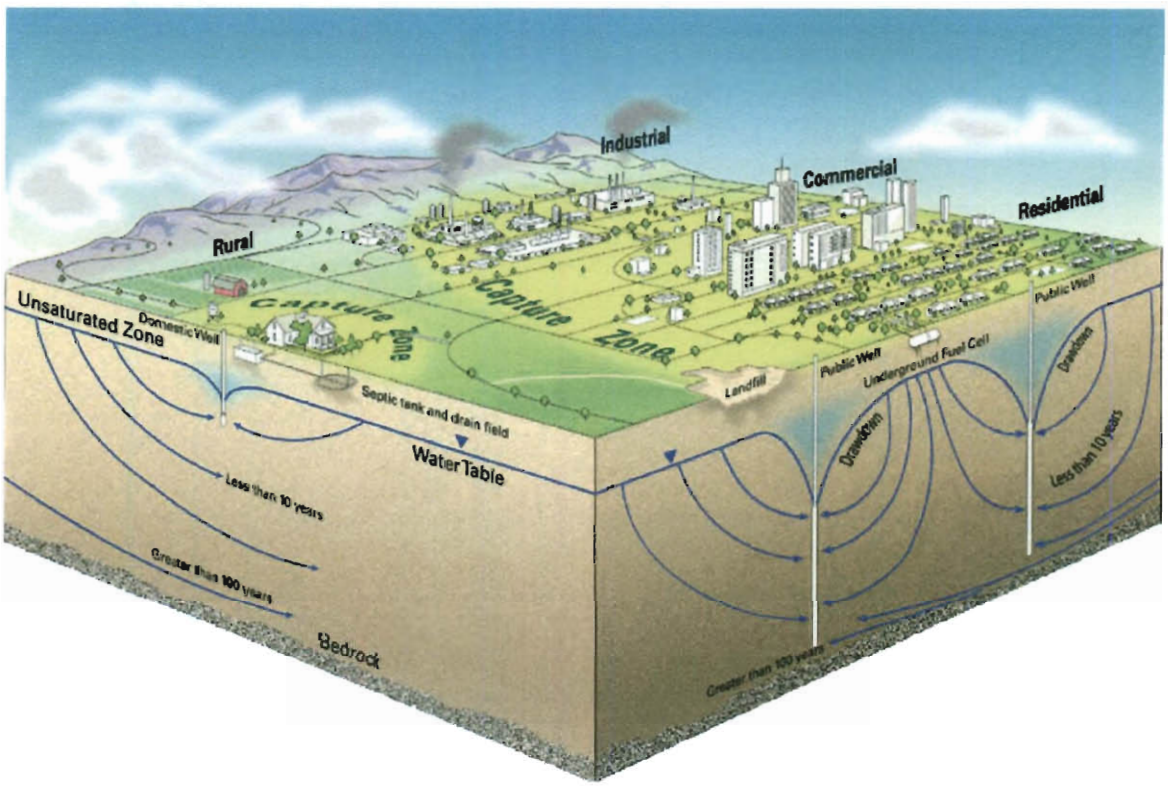

Figure 1.2. Groundwater transport due to hydrogeologic and anthropogenic effects, leading to quality change in domestic and public wells [53].

The Wong research group has investigated the remediation of chlorinated hydrocarbons in aqueous phase for several years, and trichloroethene (TCE, $ClHC{=}CCl_2$)

is one of the target compounds [51]. TCE is one of the most common hazardous organic contaminants found in groundwater, and has been ranked as the top twenty on the CERCLA Priority List for over ten years [54-59]. Typical uses of this chlorinated solvent include electronics manufacturing, metal degreasing, dry cleaning, and chemical intermediates. TCE has been widely produced and utilized around the world since the middle of the twentieth century; also has entered the subsurface through direct disposal, accidental spills, and leakage since then. According to USEPA Toxic Release Inventory, more than 42 million pounds of TCE were released to the environment during 1998-2001 [57]. Large exposure to TCE has been linked to liver damage, possible kidney effects, impaired pregnancies, childhood leukemia, and cancers in humans [59, 60]. USEPA has set Maximum Contaminant Level (MCL) for TCE in drinking water at a very low concentration, 5 ppb [61].

The catalytic remediation for TCE contaminated groundwater has been shown several advantages recently. While conventional methods, like carbon adsorption and air-stripping, can only move TCE from one phase to another [62], the catalytic remediation can reduce TCE into more benign hydrocarbons, leading to a more favorable process. The reaction of this kind of catalytic remediation is called as hydrodechlorination (HDC), which converts TCE to ethane or other non-chlorinated hydrocarbons. Pd is a well-known catalyst for HDC reactions [63-65]. Zhang and co-workers found that palladium-coated zero-valent iron (Pd/Fe) materials could enhance HDC reactions of TCE and other chlorinated compounds; the reaction rates were significantly higher than Fe materials alone [66, 67]. In their work, Fe was the reducing agent, and Pd was the catalyst. On the other hand, Kovenklioglu and co-workers found that supported Pd materials could

catalyze HDC reactions of various chlorinated compounds in aqueous phase at room temperature with hydrogen gas as the reducing agent [68]. Later, Reinhard and co-workers conducted series of HDC studies on TCE and other chlorinated compounds with palladium-supported alumina (Pd/Al_2O_3) in both laboratory and pilot-scale units [69-74]. Other research groups also provided further development of Pd-supported catalysts for groundwater remediation [75, 76].

The Wong group has developed new catalysts in order to improve the TCE HDC catalytic activity and efficiency in aqueous phase at room temperature with hydrogen gas [51]. In previous work, we utilized a bimetallic composition, colloidal Pd-decorated Au NPs (or Pd-on-Au NPs, Pd/Au NPs, Pd ensembles on the surface of Au NPs; ~20 nm), for aqueous-phase HDC reactions for the first time [50]. The Pd catalytic activity was increased significantly, compared to Pd/Al_2O_3 and even Pd NPs. Pd is known as an active catalyst for TCE HDC while Au is inert for it [70, 75-78]. Therefore, this promotion was not only due to the higher Pd dispersion but also related to the synergistic combination of Pd and Au, resulting from a geometric effect, an electronic effect, or both. In the following work, we synthesized Pd/Au NPs with a smaller diameter (~4 nm) for cost reduction, and showed Pd/Au NPs were at least one order of magnitude more active than monometallic Pd NPs, Pd/Al_2O_3, and Pd black on a per-Pd-atom basis for TCE HDC [79]. Pd/Au and Pd catalysts both showed >90% selectivity to ethane. Of note, we discovered that Pd/Au NPs exhibited a clear volcano-shape activity dependence on the surface Pd coverage (with the highest activity at 60-80% monolayer coverages, Fig. 1.3) [79]. Such results suggested that the geometric effect (Pd ensembles on the Au NP surface, or PdAu mixed sites) might be dominant since the volcano-shape dependence implied that the

special structure, Pd islands (atomic ensembles) on the Au NP surface, might be major active sites [79, 80]. Pd/Au also showed better deactivation resistance to chloride and sulfide species, which are common poisons for Pd-based catalysis [81].

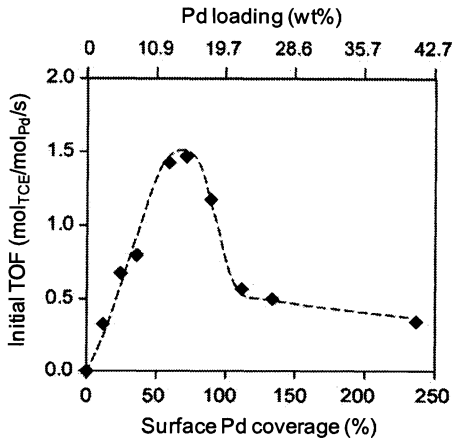

Figure 1.3. Reaction rate profile (initial turnover frequency, initial TOF) of TCE HDC with Pd/Au NPs, plotted against Pd loading and surface Pd coverage [79].

1.3. Research overview

In this thesis, following scientific issues and application approaches are addressed in order to understand structure-property relationships for bimetallic PdAu NP catalysts in water-phase reactions. TCE HDC has been chosen as the model reaction not only because of its environmental importance but also its mild reaction condition (room temperature, normal pressure, water phase), which could prevent further structure change during the reaction.

In Chapter 2, I describe the investigation into nanostructure of Pd/Au NPs. The as-synthesized Pd/Au NPs were confirmed, with X-ray absorption spectroscopy (XAS), to have a core-shell nanostructure, in which Pd was found as surface ensembles on the Au core. Au in Pd/Au NPs could impart oxidation resistance to Pd atoms. Results suggested

that these factors were sources for higher TCE HDC catalytic activity. I am the first-author on the paper published in 2011 in *Catalysis Today* entitled "Structural Analysis of Palladium-decorated Gold Nanoparticles as Colloidal Bimetallic Catalysts" [8].

In Chapter 3, I discuss a kinetics study of TCE HDC with colloidal Pd-based NPs (including Pd/Au NPs and Pd NPs). Mass transfer effects in a closed batch system were quantified by analyzing the observed reaction rates as functions of stirring rates and initial catalyst charges. The gas-liquid mass transfer was shown as the largest effect on observed reaction rates. The TCE HDC reaction was modeled as a Langmuir-Hinshelwood mechanism involving competitive chemisorption of dihydrogen and TCE molecules. Difference in adsorption affinities of the reactant molecules for the Pd/Au and Pd surfaces were suggested as responsible for the observed difference in TCE reaction order at high TCE concentrations, i.e., first-order for Pd/Au NPs and non-first-order for Pd NPs. I am the first-author on the paper published in 2011 in *ACS Catalysis* entitled "Kinetics Analysis of Palladium/Gold Nanoparticles as Colloidal Hydrodechlorination Catalysts" [82].

In Chapter 4, I describe the structure evolution of Pd/Au NPs and its relationship with catalytic activity. As-synthesized Pd/Au NPs possessed a core-shell (Au-rich core, Pd-rich shell) structure with Pd islands (atomic ensembles) on the shell. Such Pd islands on the Au NP surface would start to mix with Au to form surface PdAu alloy or full bulk PdAu alloy above 200 °C, depending on the surface Pd coverages. Pd islands on the Au NP surface were demonstrated to be major active sites for TCE HDC as the reaction rates changed with structure transition of Pd islands. Results supported that such geometric

effect dominated over other effects for Pd/Au NPs in the TCE HDC system. This work is in preparation for publication.

In Chapter 5, I discuss a new method to prepare supported bimetallic PdAu catalysts by impregnating gold salt to supported Pd catalysts with simple heating processes. Such post-impregnation of commercially available 1-wt% Pd-on-carbon (Pd/C) powder with chloroaurate salt, followed by different heat treatments, led to maximum TCE HDC activity with >15-fold increase. The relationships between catalyst structure and activity were proposed. This work is in preparation for publication.

In Chapter 6, I discuss possible directions for future work, including surface characterization, material visualization, in-situ observation, environmental practice, and further application.

1.4. References

[1] J.H. Sinfelt, Bimetallic Catalysts. Wiley, Hoboken, NJ, 1983.

[2] G.C. Bond, Chem. Soc. Rev. 20 (1991) 441-475.

[3] N. Toshima, T. Yonezawa, New J. Chem. 22 (1998) 1179-1201.

[4] R. Ferrando, J. Jellinek, R.L. Johnston, Chem. Rev. 108 (2008) 845-910.

[5] F. Maroun, F. Ozanam, O.M. Magnussen, R.J. Behm, Science 293 (2001) 1811-1814.

[6] M.S. Chen, D. Kumar, C.W. Yi, D.W. Goodman, Science 310 (2005) 291-293.

[7] J.K. Norskov, T. Bligaard, J. Rossmeisl, C.H. Christensen, Nature Chemistry 1 (2009) 37-46.

[8] Y.-L. Fang, J.T. Miller, N. Guo, K.N. Heck, P.J.J. Alvarez, M.S. Wong, Catal. Today 160 (2011) 96-102.

[9] C.J. Baddeley, R.M. Ormerod, A.W. Stephenson, R.M. Lambert, J. Phys. Chem. 99 (1995) 5146-5151.

[10] C.J. Baddeley, M. Tikhov, C. Hardacre, J.R. Lomas, R.M. Lambert, J. Phys. Chem. 100 (1996) 2189-2194.

[11] A.W. Stephenson, C.J. Baddeley, M.S. Tikhov, R.M. Lambert, Surf. Sci. 398 (1998) 172-183.

[12] T. Wei, J. Wang, D.W. Goodman, J. Phys. Chem. C 111 (2007) 8781-8788.

[13] V.I. Parvulescu, V. Parvulescu, U. Eudruschat, G. Filoti, F.E. Wagner, C. Kubel, R. Richards, Chem.-Eur. J. 12 (2006) 2343-2357.

[14] R.J. Behm, Z. Phys. Chemie-Int. J. Res. Phys. Chem. Chem. Phys. 223 (2009) 9-36.

[15] P.A.P. Nascente, S.G.C. Decastro, R. Landers, G.G. Kleiman, Phys. Rev. B 43 (1991) 4659-4666.

[16] B.E. Koel, A. Sellidj, M.T. Paffett, Phys. Rev. B 46 (1992) 7846-7856.

[17] B. Hammer, Y. Morikawa, J.K. Norskov, Phys. Rev. Lett. 76 (1996) 2141-2144.

[18] A. Ruban, B. Hammer, P. Stoltze, H.L. Skriver, J.K. Norskov, J. Mol. Catal. A-Chem. 115 (1997) 421-429.

[19] A. Roudgar, A. Gross, Phys. Rev. B 67 (2003).

[20] D.I. Enache, J.K. Edwards, P. Landon, B. Solsona-Espriu, A.F. Carley, A.A. Herzing, M. Watanabe, C.J. Kiely, D.W. Knight, G.J. Hutchings, Science 311 (2006) 362-365.

[21] J.G. Chen, C.A. Menning, M.B. Zellner, Surf. Sci. Rep. 63 (2008) 201-254.

[22] G. Ertl, H. Knözinger, F. Schüth, J. Weitkamp (Ed.), Handbook of Heterogeneous Catalysis. Wiley, Weinheim, Germany, 2008.

[23] H.U. Blaser, A. Indolese, A. Schnyder, H. Steiner, M. Studer, J. Mol. Catal. A-Chem. 173 (2001) 3-18.

[24] M. Haruta, T. Kobayashi, H. Sano, N. Yamada, Chem. Lett. (1987) 405-408.

[25] M. Haruta, N. Yamada, T. Kobayashi, S. Iijima, J. Catal. 115 (1989) 301-309.

[26] G.J. Hutchings, J. Catal. 96 (1985) 292-295.

[27] B. Nkosi, N.J. Coville, G.J. Hutchings, J. Chem. Soc.-Chem. Commun. (1988) 71-72.

[28] G.C. Bond, P.A. Sermon, G. Webb, D.A. Buchanan, P.B. Wells, J. Chem. Soc.-Chem. Commun. (1973) 444-445.

[29] G.C. Bond, C. Louis, D.T. Thompson, Catalysis by Gold. Imperial College Press, London, UK, 2006.

[30] D.T. Thompson, Platinum Metals Rev. 48 (2004) 169-172.

[31] D.T. Thompson, Nano Today 2 (2007) 40-43.

[32] G.J. Hutchings, Chem. Commun. (2008) 1148-1164.

[33] O. Vaughan, Nat. Nanotechnol. 5 (2010) 5-7.

[34] W.C. Ketchie, Y.-L. Fang, M.S. Wong, M. Murayama, R.J. Davis, J. Catal. 250 (2007) 94-101.

[35] C.W. Corti, R.J. Holliday, D.T. Thompson, Top. Catal. 44 (2007) 331-343.

[36] W.C. Ketchie, M. Murayama, R.J. Davis, J. Catal. 250 (2007) 264-273.

[37] C. Della Pina, E. Falletta, L. Prati, M. Rossi, Chem. Soc. Rev. 37 (2008) 2077-2095.

[38] D. Wang, A. Villa, F. Porta, L. Prati, D.S. Su, J. Phys. Chem. C 112 (2008) 8617-8622.

[39] A. Villa, N. Janjic, P. Spontoni, D. Wang, D.S. Su, L. Prati, Appl. Catal. A-Gen. 364 (2009) 221-228.

[40] A. Villa, D. Wang, D.S. Su, G.M. Veith, L. Prati, Phys. Chem. Chem. Phys. 12 (2010) 2183-2189.

[41] J.S. McPherson, D.T. Thompson, Top. Catal. 52 (2009) 743-750.

[42] L. Kesavan, R. Tiruvalam, M.H. Ab Rahim, M.I. bin Saiman, D.I. Enache, R.L. Jenkins, N. Dimitratos, J.A. Lopez-Sanchez, S.H. Taylor, D.W. Knight, C.J. Kiely, G.J. Hutchings, Science 331 (2011) 195-199.

[43] J.K. Edwards, B. Solsona, E.N. N, A.F. Carley, A.A. Herzing, C.J. Kiely, G.J. Hutchings, Science 323 (2009) 1037-1041.

[44] J.C. Pritchard, Q. He, E.N. Ntainjua, M. Piccinini, J.K. Edwards, A.A. Herzing, A.F. Carley, J.A. Moulijn, C.J. Kiely, G.J. Hutchings, Green Chem. 12 (2010) 915-921.

[45] M.H. Shao, T. Huang, P. Liu, J. Zhang, K. Sasaki, M.B. Vukmirovic, R.R. Adzic, Langmuir 22 (2006) 10409-10415.

[46] J. Zhang, K. Sasaki, E. Sutter, R.R. Adzic, Science 315 (2007) 220-222.

[47] J.B. Xu, T.S. Zhao, S.Y. Shen, Y.S. Li, Int. J. Hydrog. Energy 35 (2010) 6490-6500.

[48] V. Mazumder, Y. Lee, S.H. Sun, Adv. Funct. Mater. 20 (2010) 1224-1231.

[49] C.J. Zhong, J. Luo, B. Fang, B.N. Wanjala, P.N. Njoki, R. Loukrakpam, J. Yin, Nanotechnology 21 (2010).

[50] M.O. Nutt, J.B. Hughes, M.S. Wong, Environ. Sci. Technol. 39 (2005) 1346-1353.

[51] M.S. Wong, P.J.J. Alvarez, Y.-L. Fang, N. Akçin, M.O. Nutt, J.T. Miller, K.N. Heck, J. Chem. Technol. Biotechnol. 84 (2009) 158-166.

[52] A. Garron, K. Lazar, F. Epron, Appl. Catal. B-Environ. 65 (2006) 240-248.

[53] J.S. Zogorski, J.M. Carter, T. Ivahnenko, W.W. Lapham, M.J. Moran, B.L. Rowe, P.J. Squillace, P.L. Toccalino, The Quality of Our Nation's Waters: Volatile Organic Compounds in the Nation's Ground Water and Drinking-water Supply Wells: U.S. Geological Survey Circular 1292. U.S. Geological Survey, Reston, VA, 2006.

[54] CERCLA Priority List of Hazardous Substances. Agency for Toxic Substances and Disease Registry, U. S. Department of Health and Human Services, Atlanta, GA, 2007.

[55] M.J. Moran, J.S. Zogorski, P.J. Squillace, Environ. Sci. Technol. 41 (2007) 74-81.

[56] H.H. Russell, J.E. Matthews, G.W. Sewell, Ground Water Issue, EPA/540/S-92/002. U. S. Environmental Protection Agency, Washington, DC, 1992.

[57] 2001 Toxics Release Inventory Public Data Release Report, 260-R-03-001. Office of Environmental Information, U. S. Environmental Protection Agency, Washington, DC, 2003.

[58] B.H. Kueper, G.P. Wealthall, J.W.N. Smith, S.A. Leharne, D.N. Lerner, An Illustrated Handbook of DNAPL Transport and Fate in the Subsurface, R&D Publication 133. Environment Agency, Almondsbury, Bristol, UK, 2003.

[59] C.S. Scott, V.J. Cogliano, Environ. Health Perspect. 108 (2000) 159-160.

[60] Toxicological Profile for Trichloroethylene. Agency for Toxic Substances and Disease Registry, U. S. Department of Health and Human Services, Atlanta, GA, 1997.

[61] 2006 Edition of the Drinking Water Standards and Health Advisories, 822-R-06-013. Office of Water, U. S. Environmental Protection Agency, Washington, DC, 2006.

[62] J.C. Crittenden, R.R. Trussell, D.W. Hand, K.J. Howe, G. Tchobanoglous, Water Treatment Principles and Design. Wiley, Hoboken, NJ, 2005.

[63] F.J. Urbano, J.M. Marinas, J. Mol. Catal. A-Chem. 173 (2001) 329-345.

[64] F. Alonso, I.P. Beletskaya, M. Yus, Chem. Rev. 102 (2002) 4009-4091.

[65] V.I. Kovalchuk, J.L. d'Itri, Appl. Catal. A-Gen. 271 (2004) 13-25.

[66] W.X. Zhang, C.B. Wang, H.L. Lien, Catal. Today 40 (1998) 387-395.

[67] H.L. Lien, W.X. Zhang, J. Environ. Eng.-ASCE 131 (2005) 4-10.

[68] S. Kovenklioglu, Z.H. Cao, D. Shah, R.J. Farrauto, E.N. Balko, Aiche J. 38 (1992) 1003-1012.

[69] C.G. Schreier, M. Reinhard, Chemosphere 31 (1995) 3475-3487.

[70] G.V. Lowry, M. Reinhard, Environ. Sci. Technol. 33 (1999) 1905-1910.

[71] W.W. McNab, R. Ruiz, M. Reinhard, Environ. Sci. Technol. 34 (2000) 149-153.

[72] G.V. Lowry, M. Reinhard, Environ. Sci. Technol. 34 (2000) 3217-3223.

[73] G.V. Lowry, M. Reinhard, Environ. Sci. Technol. 35 (2001) 696-702.

[74] N. Munakata, M. Reinhard, Appl. Catal. B-Environ. 75 (2007) 1-10.

[75] C. Schuth, N.A. Kummer, C. Weidenthaler, H. Schad, Appl. Catal. B-Environ. 52 (2004) 197-203.

[76] K. Mackenzie, H. Frenzel, F.D. Kopinke, Appl. Catal. B-Environ. 63 (2006) 161-167.

[77] J.C. Liu, F. He, E. Durham, D.Y. Zhao, C.B. Roberts, Langmuir 24 (2008) 328-336.

[78] S. Ordonez, B.P. Vivas, F.V. Diez, Appl. Catal. B-Environ. 95 (2010) 288-296.

[79] M.O. Nutt, K.N. Heck, P. Alvarez, M.S. Wong, Appl. Catal. B-Environ. 69 (2006) 115-125.

[80] V. Ponec, G.C. Bond, Catalysis by Metals and Alloys. Elsevier, Amsterdam, The Netherlands, 1995.

[81] K.N. Heck, M.O. Nutt, P.J.J. Alvarez, M.S. Wong, J. Catal. 267 (2009) 97-104.

[82] Y.-L. Fang, K.N. Heck, P.J.J. Alvarez, M.S. Wong, ACS Catalysis 1 (2011) 128-138.

Chapter 2

Structure Analysis of Palladium-decorated Gold Nanoparticles as Colloidal Bimetallic Catalysts

2.1. Introduction

Structure characterization of catalysts provides a key to understanding the observed catalytic properties with regard to their surface active sites [1-3]. For supported bimetallic catalysts, it is generally accepted that catalysis performance, activity, selectivity, and/or stability, can be enhanced compared to that of the supported monometallic catalysts due to the synergistic combination of the two metals (in the nominal form of bimetallic nanoparticles (NPs) on the support surface) [4-7]. Three common explanations have been proposed to account for the catalytic enhancement [8-16]: (1) the geometric effect, in which atomic ensembles act as active sites; (2) the electronic effect, in which interaction among surrounding atoms gives rise to electron density dislocation; (3) the bifunctional effect, in which each metal promotes a different step of the surface reaction. In principle, these proposed mechanisms should also apply to unsupported bimetallic NPs, but this class of catalysts has been much less studied [1-3].

Many spectroscopic and microscopic methods, such as electron microscopy, scanning probe microscopy, X-ray diffraction, energy disperse X-ray microanalysis, ultraviolet-visible, infrared, surface-enhanced Raman, X-ray photoelectron, Mössbauer, and nuclear magnetic resonance, have been used to determine the structure of bimetallic

NPs [1-3]. X-ray absorption spectroscopy (XAS) is a powerful technique to acquire detailed structural and electronic information on metallic NPs [17-19]. There are two regions of interest in an X-ray absorption spectrum: the X-ray absorption near-edge structure (XANES) and the extended X-ray absorption fine structure (EXAFS) regions. As the incident photon energy is near the absorption edge of an element, the XANES region can provide information about oxidation state, electron distribution, and site symmetry of the absorbing atom. The EXAFS region, where oscillatory absorption occurs at higher incident photon energy due to interference of the ejected photoelectron with electron waves back-scattered from surrounding atoms, provides structural information about neighboring atoms to the absorbing one. XAS, especially in the EXAFS region, has been applied for characterization of bimetallic nanoparticles for decades. Sinfelt and co-workers conducted comprehensive XAS studies on various supported bimetallic catalysts prepared through conventional metal salt impregnation techniques [20-24]. Toshima and co-workers as well as other researchers performed the early work on XAS of bimetallic NPs in colloidal (i.e., unsupported) and immobilized (i.e., supported) forms [25-36]. There has been increasing use of XAS to characterize bimetallic NPs in recent years, revealing several possibilities for the two metals to be distributed within a NP, for example, alloy [34, 37-41], core-shell [26, 37, 39-46], cluster-in-cluster [28, 47, 48], and multi-shell structures [2, 49].

Through this study, we analyzed the nanostructure of palladium-decorated gold NPs (abbreviated here as Pd-on-Au NPs or Pd/Au NPs) prepared in aqueous suspension. We previously showed that Pd/Au NPs were at least one order of magnitude more active than Pd NPs, Pd-on-alumina (Pd/Al_2O_3), and Pd black on a per-Pd-atom basis for the

room-temperature, aqueous-phase hydrodechlorination (HDC) of trichloroethene (TCE) [50, 51], which converts TCE to ethane as shown in Scheme 2.1.

$$ClHC{=}CCl_2 + 4\ H_2 \rightarrow H_3C{-}CH_3 + 3\ HCl$$

Scheme 2.1. TCE HDC overall reaction.

Pd/Au and Pd catalysts both exhibited >90% selectivity to ethane for TCE HDC reactions [51]. The presumptive nanostructure of the catalyst was a one-atom-thick Pd shell on 4-nm Au NPs, with maximum activity found for NPs partially covered by Pd atoms (with 60-80% Pd surface coverage). Based on batch kinetic studies and characterization results, we proposed that geometric and electronic effects could explain the catalytic enhancement. Through careful XAS measurement and analysis of Pd/Au NPs with 60% Pd coverage and comparison with Au NPs and Pd NPs, we confirmed the core-shell bimetallic structure in this work. By studying the effect of heat treatment, we found the Pd shell to be in the form of Pd ensembles on the Au NP surface. At ambient temperature, a portion of the Pd surface atoms remained metallic in the Pd/Au NPs while most of the surface atoms were oxidized in Pd NPs, suggesting that zero-valent Pd contributes to the higher catalytic activity of Pd/Au NPs. This work has been published in 2011 in *Catalysis Today* [52].

2.2. Experimental

2.2.1. Preparation of NP catalysts

Nanoparticles, including Au NPs, Pd/Au NPs, and Pd NPs, were prepared as previously reported [51]. For Au NPs, a gold salt solution was prepared by diluting 1 mL $HAuCl_4$

solution (0.236 M; $AuCl_3$ 99.99%, Sigma-Aldrich; $AuCl_3$ was dissolved in water at room temperature) in 80 mL Nanopure water (>18.0 MΩ-cm, Barnstead NANOpure Diamond). A second solution was prepared by dissolving 0.04 g trisodium citrate (>99.5%, Fisher), 0.05 g tannic acid (>99.5%, Sigma-Aldrich), and 0.018 g potassium carbonate (>99.5%, Sigma-Aldrich) in 20 mL Nanopure water. Both solutions were heated to 60 °C and kept at 60 °C for at least 5 min. The second solution was then added to the gold salt solution. The overall fluid was kept stirring vigorously, and was heated to boil for 20 min before the heat source was removed. The color of the heated overall fluid changed with time—from light yellow to reddish, brown, and finally dark brown. Au NPs in the final fluid were about 4-nm in diameter according to transmission electron microscopy (TEM), and the concentration was calculated to be 1.07×10^{14} NP/mL, assuming 100% reduction of Au salts.

Pd/Au NPs were prepared with Au NPs modeled as "magic clusters" with seven complete shells of Au atoms and an additional Pd shell of different coverages [51]. The magic cluster model describes atom stacking by the way of a central atom surrounded with closed shells of identical atoms, which is the same arrangement as the face-centered cubic (FCC) system [51, 53-55]. In this work, Pd/Au NPs with a 60% Pd surface coverage (= 0.6 monolayer = 0.6 ML) were chosen as a representative sample because of the highest activity. To prepare 0.6 ML Pd/Au NPs, 57 μL H_2PdCl_4 solution (0.00240 M), which was prepared by dissolving $PdCl_2$ (99.99%, Sigma-Aldrich) in 0.005 M $HCl_{(aq)}$ with moderate stirring, was mixed with 2 mL as-synthesized Au NP suspension (1.07×10^{14} NP/mL). The fluid was then bubbled with hydrogen gas (99.99%, Matheson) for 2 min, and left to age overnight at room temperature (RT, 22 ± 2 °C). Hydrogen gas served

as a reducing agent for Pd salts; as we previously reported [51], Pd(0) atoms would be deposited on the surface of Au NPs rather than forming Pd particles because the activation energy for heterogeneous nucleation is less than that for homogeneous nucleation [56].

For Pd NPs, the preparation was the same as Au NPs, except that the gold salt solution was replaced by the palladium salt solution, which was prepared by diluting 12 mL H_2PdCl_4 solution (0.00240 M) in 68 mL Nanopure water. The color of the heated overall fluid also changed with time, from light yellow to brown. Pd NPs in the final fluid were about 4-nm in diameter according to TEM, and the concentration was calculated to be 1.22×10^{14} NP/mL, assuming 100% reduction of Pd salts.

2.2.2. Catalyst characterization

2.2.2.1. Transmission electron microscopy (TEM)

Size distributions of the NP samples were determined by analysis of imaging with a JEOL 2010 transmission electron microscope. TEM samples were prepared by depositing NP suspension on a 200-mesh carbon/formvar TEM grid and air-dried at RT. Size distribution measurements were conducted with the *ImageJ* program [57]; 150 particles were counted for each sample. TEM was done with help from Dr. H. G. Bagaria.

2.2.2.2. X-ray absorption spectroscopy (XAS)

NPs were immobilized on carbon powder for XAS experiments. 0.2 g carbon powder (Vulcan XC-72, Cabot) was dispersed in 5 mL isopropanol (99.9%, Fisher) under ultrasonication for 5 min. A given NP suspension (Au NPs, 0.6 ML Pd/Au NPs, or Pd NPs) was added to the carbon powder dispersion, and resulting mixture was ultrasonicated for 30 min and then stirred for 2 hr. Afterward, the mixture was freeze-

dried at −50 °C with a vacuum pressure 0.066 mbar (Labconco FreeZone 4.5 L console freeze dry system) to generate NP-containing carbon powders (NP/C). This low-temperature freeze-drying process for NP immobilization increased the metal loadings in the final solid, allowing for better XAS signal-to-noise ratios without heat effects that would damage the bimetallic nanostructure. The final solid compositions for Au NP/C, 0.6 ML Pd/Au NP/C, and Pd NP/C were respectively 5 wt% Au, 5 wt% Au with 0.75 wt% Pd, and 1 wt% Pd, estimated from mass balance with the assumption that all Pd and Au contents in the system were deposited on the carbon support.

X-ray absorption measurements were carried out on the insertion-device beamline 10-ID-B of the Materials Research Collaborative Access Team (MRCAT) at the Advanced Photon Source at Argonne National Laboratory. A cryogenically cooled double-crystal Si (111) monochromator was used in conjunction with an uncoated glass mirror to minimize the presence of harmonics. The monochromator was scanned continuously during the measurements with data points integrated over 0.5 eV for 0.07 sec per data point. Measurements were made in transmission mode with the ionization chambers optimized for the maximum current with linear response (~10^{10} photons detected per sec) using a mixture of nitrogen and helium in the incident X-ray detector and a mixture of ~20% argon in nitrogen in the transmission X-ray detector. A gold or palladium foil spectrum was acquired simultaneously with each measurement for energy calibration.

The NP/C samples were pressed into a cylindrical holder with a thickness chosen to give a total absorbance (μx) at the Au L_{III} (11.918 keV) and Pd K (24.350 keV) edges of ca. 2.0, and an edge step ($\Delta\mu x$) of ca. 0.5. Samples were analyzed as-prepared in air,

He, or H_2 at RT. Separate samples were reduced at 100 °C, 250 °C, or 300 °C for 30 min in 4% H_2/He followed by He purge at 200 °C in a continuous-flow reactor cell (glass tube, length 18 in., diameter 0.75 in.) fitted at both ends with polyimide windows and stainless steel valves to isolate the reactor from the atmosphere. Purging of the reduced catalysts in He at 200 °C was sufficient to decompose any Pd-H that might have been present and to desorb chemisorbed H_2 molecules. All spectra were obtained at RT.

Experimental phase shifts and back-scattering amplitudes were obtained from reference compounds: $Pd(NH_3)_4(NO_3)_2$ (Aldrich) for Pd-O, Pd foil for Pd-Pd, and Au foil for Au-Au. Experimental data of Pd and Au foil were used to determine the best fit of Debye-Waller factors (DWF's) and amplitude reduction factors (S_o) for phase shifts and back-scattering amplitudes in the FEFF fitting [58]. Along with the bond distance for Au and Pd foil, these values were used for determining the Au-Pd and Pd-Au FEFF phase shifts and back-scattering amplitudes. Standard procedures based on the WINXAS97 software [58] were used to extract the data [59]. The coordination parameters were obtained by a least-square fit in k- and R-space of the nearest-neighbor, k^2-weighted Fourier transform (FT) data (k: photoelectron wave number). The data fitted equally well with both k^1 and k^3 weightings. For the bimetallic Pd/Au sample, the EXAFS fitting was verified that, within error, the data from both Pd and Au edges led to the same bond distances, the same DWF's, and self-consistent coordination numbers for Pd-Au and Au-Pd bonds [60].

2.2.3. Trichloroethene hydrodechlorination (TCE HDC) rate determination

NP suspensions were tested in batch reactors for TCE HDC reactions, performed according to the previous studies [51]. Nanopure water and a magnetic stir bar were

sealed in a screw-cap bottle (250 mL, Alltech) with PTFE-sealed threads and a PTFE-silicone septum. The initial water volume was controlled to make the final liquid volume 173 mL after addition of the nanoparticle suspension. Hydrogen gas was bubbled into the bottle for 15 min to displace dissolved oxygen and to fill the headspace with a hydrogen atmosphere (1 atm). Then 7 μL TCE (99.5%, Sigma-Aldrich) and 0.2 μL pentane (99.7%, Burdick and Jackson), as the internal standard, were injected into the sealed bottle. The overall solution was stirred for at least 3 hr to reach equilibrium. The initial TCE concentration in water was 50.9 ppm, far below the saturation concentration of 1200 ppm in water at 25 °C [61]. Afterward, at time $t = 0$, NP suspension (Au NPs, Pd/Au NPs, or Pd NPs) was injected into the reaction bottle stirred at 600 rpm. The reaction was monitored through headspace gas chromatography (GC) using an Agilent Technologies 6890N GC with a flame ionization detector (FID) and a 60/80 Carbopack B/1% SP-1000 packed column (Supelco 12487, Sigma-Aldrich). Gas samples were taken from the headspace (gas phase) of the reactor, and then injected into GC to determine quantities of TCE and other compounds (>90% selectivity to ethane [51]). Reaction rates were determined from change of TCE concentrations in the headspace. All the reactions were performed at room temperature; reactions were performed with NP suspensions and not with either NP/C or heat-treated NP/C samples.

2.3. Results and discussion

2.3.1. TEM analysis

TEM images provided particle size information for the monometallic Au, 0.6 ML Pd/Au, and monometallic Pd NPs (Fig. 2.1). The mean particle sizes (and relative standard

deviations) were similar and estimated to be 4.1 nm (24%), 4.2 nm (17%), and 4.1 nm (15%) for Au NPs, 0.6 ML Pd/Au NPs, and Pd NPs, respectively.

2.3.2. XAS analysis

The XANES spectra of Au NP/C at the Au edge in air, He, or H_2 (Fig. 2.2) were almost identical to that of Au foil (reference compound for Au-Au bond), indicating that the Au NPs were metallic with little oxidized Au. The k^2-weighted Fourier transform of EXAFS data for Au NP/C (Fig. 2.3) also gave no evidence for the presence of Au-O bonds (bond distance of 2.03 Å). The XANES spectra did not change after RT treatment in air, He, or H_2 or after reduction at 250 °C.

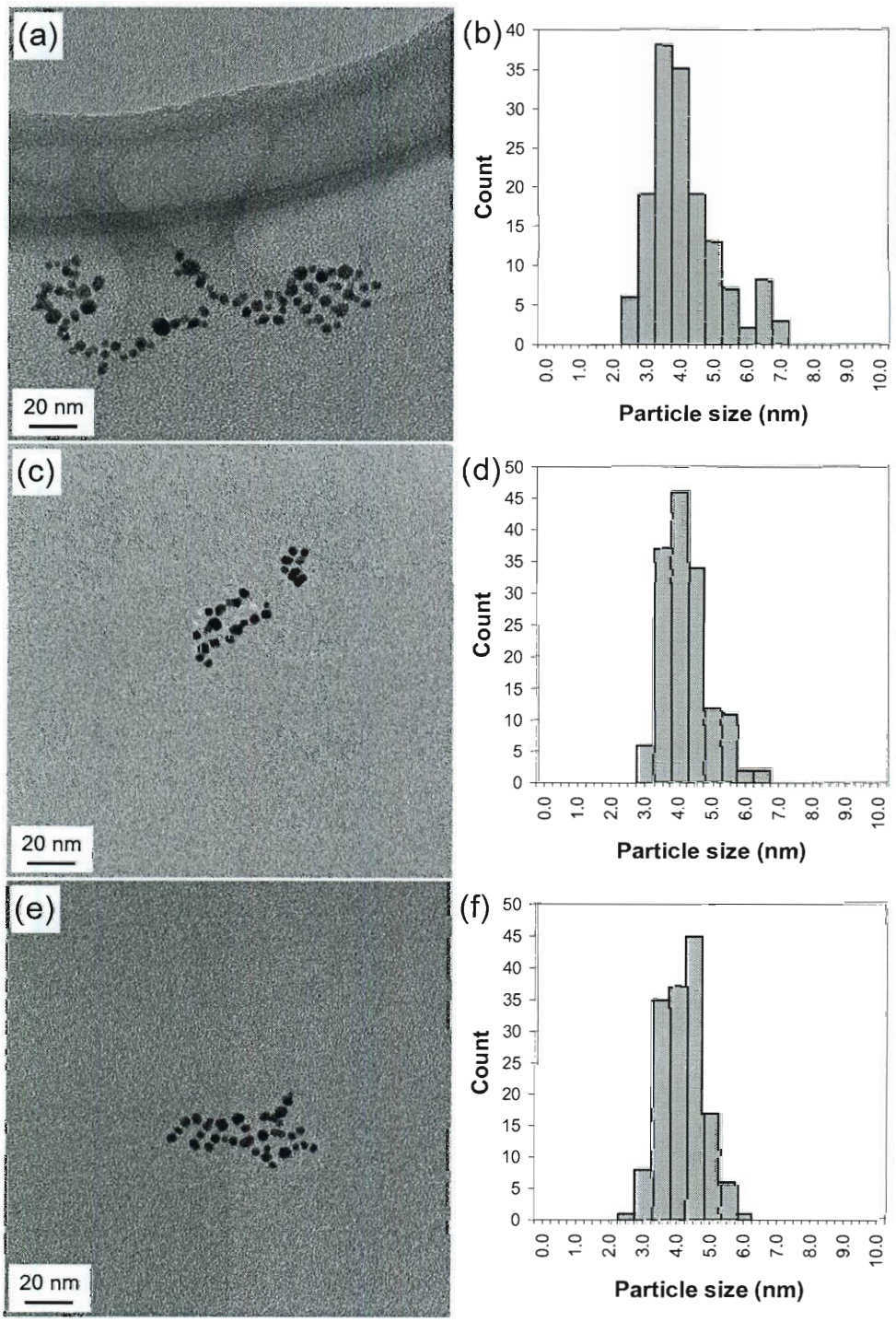

Figure 2.1. Representative TEM images and particle size histograms of (a, b) Au NPs, (c, d) 0.6 ML Pd/Au NPs, and (e, f) Pd NPs. A population of 150 NPs was analyzed for each NP sample. (Images by courtesy of Dr. H. G. Bagaria)

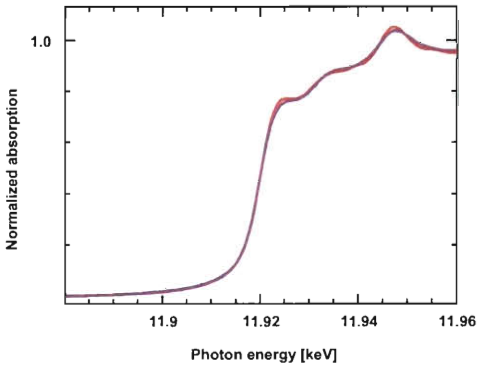

Figure 2.2. XANES spectra of Au foil (red) at RT and Au NP/C in air (blue), He (pink), and H_2 (green) at RT.

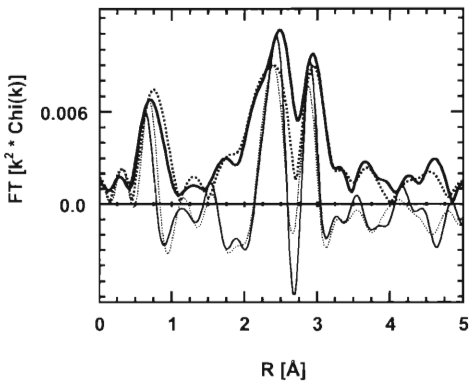

Figure 2.3. Fourier transform (k^2 weighted, Δk = 2.6-12.6 $Å^{-1}$) of Au L_{III} edge EXAFS data for Au NP/C and 0.6 ML Pd/Au NP/C, both after reduction at 250 °C: magnitude (solid thick) and imaginary components (solid thin) for Au NP/C; magnitude (dotted thick) and imaginary components (dotted thin) for Pd/Au NP/C (Δk: data length of k used for fitting).

Table 2.1 showed the results of EXAFS fitting. The Au-Au coordination number ($N_{Au\text{-}Au}$) of Au NP/C was about 10, and was estimated to correspond to approximately 5.5 nm particles [62]. This particle size was slightly larger than the 4.1 nm average diameter measured from TEM, which might be attributed to EXAFS being more sensitive to larger particles. The bond distance in the Au NPs was 2.86 Å, slightly less than that of Au foil (2.88 Å), which is typical of NPs. The Au-Au bond distance and coordination number did not change after RT treatment in air, He, or H_2 or after reduction at 250 °C (Table 2.1).

Table 2.1. EXAFS fit parameters (N: coordination number, R: bond distance, DWF: Debye-Waller factor, E_0: threshold absorption edge energy).

Sample	Edge	Treatment	Scattering path	N (±10%)	R (Å) (±0.02 Å)	DWF (10^3 Å^2)	E_0 (eV)
Au NP/C	Au	Air RT	Au-Au	10.2	2.86	1.0	-3.8
	Au	He RT	Au-Au	10.2	2.86	1.0	-3.7
	Au	H_2 RT	Au-Au	10.2	2.86	1.0	-3.8
	Au	H_2 100 °C	Au-Au	9.8	2.86	1.0	-3.9
	Au	H_2 250 °C	Au-Au	10.2	2.86	1.0	-3.7
Pd NP/C	Pd	Air RT	Pd-Pd	8.1	2.79	2.5	2.8
			Pd-O	1.3	2.05	2.0	1.5
	Pd	H_2 100 °C	Pd-Pd	7.4	2.81	2.5	2.1
			Pd-O	1.2	2.03	2.0	0.3
	Pd	H_2 300 °C	Pd-Pd	9.3	2.80	2.5	1.9
0.6 ML Pd/Au NP/C	Au	Air RT	Au-Au	9.7	2.85	1.0	2.4
			Au-Pd	1.5	2.80	1.0	3.0
	Au	He RT	Au-Au	9.8	2.85	1.0	2.3
			Au-Pd	1.3	2.80	1.0	3.6
	Au	H_2 RT	Au-Au	9.7	2.85	1.0	2.2
			Au-Pd	1.3	2.81	1.0	4.0
	Au	H_2 100 °C	Au-Au	9.6	2.84	1.0	2.2
			Au-Pd	1.3	2.79	1.0	3.9
	Au	H_2 250 °C	Au-Au	9.3	2.85	1.0	2.8
			Au-Pd	1.6	2.83	1.0	4.8
	Pd	Air RT	Pd-Pd	3.3	2.78	1.0	-3.0
			Pd-O	0.9	2.04	1.0	1.5
			Pd-Au	3.8	2.80	1.0	-2.1
	Pd	H_2 RT	Pd-Pd	2.8	2.77	1.0	-4.4
			Pd-O	0.6	2.04	1.0	2.0
			Pd-Au	4.2	2.78	1.0	-2.6
	Pd	H_2 100 °C	Pd-Pd	3.3	2.78	1.0	-4.0
			Pd-O	0.8	2.04	1.0	1.9
			Pd-Au	4.0	2.80	1.0	-1.8
	Pd	H_2 300 °C	Pd-Pd	2.0	2.76	1.0	-3.7
			Pd-Au	6.9	2.79	1.0	-3.2

The EXAFS of Pd NPs indicated partial oxidation in air at RT and in H_2 up to 100 °C. Fits of the oxidized catalysts gave a Pd-Pd coordination number ($N_{Pd\text{-}Pd}$ = 8.1) at a bond distance R = 2.79 Å and a Pd-O coordination number ($N_{Pd\text{-}O}$ = 1.3) at R = 2.05 Å. Since PdO has $N_{Pd\text{-}O}$ = 4, one can estimate the oxidized fraction from the coordination number. Approximately, one-third of the Pd atoms in a Pd NP were oxidized in air at RT,

i.e., 1.3/4 = 0.33, which is similar to the estimated dispersion of about 0.27 (calculated from dispersion $D = c/d$ (c is a constant 1.1 for Pd; d is the average particle size 4.1 nm from TEM.) [63, 64]. These values suggested that nearly all of the surface Pd atoms were oxidized in the monometallic Pd NPs.

Upon reduction at 300 °C, the Pd NPs were fully reduced and the estimated size from $N_{Pd\text{-}Pd}$ = 9.3 was 4.4 nm, in good agreement with the TEM-derived value of 4.1 nm. The Pd-Pd bond distance was 2.80 Å, which was larger than that in Pd foil (e.g., 2.75 Å), and similar to that in Pd-H [65]. These spectra were obtained in He after H_2 desorption at 200 °C without a change in the bond distance. Under the same conditions, supported Pd-H prepared by conventional methods is not stable, decomposing to metallic Pd with a bond distance of 2.75 Å [65]. The reason for these differences is not understood.

At the Au edge for the Pd/Au NPs, $N_{Au\text{-}Au}$ was 9.7 at R = 2.85 Å, which was very similar to that in the monometallic Au NPs, consistent with the Au core of Pd/Au NPs being similarly sized to monometallic Au NPs. Unlike the Au NPs, however, the EXAFS indicated the presence of a second scatter, i.e., from Au-Pd with $N_{Au\text{-}Pd}$ = 1.3 at 2.80 Å. There was negligible difference in the Au XANES or EXAFS for the 0.6 ML Pd/Au NP/C structure after contacting with air, He, or H_2 at RT (Table 2.1). However, upon reduction at 250 °C, there was a slight increase in the Au-Pd coordination number to 1.6. There was no evidence of oxidized Au in the Pd/Au NPs.

EXAFS of the Pd edge for 0.6 ML Pd/Au NP/C in air at RT and in H_2 up to 100 °C showed a significant peak near 1.5 Å (the uncorrected distance for Pd-O bond) and metallic peaks between 1.8-3.0 Å (Fig. 2.4). The EXAFS fits indicated that Pd has three coordination environments: metallic Pd ($N_{Pd\text{-}Pd}$ = 3.3 at 2.78 Å), metallic Au ($N_{Pd\text{-}Au}$

= 4.0 at 2.80 Å), and oxidized Pd^{2+} ($N_{Pd\text{-}O}$ = 0.8 at 2.04 Å) (Table 2.1). Within the error of the EXAFS measurements, the bond distances of Au-Pd ($R_{Au\text{-}Pd}$) and Pd-Au ($R_{Pd\text{-}Au}$) were identical, ca. 2.80 Å.

From the Pd-O coordination numbers, the fraction of oxidized atoms in the 0.6 ML Pd/Au NPs was estimated to be about 20% (~0.8/4.0) in air or after treatment in H_2 at 100 °C. Assuming nearly all the Pd atoms were located on the Au NP surface as Pd surface atoms, then most of the Pd atoms (~80%) were in the metallic form. Reduction at 300 °C led to complete reduction of Pd and an increase in the Pd-Au coordination number to 6.9, but a decrease in the Pd-Au coordination number to 2.0.

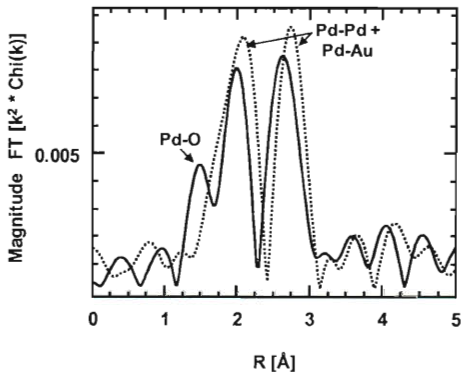

Figure 2.4. Fourier transform magnitude components (k^2 weighted, Δk = 2.8-10.5 $Å^{-1}$) of Pd K edge EXAFS data for 0.6 ML Pd/Au NP/C: in air at RT (solid line), after reduced in H_2 at 300 °C (dotted line).

A more complete analysis of metal coordination numbers provided insights into the Au and Pd distributions in the Pd/Au NPs. For the sample analyzed after treatment in air at RT, $N_{Au\text{-}Au}$ = 9.7 and $N_{Au\text{-}Pd}$ = 1.5, with the sum as the total Au coordination number of 11.2. The elemental composition was 5 wt% Au and 0.75 wt% Pd. At RT in air or H_2 at 100 °C, 80% (or 0.6 wt% Pd) was metallic. The molar composition of the reduced

metal was thus calculated as 82% and 18% for Au and Pd, respectively. If the Pd/Au NPs had a random, uniform distribution of Pd and Au atoms, the coordination number of Au with other Au atoms $N_{\text{Au-Au, bulk}}$ would be 9.2 (= 11.2 × 82%), and the coordination number of Au with other Pd atoms $N_{\text{Au-Pd, bulk}}$ would be 2.0 (= 11.2 × 18%). Since the measured $N_{\text{Au-Au}}$ was greater than $N_{\text{Au-Au, bulk}}$ and the measured $N_{\text{Au-Pd}}$ was less than $N_{\text{Au-Pd, bulk}}$, the Pd/Au NPs were concluded to have a Au-rich core (and a Pd-rich surface). The total absence of a small amount of Pd atoms within the Au core could not be ascertained.

From the Pd edge, $N_{\text{Pd-Au}}$ = 3.8 and $N_{\text{Pd-Pd}}$ = 3.3, giving a total Pd coordination number of 7.1. For a NP of Pd-Au uniform composition, the coordination number of Pd with Au atoms $N_{\text{Pd-Au, bulk}}$ would be 5.8 (= 7.1 × 82%) and the coordination number of Pd with other Pd atoms $N_{\text{Pd-Pd, bulk}}$ would be 1.3 (= 7.1 × 18%) (Fig. 2.5a). Since the measured $N_{\text{Pd-Au}}$ was less than $N_{\text{Pd-Au, bulk}}$ and the measured $N_{\text{Pd-Pd}}$ was greater than $N_{\text{Pd-Pd, bulk}}$, the NPs have a Pd-rich surface (Fig. 2.5b).

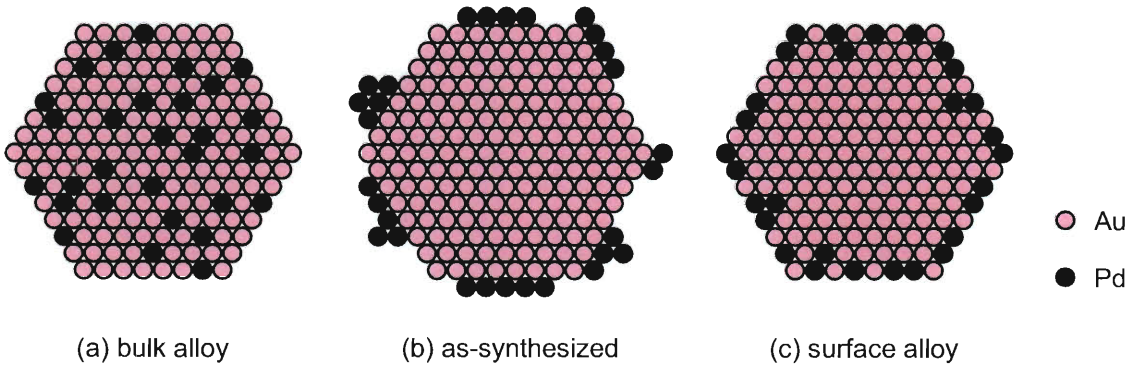

Figure 2.5. Idealized cross-sections of (a) a PdAu alloyed NP and core-shell nanostructures of a Pd/Au NP (b) in the as-synthesized form and (c) after reduction in H_2 at 300 °C.

All the oxidized Pd atoms in the carbon-supported Pd/Au NPs were reduced in H_2 at 300 °C. The metallic composition was re-calculated to be 78% and 22% for Au and Pd,

respectively. The total Au coordination number was 10.9, but the total Pd coordination number increased from 7.1 to 8.9. The coordination numbers for a NP of PdAu bulk composition were calculated as $N_{\text{Au-Au, bulk}}$ = 8.5, $N_{\text{Au-Pd, bulk}}$ = 2.4, $N_{\text{Pd-Au, bulk}}$ = 6.9, and $N_{\text{Pd-Pd, bulk}}$ = 2.0. $N_{\text{Au-Au}}$ EXAFS fit of 9.3 was greater than $N_{\text{Au-Au, bulk}}$ and $N_{\text{Au-Pd}}$ of 1.6 was less than $N_{\text{Au-Pd, bulk}}$. The Au EXAFS suggested there was some mixing of the Pd atoms with the Au; however, the core remained Au rich. By contrast, at the Pd edge, $N_{\text{Pd-Au}}$ was equal to $N_{\text{Pd-Au, bulk}}$ and $N_{\text{Pd-Pd}}$ was equal to $N_{\text{Pd-Pd, bulk}}$, suggesting that the NP surface underwent restructuring to give a composition similar to the bulk composition, i.e., a random and uniform composition (Fig. 2.5c). The difference in the state of Pd atoms before and after high-temperature treatment clearly showed the Pd atoms were located on the surface in the as-synthesized Pd/Au NPs [50, 51]. On the other hand, hydrogen chemisorption and infrared spectroscopy with CO as the probe molecule [66, 67] can indeed provide direct measurements of surface Pd atoms for comparison to EXAFS results. Such studies are currently underway.

2.3.3. TCE HDC catalytic activity comparison

Reaction rates of TCE HDC were determined as initial turnover frequency (TOF, number of reacted TCE molecules per surface Pd atom per sec), with the implicit assumption of first-order dependence in TCE and zero-order in H_2 [50, 51, 68, 69]. The kinetics is, in reality, more complicated at higher TCE concentrations for monometallic Pd catalysts [70]. Nevertheless, initial TOF's can be used to compare catalytic activities at a given TCE concentration and at an excess concentration of H_2. In accordance with our previous studies, Au NPs were found to be inactive, and the Pd-based NPs were active for the

HDC reaction (Table 2.2). On the basis of an equal amount of surface Pd atoms charged to the batch reactor, the Pd/Au NPs were 10 times more active than Pd NPs [51].

We performed TCE HDC reaction tests with colloidal NP suspensions for consistency with our previous works [50, 51, 71] rather than with immobilized NPs on carbon powders, which were used for XAS measurements. While the freeze-drying immobilization process is presumed to not affect NP structure due to its low temperature, the carbon support did influence the reaction kinetics due to loss of available active surface. In-depth analysis of NP/C catalysis and heat treatment effect on Pd-on-Au NP structure are underway.

Table 2.2. Results of catalytic testing for nanoparticle catalysts in aqueous-phase trichloroethene hydrodechlorination (initial $[TCE]_{(aq)}$ = 50.9 ppm, H_2 saturated in water and filled in the headspace (1 atm), stir rate 600 rpm, room temperature 22 ± 2 °C).

Nanoparticle catalysts tested	Pd weight loading (wt%)	Estimated Pd dispersion (% surface Pd atoms)	Calculated amount of surface Pd charged (nmol)	Initial TOF ($mol_{TCE}/mol_{surf\ Pd}/s$)
Au NPs	0	n/a	0	0
0.6 ML Pd/Au NPs	12.8	100[a]	60	1.44
Pd NPs	100	27[b]	47	0.15

[a] Pd atoms assumed to be fully accessible on Au NP surface.
[b] Calculated from dispersion $D = c/d$ (c is a constant 1.1 for Pd; d is the average particle size 4.1 nm from TEM.) [63, 64].

Despite the inexact model (in which the TCE HDC reaction is presumed to be first-order in TCE concentration for all catalysts) used to quantify reaction rate, the large difference in values indicated a remarkably beneficial effect of Au on Pd activity. Observing that the TCE HDC activity (on a per-Pd-atom basis) increased with Pd surface coverage until it reached a maximum at 60-80% surface coverage, we had previously speculated that 2-dimensional Pd ensembles were formed at the lowest surface coverages

before forming 3-dimensional Pd ensembles, which would have lowered Pd dispersion and therefore per-Pd-atom activity [51].

EXAFS analysis indicated the existence of monolayer-thin Pd clusters that were resistant to oxidation and mostly metallic under an ambient-temperature catalytic condition. We speculate that when Pd atoms are in contact with the metallic Au core, many, or perhaps all, of these remain metallic in air under conditions that the surface of Pd NPs is oxidized. Since the mild reaction conditions are insufficient to reduce these oxidized Pd, the Pd NP catalyst has low activity. We further speculate that higher Pd surface coverages in Pd/Au NPs lead to Pd multilayers, which easily get oxidized at an ambient temperature, contributing to lower activity at the higher surface coverages.

2.4. Conclusions

The bimetallic structure of Pd/Au NPs was characterized by TEM and XAS, and compared with Au NPs and Pd NPs. The Pd/Au NPs were found to be consistent with a core-shell model in which Pd atoms were located on the surface of a Au-rich core. Whereas the Pd/Au NPs had nearly all its Pd atoms as surface atoms and only ~20% of these were oxidized, the monometallic Pd NPs had 25-35% of its Pd atoms as surface atoms and nearly all of these were oxidized. Since the oxidized surface of the monometallic Pd NPs is not reduced under the mild reaction conditions, the metallic Pd atoms of the Pd/Au NPs are suggested to be active sites for the room-temperature, water-phase reaction of TCE HDC. Heat treatment of carbon-supported NPs at 300 °C was sufficient to break apart the Pd-rich surface ensembles into a randomly distributed composition at the NP surface. Au NPs appear to have a unique ability to stabilize surface

Pd atoms in metallic form, possibly leading to a set of highly active sites that is not present in monometallic Pd NPs under ambient-temperature reaction conditions.

2.5. References

[1] N. Toshima, T. Yonezawa, New J. Chem. 22 (1998) 1179-1201.

[2] R. Ferrando, J. Jellinek, R.L. Johnston, Chem. Rev. 108 (2008) 845-910.

[3] D. Astruc (Ed.), Nanoparticles and Catalysis. Wiley, Weinheim, Germany, 2008.

[4] G. Schmid, A. Lehnert, J.O. Malm, J.O. Bovin, Angew. Chem.-Int. Edit. Engl. 30 (1991) 874-876.

[5] A.M. Molenbroek, S. Haukka, B.S. Clausen, J. Phys. Chem. B 102 (1998) 10680-10689.

[6] A.E. Russell, A. Rose, Chem. Rev. 104 (2004) 4613-4635.

[7] C. Burda, X.B. Chen, R. Narayanan, M.A. El-Sayed, Chem. Rev. 105 (2005) 1025-1102.

[8] F. Maroun, F. Ozanam, O.M. Magnussen, R.J. Behm, Science 293 (2001) 1811-1814.

[9] R.J. Behm, Z. Phys. Chemie-Int. J. Res. Phys. Chem. Chem. Phys. 223 (2009) 9-36.

[10] V. Ponec, Appl. Catal. A-Gen. 222 (2001) 31-45.

[11] J.G. Chen, C.A. Menning, M.B. Zellner, Surf. Sci. Rep. 63 (2008) 201-254.

[12] M.S. Chen, D. Kumar, C.W. Yi, D.W. Goodman, Science 310 (2005) 291-293.

[13] T. Wei, J. Wang, D.W. Goodman, J. Phys. Chem. C 111 (2007) 8781-8788.

[14] B. Hammer, J.K. Norskov, Advances in Catalysis, Vol 45 45 (2000) 71-129.

[15] J.R. Kitchin, J.K. Norskov, M.A. Barteau, J.G. Chen, Phys. Rev. Lett. 93 (2004).

[16] J.K. Norskov, T. Bligaard, J. Rossmeisl, C.H. Christensen, Nature Chemistry 1 (2009) 37-46.

[17] J.T. Miller, M.K. Neylon, C.L. Marshall, A.J. Kropf, in: C.I. Contescu, K. Putyera, (Eds.), Dekker Encyclopedia of Nanoscience and Nanotechnology, CRC Press, Boca Raton, FL, 2004, 3953-3972.

[18] G. Vlaic, D. Andreatta, P.E. Colavita, Catal. Today 41 (1998) 261-275.

[19] G. Meitzner, Catal. Today 39 (1998) 281-291.

[20] J.H. Sinfelt, J. Catal. 29 (1973) 308-315.

[21] J.H. Sinfelt, Accounts Chem. Res. 20 (1987) 134-139.

[22] G. Meitzner, G.H. Via, F.W. Lytle, J.H. Sinfelt, J. Chem. Phys. 78 (1983) 882-889.

[23] G. Meitzner, G.H. Via, F.W. Lytle, J.H. Sinfelt, J. Chem. Phys. 78 (1983) 2533-2541.

[24] G. Meitzner, G.H. Via, F.W. Lytle, J.H. Sinfelt, J. Chem. Phys. 83 (1985) 4793-4799.

[25] N. Toshima, M. Harada, T. Yonezawa, K. Kushihashi, K. Asakura, J. Phys. Chem. 95 (1991) 7448-7453.

[26] N. Toshima, M. Harada, Y. Yamazaki, K. Asakura, J. Phys. Chem. 96 (1992) 9927-9933.

[27] M. Harada, K. Asakura, Y. Ueki, N. Toshima, J. Phys. Chem. 96 (1992) 9730-9738.

[28] M. Harada, K. Asakura, N. Toshima, J. Phys. Chem. 97 (1993) 5103-5114.

[29] M. Harada, K. Asakura, N. Toshima, J. Phys. Chem. 98 (1994) 2653-2662.

[30] D.G. Duff, P.P. Edwards, J. Evans, J.T. Gauntlett, D.A. Jefferson, B.F.G. Johnson, A.I. Kirkland, D.J. Smith, Angew. Chem.-Int. Edit. Engl. 28 (1989) 590-593.

[31] D. Richard, J.W. Couves, J.M. Thomas, Faraday Discuss. 92 (1991) 109-119.

[32] L.E. Aleandri, H. Bonnemann, D.J. Jones, J. Richter, J. Roziere, J. Mater. Chem. 5 (1995) 749-752.

[33] U. Kolb, S.A. Quaiser, M. Winter, M.T. Reetz, Chem. Mat. 8 (1996) 1889-1894.

[34] J.S. Bradley, G.H. Via, L. Bonneviot, E.W. Hill, Chem. Mat. 8 (1996) 1895-1903.

[35] A. Traverse, New J. Chem. 22 (1998) 677-683.

[36] A. Frenkel, Z. Kristall. 222 (2007) 605-611.

[37] S.N. Reifsnyder, H.H. Lamb, J. Phys. Chem. B 103 (1999) 321-329.

[38] C.R. Bian, S. Suzuki, K. Asakura, L. Ping, N. Toshima, J. Phys. Chem. B 106 (2002) 8587-8598.

[39] B.J. Hwang, L.S. Sarma, J.M. Chen, C.H. Chen, S.C. Shih, G.R. Wang, D.G. Liu, J.F. Lee, M.T. Tang, J. Am. Chem. Soc. 127 (2005) 11140-11145.

[40] M.R. Knecht, M.G. Weir, A.I. Frenkel, R.M. Crooks, Chem. Mat. 20 (2008) 1019-1028.

[41] S.M. Oxford, P.L. Lee, P.J. Chupas, K.W. Chapman, M.C. Kung, H.H. Kung, J. Phys. Chem. C 114 (2010) 17085-17091.

[42] R.J. Davis, M. Boudart, J. Phys. Chem. 98 (1994) 5471-5477.

[43] W.C. Ketchie, M. Murayama, R.J. Davis, J. Catal. 250 (2007) 264-273.

[44] C.H. Chen, L.S. Sarma, J.M. Chen, S.C. Shih, G.R. Wang, D.G. Liu, M.T. Tang, J.F. Lee, B.J. Hwang, ACS Nano 1 (2007) 114-125.

[45] P. Dash, T. Bond, C. Fowler, W. Hou, N. Coombs, R.W.J. Scott, J. Phys. Chem. C 113 (2009) 12719-12730.

[46] M.G. Weir, M.R. Knecht, A.I. Frenkel, R.M. Crooks, Langmuir 26 (2010) 1137-1146.

[47] K. Asakura, Y. Yamazaki, H. Kuroda, M. Harada, N. Toshima, Jpn. J. Appl. Phys. Part 1 - Regul. Pap. Short Notes Rev. Pap. 32 (1993) 448-450.

[48] M. Harada, H. Einaga, J. Colloid Interface Sci. 308 (2007) 568-572.

[49] D. Ferrer, A. Torres-Castro, X. Gao, S. Sepulveda-Guzman, U. Ortiz-Mendez, M. Jose-Yacaman, Nano Lett. 7 (2007) 1701-1705.

[50] M.O. Nutt, J.B. Hughes, M.S. Wong, Environ. Sci. Technol. 39 (2005) 1346-1353.

[51] M.O. Nutt, K.N. Heck, P. Alvarez, M.S. Wong, Appl. Catal. B-Environ. 69 (2006) 115-125.

[52] Y.-L. Fang, J.T. Miller, N. Guo, K.N. Heck, P.J.J. Alvarez, M.S. Wong, Catal. Today 160 (2011) 96-102.

[53] L.N. Lewis, Chem. Rev. 93 (1993) 2693-2730.

[54] J.M. Thomas, Pure Appl. Chem. 60 (1988) 1517-1528.

[55] T. Teranishi, M. Miyake, Chem. Mat. 10 (1998) 594-600.

[56] D. Kashchiev, G.M. van Rosmalen, Cryst. Res. Technol. 38 (2003) 555-574.

[57] ImageJ, v. 1.40 (http://rsb.info.nih.gov/ij/). National Institutes of Health, 2008.

[58] T. Ressler, J. Synchrot. Radiat. 5 (1998) 118-122.

[59] F.W. Lytle, D.E. Sayers, E.A. Stern, Physica B 158 (1989) 701-722.

[60] G.H. Via, K.F. Drake, G. Meitzner, F.W. Lytle, J.H. Sinfelt, Catal. Lett. 5 (1990) 25-33.

[61] R.P. Schwarzenbach, P.M. Gschwend, D.M. Imboden, Environmental Organic Chemistry. Wiley, Hoboken, NJ, 1993.

[62] J.T. Miller, A.J. Kropf, Y. Zha, J.R. Regalbuto, L. Delannoy, C. Louis, E. Bus, J.A. van Bokhoven, J. Catal. 240 (2006) 222-234.

[63] D. Roth, P. Gelin, A. Kaddouri, E. Garbowski, M. Primet, E. Tena, Catal. Today 112 (2006) 134-138.

[64] P. Castellazzi, G. Groppi, P. Forzatti, A. Baylet, P. Marecot, D. Duprez, Catal. Today 155 (2010) 18-26.

[65] M.W. Tew, J.T. Miller, J.A. van Bokhoven, J. Phys. Chem. C 113 (2009) 15140-15147.

[66] H.G. Lang, S. Maldonado, K.J. Stevenson, B.D. Chandler, J. Am. Chem. Soc. 126 (2004) 12949-12956.

[67] J. Rebelli, M. Detwiler, S. Ma, C.T. Williams, J.R. Monnier, J. Catal. 270 (2010) 224-233.

[68] G.V. Lowry, M. Reinhard, Environ. Sci. Technol. 33 (1999) 1905-1910.

[69] F.D. Kopinke, K. Mackenzie, R. Kohler, Appl. Catal. B-Environ. 44 (2003) 15-24.

[70] Y.-L. Fang, K.N. Heck, P.J.J. Alvarez, M.S. Wong, ACS Catalysis 1 (2011) 128-138.

[71] K.N. Heck, M.O. Nutt, P.J.J. Alvarez, M.S. Wong, J. Catal. 267 (2009) 97-104.

Chapter 3

Kinetics Analysis of Palladium/Gold Nanoparticles as Colloidal Hydrodechlorination Catalysts

3.1. Introduction

As an emerging field of interest during the past decade, nanoparticle (NP) catalysis encompasses chemical reactions catalyzed by NPs that are freely suspended in the liquid reaction medium or are supported on certain solids [1-3]. Examples of catalytic NP compositions include photocatalytic semiconductor metal oxides like TiO_2 [1, 4, 5], metal chalcogenides like CdSe ("quantum dots" [6-9]), and transition metals like Pd, Pt, and Rh [1-3, 6, 10]. As one of the extensively studied composition types, catalytic transition metal NPs have been investigated for both supported forms (including fuel cell reactions [11-14], and hydrogenation [15-17]) and suspended colloidal forms (including reduction [18-20], oxidation [21-25], hydrogenation [25-30], electron transfer reactions [31-33], and carbon coupling reactions [34-39]). So far, the colloidal form of catalytic NPs has been studied far less than the supported form, with the latter comprising the class of supported metal catalysts.

Colloidal transition metal NPs have uniform particle sizes typically in the 1-10 nm range; well-controlled composition; well-defined shape; kinetic colloidal stability; and reproducibility in synthesis [10, 40, 41]. Catalysis by such NPs, referred hereafter as colloidal NP catalysis or colloidal catalysis, has similarities to both heterogeneous and

homogeneous forms [2]. From the homogeneous point-of-view, these NPs can be dispersed and handled in solvents and characterized as molecular compounds by spectroscopic techniques [3, 18-20, 31-33, 42-44]; from the heterogeneous point-of-view, these NPs behave as metal solids with a defined particle surface [3, 11, 45]. As an added complication, catalysis can occur in solution due to metal leachate generated *in situ*, as has been established for Pd NPs in carbon coupling reactions [36-38].

Colloidal NPs can be considered a model material for the study of supported metal catalysis in which support effects are eliminated, e.g., mass transfer limitations and metal-support interactions [6]. NPs have no internal porosity and the active sites are located exclusively at the particle surface; so intra-particle diffusion is a non-issue. Very high stirring rates are used in the batch reactions, though the assumption of negligible external diffusion is not usually verified [21-23, 26-30, 46, 47]. The effect of stirring rate on measured reaction rates is the common method, but a more rigorous approach to analyzing the effects of mass transfer on colloidal NP catalysis is needed.

We develop such an approach in this work using palladium-decorated gold (or palladium-on-gold, Pd/Au) NPs as the colloidal catalytic material. Pd/Au NPs is highly active for the room-temperature aqueous-phase hydrodechlorination (HDC) of trichloroethene (TCE), perchloroethene, and other chlorinated compounds dissolved in water [48-50]. Pd is a well-studied catalyst for HDC reactions [51-53], especially for TCE [54-63]. TCE is of particular interest as one of the most common hazardous organic contaminants found in groundwater [64-69]. We showed that Pd/Au NPs were significantly more active than monometallic Pd catalysts, exhibiting maximum activity at sub-monolayer Pd coverages that was two orders of magnitude greater than Pd black on a

Pd atom basis. Au increased Pd catalytic activity through a likely combination of mixed site and electronic effects [50, 70-72], and further led to deactivation resistance to chloride and sulfide species, a common problem for Pd-based catalysis [73]. Au appeared to cause Pd to be more oxidation resistant compared to monometallic Pd [74]. Lab-scale flow reactor testing of immobilized Pd/Au NPs indicated a 20-fold decrease in materials cost compared to commercially available Pd/Al_2O_3 [48].

In this work, we present an experimental protocol for studying simultaneously the surface reaction and external mass transfer rates of Pd/Au NPs and Pd NPs for TCE HDC, which improves upon our earlier effort [50]. The effects of stirring rate and catalyst charge amount in a batch reactor were analyzed to determine the relative contributions of the possible mass-transfer resistances to surface reaction. A proposed Langmuir-Hinshelwood reaction pathway was found to be consistent with the rate data for Pd/Au NPs and Pd NPs, corrected for mass transfer resistances. The kinetic analysis presented here is general and adaptable to liquid-phase reactions catalyzed by colloidal NPs. This work has been published in 2011 in *ACS Catalysis* [75].

3.2. Experimental

3.2.1. Catalyst preparation

3.2.1.1. Monometallic NPs

Monometallic Au NPs and Pd NPs were synthesized in the way similar to our previous work [50]. For Au NPs, a gold salt solution was prepared by diluting 1 mL $HAuCl_4$ solution (0.236 M; $AuCl_3$ 99.99%, Sigma-Aldrich; $AuCl_3$ was dissolved in water at room temperature) in 80 mL Nanopure water (>18.0 MΩ-cm, Barnstead NANOpure Diamond).

A second solution was prepared by dissolving 0.04 g trisodium citrate (>99.5%, Fisher), 0.05 g tannic acid (>99.5%, Sigma-Aldrich), and 0.018 g potassium carbonate (>99.5%, Sigma-Aldrich) in 20 mL Nanopure water. Both solutions were heated to 60 °C and kept at 60 °C for at least 5 min before mixing together. The overall fluid was kept stirring vigorously, and was heated to boil for 20 min before removed from the heat source. As observed, the color of the heated overall fluid changed with time—from light yellow to reddish, brown, and finally dark brown. Au NPs in the final fluid were of 4-nm size in diameter according to transmission electron microscopy analysis reported previously [50, 74]. Elemental analysis, conducted on randomly selected, centrifuged NP samples using a PerkinElmer inductively coupled plasma optical emission spectrometer (ICP-OES) Optima 4300 DV, indicated >95% of Au salt precursor was in the NP form. We calculated the concentration of the final Au NP suspension to be 1.07×10^{14} NP/mL, based on 100% reduction of Au salts into NPs.

The procedure for Pd NPs was almost the same as for Au NPs, except for the gold salt solution substituted by a palladium salt solution. The palladium salt solution was prepared by diluting 12 mL H_2PdCl_4 solution (0.00240 M), which was prepared by dissolving $PdCl_2$ (99.99%, Sigma-Aldrich) in 0.005 M $HCl_{(aq)}$ at room temperature with moderate stirring, in 68 mL Nanopure water. The overall color of the heated fluid also changed with time, from light yellow to brown. Pd NPs in the final fluid were of 4-nm size in diameter according to transmission electron microscopy analysis reported previously [74]. ICP results generally indicated >95% of Pd salt precursor was in the NP form. We thus assumed 100% conversion of Pd salts, and calculated the concentration of the final Pd NP suspension to be 1.22×10^{14} NP/mL.

3.2.1.2. Bimetallic Pd/Au NPs

Pd/Au NPs were also synthesized as previously reported, with the NPs modeled as Au "magic clusters" with seven complete shells of Au atoms and a Pd shell of different coverages [50]. In the preparation of Pd/Au NPs with a 30% Pd surface coverage (= 0.3 monolayer = 0.3 ML), 28.5 μL H_2PdCl_4 solution (0.00240 M) was added to 2 mL Au NP suspension (1.07×10^{14} NP/mL) and mixed. The fluid was then bubbled with hydrogen gas (99.99%, Matheson) for 2 min, and left at room temperature (22 ± 2 °C) overnight. In the preparation of Pd/Au NPs with a 60% Pd surface coverage (= 0.6 ML), 57.0 μL H_2PdCl_4 solution (0.00240 M) was used instead. ICP results indicated >95% of Pd salt precursor was reduced and incorporated into the Pd/Au NPs. For calculation purposes, we assumed 100% conversion of Pd precursor.

3.2.2. Mass transfer catalytic experiments

In the batch reactor studies of TCE HDC, Nanopure water and a magnetic stir bar were sealed in a screw-cap bottle (250 mL, Alltech) with PTFE-sealed threads and a PTFE-silicone septum. The initial water volume was controlled so that the final liquid reaction volume was 173 mL after addition of the colloidal sol. Hydrogen gas was bubbled into the bottle for 15 min to displace dissolved oxygen and to fill the headspace with a hydrogen atmosphere (1 atm). All the reactions were performed at room temperature.

3.2.2.1. Pd/Au NP testing

After hydrogen bubbling, 3 μL TCE (99.5%, Sigma-Aldrich) and 0.2 μL pentane (99.7%, Burdick and Jackson), as the internal standard, were injected into the sealed bottle. The overall solution was stirred for at least 3 hr to reach equilibrium. Then at time $t = 0$, a specific volume of Pd/Au NP (0.3 ML) suspension (0.30, 0.60, 0.90 mL; 1.07×10^{14}

NP/mL) was injected into the reaction bottle at a set stirring rate (300, 600, 900 rpm). The reaction was monitored through headspace gas chromatography (GC) using an Agilent Technologies 6890N GC with a flame ionization detector (FID) and a packed column (length 1.83 m × O.D. 1/8 in. × I.D. 2.1 mm) containing 60/80 Carbopack B/1% SP-1000 (Supelco 12487, Sigma-Aldrich). The initial TCE concentration was 21.8 ppm in liquid and 3.49 ppm in gas—within the detectable FID range. TCE HDC reaction rates were determined by the initial slope of TCE concentration-time profiles within the first 5 min. Pd/Au NPs (0.6 ML) were tested in the same way but with half the NP suspension volumes (0.15 , 0.30, 0.45 mL) so that the charged Pd amount was kept the same.

3.2.2.2. Pd NP testing

Tests for Pd NPs were conducted slightly differently. After hydrogen bubbling, 0.3 μL TCE and 4 μL methylene chloride (99.9%, Fisher), as the internal standard, were injected into the sealed bottle. The overall solution was stirred for at least 3 hr to reach equilibrium. Then at time $t = 0$, a specific volume of Pd NP suspension (0.28, 0.56, 1.12 mL) was injected into the bottle at a set stirring rate (300, 600, 900 rpm). The reaction was monitored through headspace GC using an Agilent Technologies 6890N GC with a micro-electron capture detector (μ-ECD) and a capillary column (length 30 m × O.D. 320 μm × I.D. 0.25 μm) containing 5% phenyl methyl siloxane (HP-5, Agilent Technologies). The initial TCE concentration was 2.18 ppm in liquid and 0.349 ppm in gas—within the detectable ECD range but below the detection limit for FID. Methylene chloride was chosen as the internal standard because ECD is very sensitive to chlorine atoms. This molecule had no effect on the TCE HDC reaction [59], and did not undergo reactions (no concentration change) according to control experiments with 40 μL methylene chloride

under the same conditions. TCE HDC reaction rates were determined by the initial slope of TCE concentration-time profiles within the first 5 min.

3.2.3. Reaction mechanism experiments

For this study, the TCE HDC reaction was carried out at different initial TCE concentrations, using specified amounts of TCE and an internal standard. The internal standard was either methylene chloride (4 μL) if the initial TCE concentration in liquid $[TCE]_0 < 20$ ppm, or pentane (0.2 μL) if $[TCE]_0 > 20$ ppm. The overall solution was stirred for at least 3 hr to reach equilibrium. Then at time $t = 0$, a volume of Pd/Au NP (0.3 ML) suspension (0.4 mL) was injected into the bottle, which was kept at a stirring rate of 600 rpm. The reaction was monitored using the ECD for headspace samples containing methylene chloride, or FID for headspace samples containing pentane. TCE HDC reaction rates were determined by the initial slope of TCE concentration-time profiles within the first 5 min, and corrected for mass-transfer effects. For the testing of Pd/Au NPs (0.6 ML) and Pd NPs, volumes of 0.2 mL and 0.8 mL were used, respectively.

3.3. Results and discussion

3.3.1. Mass transfer analysis of NP catalysts

3.3.1.1. General theory for spherical non-porous catalytic particles

The NP-catalyzed TCE HDC can be considered to occur in a three-phase gas/liquid/solid reactor [76]. Scheme 3.1 shows the TCE transport from the headspace through liquid phase and to the catalyst particle surface.

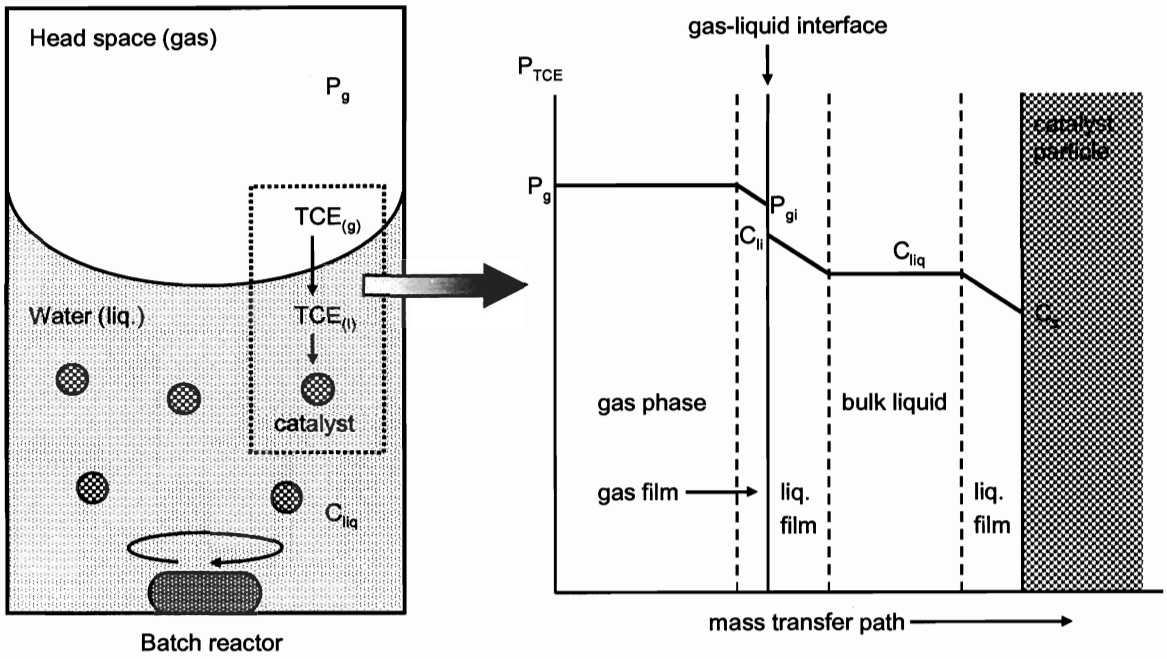

Scheme 3.1. Mass transfer pathway of TCE in the aqueous-phase TCE HDC reaction catalyzed by suspended particles in a batch reactor.

Because surface reaction cannot be faster than TCE mass transfer, the rate of surface reaction equals to the rate of mass transfer through each of the films (rate unit = [TCE amount/time]); therefore,

$$\frac{-\mathrm{d[TCE]}}{\mathrm{d}t} = r_{\mathrm{obs}} = r_{\mathrm{diff,\,g}} = r_{\mathrm{diff,\,gl}} = r_{\mathrm{diff,\,ls}} = r_{\mathrm{surf\ rxn}} \tag{1}$$

where

$$r_{\mathrm{diff,g}} = k_{\mathrm{g}} a_{\mathrm{gl}} (P_{\mathrm{g}} - P_{\mathrm{gi}}) / H_{\mathrm{TCE}} \tag{2}$$

$$r_{\mathrm{diff,gl}} = k_{\mathrm{gl}} a_{\mathrm{gl}} (C_{\mathrm{li}} - C_{\mathrm{liq}}) = k_{\mathrm{gl}} a_{\mathrm{gl}} (P_{\mathrm{li}} - P_{\mathrm{liq}}) / H_{\mathrm{TCE}} \tag{3}$$

$$r_{\mathrm{diff,ls}} = k_{\mathrm{ls}} a_{\mathrm{s}} (C_{\mathrm{liq}} - C_{\mathrm{s}}) = k_{\mathrm{ls}} a_{\mathrm{s}} (P_{\mathrm{liq}} - P_{\mathrm{s}}) / H_{\mathrm{TCE}} \tag{4}$$

With the assumption that the surface reaction can be described as a first-order reaction in TCE and zero-order in hydrogen (with hydrogen in excess), the rate equation (Eq. 1) becomes

$$r_{\text{surf rxn}} = ka_s C_s = ka_s P_s / H_{\text{TCE}} \tag{5}$$

In Eq. 5, C_s is TCE concentration at catalyst surface, and P_s is partial pressure of TCE at catalyst surface, calculated from Henry's law and C_s. Since $r_{\text{diff, ls}} = r_{\text{surf rxn}}$, then $k_{ls}a_s(P_{\text{liq}} - P_s) = ka_sP_s$ and P_s can be solved as

$$P_s = \frac{k_{ls}P_{\text{liq}}}{k + k_{ls}} \tag{6}$$

Substituting P_s from Eq. 6 to Eq. 4 gives

$$r_{\text{diff,ls}} = \frac{kk_{ls}a_sP_{\text{liq}}}{(k + k_{ls})H_{\text{TCE}}} \tag{7}$$

Similarly, P_{liq} and P_{li} can be solved from Eqs. 2-4 and be substituted into Eq. 2 to obtain

$$r_{\text{obs}} = \frac{P_g}{\left(\frac{1}{k_g a_{gl}} + \frac{1}{k_{gl}a_{gl}} + \frac{1}{k_{ls}a_s} + \frac{1}{ka_s}\right)H_{\text{TCE}}} \tag{8}$$

According to the literature [77], the gas film resistance of TCE is negligible compared to liquid film; therefore, Eq. 8 can be simplified to

$$r_{obs} = \frac{P_g}{\left(\frac{1}{k_{gl}a_{gl}} + \frac{1}{k_{ls}a_s} + \frac{1}{ka_s}\right)H_{TCE}} \tag{9}$$

From the definition of Henry's law constant $H = P_g / C_{liq}$, Eq. 9 can be rewritten as

$$r_{obs} = \frac{C_{liq}}{\frac{1}{k_{gl}a_{gl}} + \frac{1}{k_{ls}a_s} + \frac{1}{ka_s}} \tag{10}$$

Here, $1/k_{gl}a_{gl}$ and $1/k_{ls}a_s$ represent the resistances of diffusion through the liquid films at the gas-liquid interface and through the boundary layer at the liquid-particle surface, and $1/ka_s$ is the surface reaction resistance. By rearranging Eq. 10, one gets

$$\frac{C_{liq}}{r_{obs}} = \frac{1}{k_{gl}a_{gl}} + \frac{1}{k_{ls}a_s} + \frac{1}{ka_s} = \frac{C_1'}{a_{gl}} + \frac{C_2'}{a_s} \tag{11}$$

which simplifies to

$$\frac{1}{r_{obs}} = C_1 + \frac{C_2}{w_s} \tag{12}$$

where

$$w_s = a_s\left(\frac{d_p}{6}\right)\left(\frac{\rho_p}{\rho_{liq}}\right) \tag{13}$$

$$C_1 = \left(\frac{1}{k_{gl}a_{gl}}\right)\left(\frac{1}{C_{liq}}\right) \tag{14}$$

$$C_2 = \left(\frac{1}{k} + \frac{1}{k_{ls}}\right)\left(\frac{1}{C_{liq}}\right)\left(\frac{d_p}{6}\right)\left(\frac{\rho_p}{\rho_{liq}}\right) \tag{15}$$

Eq. 12 indicates that the observed reaction rate (r_{obs}) will vary with catalyst loading (w_s), which determines the liquid-catalyst surface area; it also indicates how mixing within the batch reactor affects the observed reaction rate. A stirring rate that is high enough for gas-liquid mass transfer to be negligible would give $C_1 \sim 0$, meaning $k_{gl}a_{gl}$ is very large. A low stirring rate would decrease the gas-liquid interfacial area a_{gl}, thereby giving a non-zero C_1 or intercept in a $1/r_{obs}$-vs.-$1/w_s$ plot. Thus, in this manner, the effect of stirring can be quantified. This mass transfer analysis is applicable to spherical non-porous catalytic particles of any size. This approach also applies to the general case of porous catalysts for three-phase gas/liquid/solid reactions if intraparticle porosity effects are included, e.g., in industrial hydrogenation reactions [76, 78-80].

3.3.1.2. Applicability of mass transfer model to Pd/Au and Pd NPs

So that the general analysis could be applied correctly to Pd/Au NPs (0.3 ML and 0.6 ML) and Pd NPs for TCE HDC, the condition of constant hydrogen concentration in the reactor needed to be satisfied. Calculations indicated that, within the 5-min time interval in which initial reaction rates were measured, the maximum consumed amounts of hydrogen were <1% of the initial amount (Table 3.1) while TCE conversions were <16%. Thus, the hydrogen content was in excess, and it could be approximated to be constant.

Table 3.1. Experimental conditions of mass transfer analysis with catalytic NPs.

Parameter	Pd/Au NPs (0.3 ML)	Pd/Au NPs (0.6 ML)	Pd NPs
Batch reactor total volume	250 mL	250 mL	250 mL
Liquid phase	173 mL	173 mL	173 mL
Gas phase	77 mL	77 mL	77 mL
Initial H_2 total amount	3.35×10^{-3} mol	3.35×10^{-3} mol	3.35×10^{-3} mol
Liquid phase	1.50×10^{-4} mol	1.50×10^{-4} mol	1.50×10^{-4} mol
Gas phase	3.20×10^{-3} mol	3.20×10^{-3} mol	3.20×10^{-3} mol
H_2 amount consumed in the first 5 min (as a percentage of initial H_2 amount charged to reactor)[a]	1.26×10^{-5} mol (0.375%)	2.10×10^{-5} mol (0.627%)	1.25×10^{-5} mol (0.373%)
Initial TCE total amount	3.34×10^{-5} mol	3.34×10^{-5} mol	3.34×10^{-6} mol
Liquid phase	2.87×10^{-5} mol	2.87×10^{-5} mol	2.87×10^{-6} mol
Gas phase	0.47×10^{-5} mol	0.47×10^{-5} mol	0.47×10^{-6} mol
Initial [TCE] in liquid phase ($[TCE]_0$)	21.8 ppm	21.8 ppm	2.18 ppm
Pd total amounts of 3 different initial catalyst charges	(1) 9.39×10^{-9} mol (2) 1.88×10^{-8} mol (3) 2.81×10^{-8} mol	(1) 9.39×10^{-9} mol (2) 1.88×10^{-8} mol (3) 2.81×10^{-8} mol	(1) 8.06×10^{-8} mol (2) 1.61×10^{-7} mol (3) 3.22×10^{-7} mol
Mass fraction of catalyst with respect to total liquid (w_s, g_{Pd}/g_{liquid})	(1) 5.77×10^{-9} (2) 1.15×10^{-8} (3) 1.73×10^{-8}	(1) 5.77×10^{-9} (2) 1.15×10^{-8} (3) 1.73×10^{-8}	(1) 4.95×10^{-8} (2) 9.90×10^{-8} (3) 1.98×10^{-7}
Au total amounts of 3 different initial catalyst charges	(1) 7.53×10^{-8} mol (2) 1.51×10^{-7} mol (3) 2.26×10^{-7} mol	(1) 7.53×10^{-8} mol (2) 1.51×10^{-7} mol (3) 2.26×10^{-7} mol	(1) n/a (2) n/a (3) n/a

[a] The initial reaction rates were measured in the first 5 min. Consumed H_2 amounts were based on the reaction stoichiometry: $Cl_2C{=}CHCl + 4\ H_2 \rightarrow H_3C{-}CH_3 + 3\ HCl$.

We recently found that the reaction order of TCE HDC was not necessarily always first-order in TCE, and that initial TCE concentration determined the observed reaction order depending on the Pd catalyst type [73]. Here, we were able to verify these observations by analyzing the reaction at "low" and "high" $[TCE]_0$ (Fig. 3.1). While the initial reaction rates were collected within the first 5 minutes of reaction, the concentration-time profiles of Fig. 3.1 were reasonably well-behaved for times beyond 5 min. As expected, the reaction was first-order in TCE concentration for Pd/Au NPs at both concentrations (Fig. 3.1a, b, d, e).

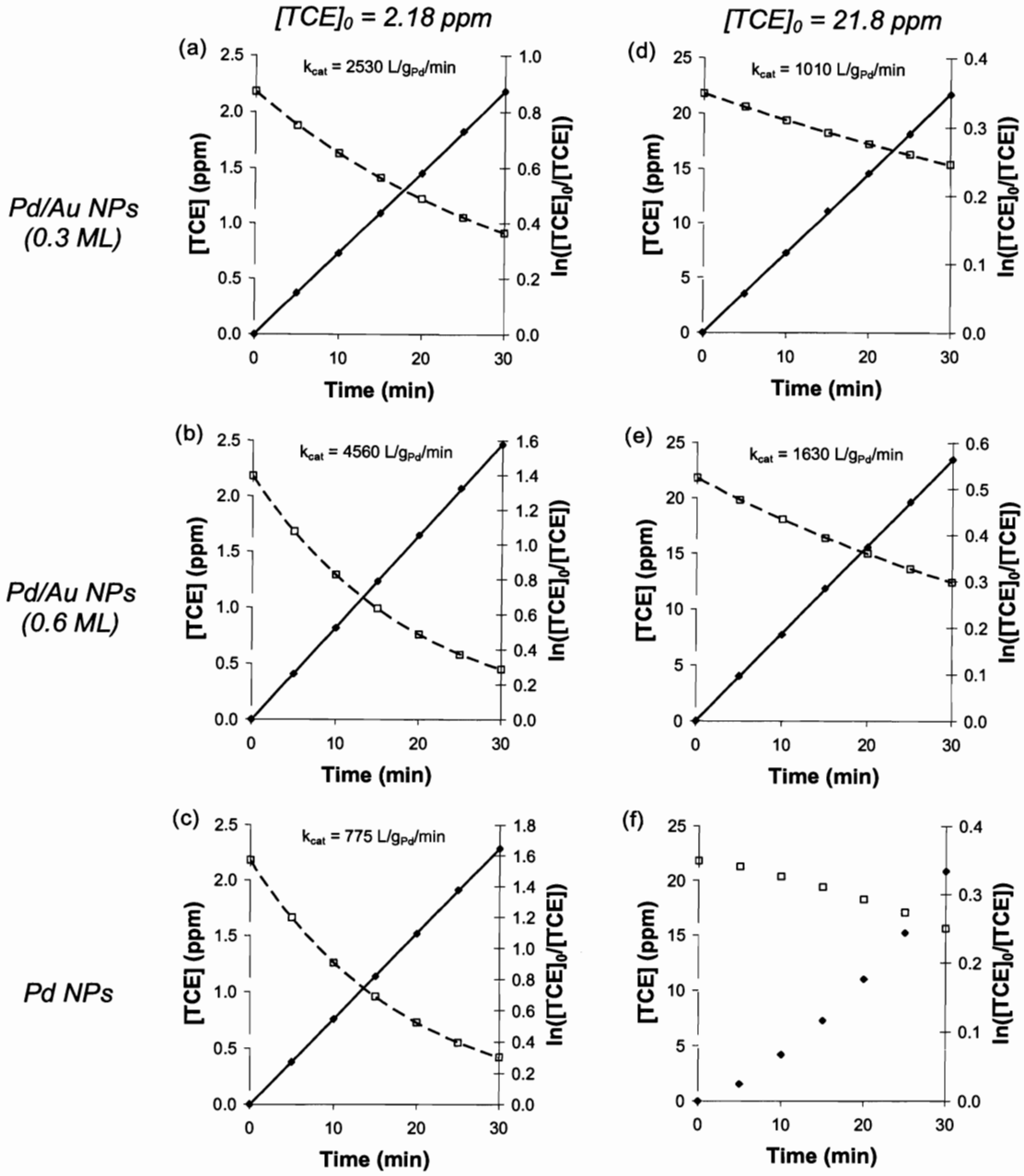

Figure 3.1. TCE concentration profiles in liquid phase (open square) with first-order fits (dashed line) and first-order linearizations (solid line) of TCE HDC batch reactions with different catalytic NPs and initial TCE concentrations. These reactions were carried out with a 600-rpm stirring rate.

In contrast, the reaction was first-order in TCE with Pd NPs at low $[TCE]_0$ (Fig. 3.1c) but was not first-order at high $[TCE]_0$ (Fig. 3.1f). The "low" $[TCE]_0$ of 2.18 ppm was close to the 1 ppm concentrations used by other research groups, in which first-order dependence was also reported [54, 81]. The first-order rate constants were calculated using Eq. 16.

$$k_{cat} = \frac{r_{obs,0}}{[Pd][TCE]_0} = \frac{\left(\frac{-d[TCE]}{dt}\right)_0}{[Pd][TCE]_0} \tag{16}$$

3.3.1.3. Determination of mass transfer resistances

The $1/r_{obs}$-vs.-$1/w_s$ plots were collected for the Pd/Au and Pd NPs (Fig. 3.2). Each data point corresponded to a separate catalyst run at a specific catalyst charge and stirring rate, with higher catalyst amounts and faster stirring rates leading to higher observed reaction rates.

The trendlines decreased with increasing stirring rates in all cases, and the intercept C_1 was nearly zero at 900 rpm, indicating the reaction system almost reached the condition of zero gas-liquid mass transfer resistance. It was estimated that increasing from 300 to 900 rpm reduced this mass transfer resistance by ~40 times (Table 3.2). Calculated from the intercept C_1, the $1/k_{gl}a_{gl}$ values at 300 and 600 rpm stirring rates were similar for each NP tested (within 15% difference), indicating that gas-liquid mass transfer resistance was independent of catalyst composition (Table 3.2). There was greater variation in $1/k_{gl}a_{gl}$ values at 900 rpm (~30% difference), which was attributed to their smaller values, the larger effects of measurement error, and operational instability of the magnetic stirrer at 900 rpm.

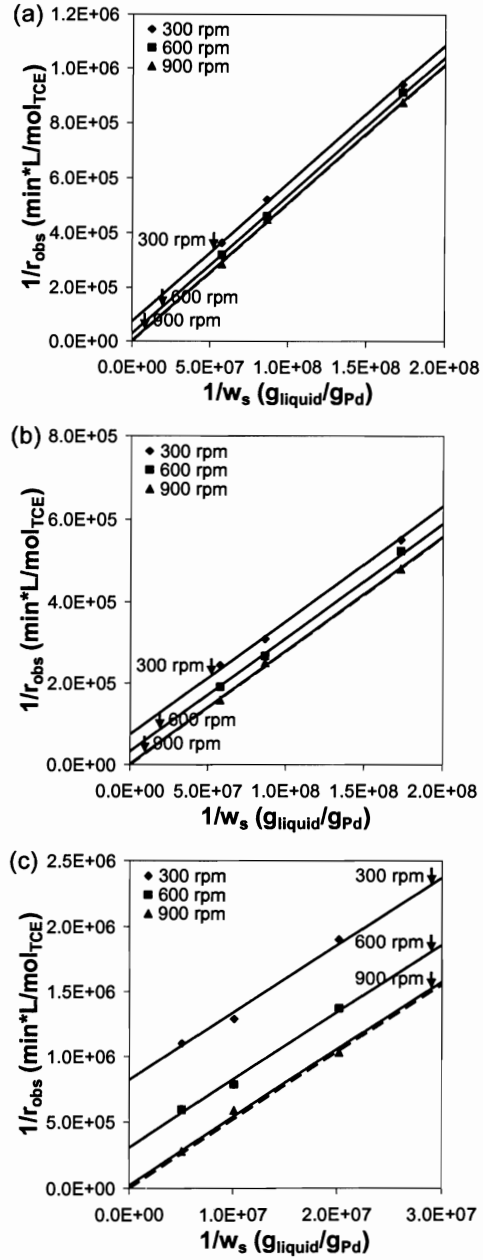

Figure 3.2. The relationship between $1/r_{obs}$ and $1/w_s$ for the mass transfer analysis of catalytic NPs (a) Pd/Au NPs (0.3 ML), (b) Pd/Au NPs (0.6 ML), and (c) Pd NPs. Dashed lines indicated zero gas-liquid mass transfer resistance.

Table 3.2. Mass transfer resistances and rate constants for TCE HDC reactions with NPs.

Term	Resistance type	Unit	Pd/Au NPs (0.3 ML)	Pd/Au NPs (0.6 ML)	Pd NPs
$1/k_{gl}a_{gl}$ (300 rpm)	Gas-liquid	min	12.2	12.3	13.6
$1/k_{gl}a_{gl}$ (600 rpm)	Gas-liquid	min	4.84	5.39	5.09
$1/k_{gl}a_{gl}$ (900 rpm)	Gas-liquid	min	0.300	0.252	0.377
$1/ka_s + 1/k_{ls}a_s$		min	43.6	26.1	8.66
$1/k_{ls}a_s$	Liquid-solid	min	0.00478	0.00519	0.00161
$1/ka_s$	Solid surface	min	43.6	26.1	8.66
k[a]		$L/m_{surf\ Pd}^2/min$	3.58	6.21	
k[b]		$L/m_{surf\ Pd}^2/min$			9.62
Initial TOF[a]		$mol_{TCE}/mol_{Pd}/s$	0.368	0.636	
		$mol_{TCE}/mol_{surf\ Pd}/s$	0.368	0.636	
Initial TOF[b]		$mol_{TCE}/mol_{Pd}/s$			0.0344
		$mol_{TCE}/mol_{surf\ Pd}/s$			0.0990
$k_{cat,\ corr}$[a]		$L/g_{Pd}/min$	1250	2160	
		$L/g_{surf\ Pd}/min$	1250	2160	
$k_{cat,\ corr}$[b]		$L/g_{Pd}/min$			1170
		$L/g_{surf\ Pd}/min$			3360
k_{cat} (600 rpm)[a]		$L/g_{Pd}/min$	1010	1630	
		$L/g_{surf\ Pd}/min$	1010	1630	
k_{cat} (600 rpm)[b]		$L/g_{Pd}/min$			775
		$L/g_{surf\ Pd}/min$			2230

[a] Initial liquid-phase $[TCE]_0 = 21.8$ ppm.
[b] Initial liquid-phase $[TCE]_0 = 2.18$ ppm.

The liquid-solid mass transfer coefficient k_{ls} towards a spherical particle could be estimated by the Ranz-Marshall correlation, $Sh = 2 + 0.6Re^{1/2}Sc^{1/3}$, for $2 \leq Re \leq 200$ and $0.6 \leq Sc \leq 2.7$ [82]. However, the maximum Reynolds number Re is 0.0094 and the Schmidt number Sc is 362 for our catalytic colloid system at room temperature. Convection contributes negligibly to diffusive mass transfer; therefore, the Sherwood number Sh = 2. From $Sh = k_{ls}d_p / D_{TCE}$, where D_{TCE} is the diffusivity of TCE in water (1.04×10^{-5} cm^2s^{-1} at 25 °C [83]), k_{ls} was calculated to be 0.520 m/s for 4-nm particles. Using the magic cluster model [50] and counting only the exposed surface Pd atoms, we calculated a_s as 23.9, 44.7, 121 $m^2/g_{catalyst}$ for Pd/Au (0.3 ML), Pd/Au (0.6 ML), and Pd

NPs, respectively, giving the corresponding liquid-solid mass transfer resistance $1/k_{ls}a_s$ values listed in Table 3.2.

With the slope C_2 nearly the same at different stirring rates for a given NP catalyst (Eq. 15), the surface reaction resistance $1/ka_s$ was found to be much greater than $1/k_{ls}a_s$, indicating the mass transfer effect through the diffusion boundary layer can be neglected (Table 3.2). The surface reaction rate constants k ($L/m_{surf\ Pd}^2/min$), which were based on the Pd metal surface area, indicated the catalysts could be ranked in decreasing activity in the following order: Pd NPs > Pd/Au NPs (0.6 ML) > Pd/Au NPs (0.3 ML). After converting into initial turnover frequencies (TOF's) by accounting for initial TCE concentrations, we confirmed that Pd/Au NPs (0.6 ML) > Pd/Au NPs (0.3 ML) on either a per-total-Pd-atom basis or a per-surface-Pd-atom basis (Table 3.2), which was consistent with our previous work [48, 50].

This analysis is based on the reasonable assumption that H_2 mass transfer is faster than TCE mass transfer. Analogous to the TCE case, H_2 mass transfer can be considered to occur through the gas film and liquid film at the gas-liquid interface, and the liquid film at the liquid-catalyst surface, terminating at the catalyst surface. At the gas-liquid interface, the gas film resistance is negligible compared to the liquid film resistance (10^3-10^4 difference [77, 84]). Considering the liquid film resistances at both interfaces, H_2 transfer is >4 times faster than TCE due to its higher molecular diffusivity in water (4.80×10^{-5} cm^2s^{-1} for H_2 and 1.04×10^{-5} cm^2s^{-1} for TCE at 25 °C [83, 85]). The H_2 consumed in the water phase would be replenished rapidly by the H_2 in the headspace, compared to TCE. This implies further that the water-phase hydrogen concentration can be approximated to be constant due to rapid hydrogen transport from the gas space.

To remove the effects of mass transfer (mostly due to transfer through gas-liquid interface) on observed reaction rates, we obtained reaction rate r_{corr} values by setting the mass-transfer resistances $1/k_{gl}a_{gl}$ and $1/k_{ls}a_s$ in Eq. 10 to zero, such that $r_{corr} = C_{liq} / (1/ka_s)$. The corrected rate constants were then calculated in the following way:

$$k_{cat,\,corr} = \frac{r_{corr}}{[Pd][TCE]_0} \tag{17}$$

It can be seen that mass transfer depressed observed rates significantly. For reactions carried out at a 600-rpm stirring rate, the measured rate constants k_{cat} for Pd/Au NPs (0.3 ML), Pd/Au NPs (0.6 ML), and Pd NPs were lower than the corrected values $k_{cat,\,corr}$ by 24%, 33%, and 51% (Table 3.2).

Other measured rates can be corrected for mass transfer effects without resorting to collecting additional $1/r_{obs}$-vs.-$1/w_s$ data, once $1/k_{gl}a_{gl}$ is known at a stirring rate and $1/k_{ls}a_s$ is neglected. It should be recognized that the gas-liquid mass transfer resistance $1/k_{gl}a_{gl}$ is not affected by catalyst composition or kinetics of the surface reaction.

TCE HDC performed with an initial liquid-phase $[TCE]_0$ = 2.18 ppm had observed rate constants k_{cat} of 2530, 4560, and 775 $L/g_{Pd}/min$ for Pd/Au NPs (0.3 ML), Pd/Au NPs (0.6 ML), and Pd NPs, at a 600-rpm stirring rate (Fig. 3.1). Calculations gave corrected rate constants $k_{cat,\,corr}$ of 2940, 6370, and 1170 $L/g_{Pd}/min$ for Pd/Au NPs (0.3 ML), Pd/Au NPs (0.6 ML), and Pd NPs, respectively (Table 3.3). The activity order was Pd/Au NPs (0.6 ML) > Pd/Au NPs (0.3 ML) > Pd NPs, consistent with previous results [50].

Table 3.3. Reaction rates for TCE HDC reactions with NPs at $[TCE]_0 = 2.18$ ppm.

Term	Unit	Pd/Au NPs (0.3 ML)	Pd/Au NPs (0.6 ML)	Pd NPs
r_{obs} (600 rpm)	$mol_{TCE}/L/min$	4.84×10^{-7}	8.75×10^{-7}	1.21×10^{-6}
k_{cat} (600 rpm)	$L/g_{Pd}/min$	2530	4560	775
	$L/g_{surf\ Pd}/min$	2530	4560	2230
r_{corr}	$mol_{TCE}/L/min$	5.64×10^{-7}	1.22×10^{-6}	1.92×10^{-6}
r_{corr}	ppm_{TCE}/min	0.0741	0.160	0.252
Initial TOF	$mol_{TCE}/mol_{Pd}/s$	0.0865	0.187	0.0344
	$mol_{TCE}/mol_{surf\ Pd}/s$	0.0865	0.187	0.0990
$k_{cat,\ corr}$	$L/g_{Pd}/min$	2940	6370	1170
	$L/g_{surf\ Pd}/min$	2940	6370	3360

3.3.2. Kinetic studies for reaction mechanism

3.3.2.1. General rate expression

To gain insight into the effects of TCE concentration on reaction order as illustrated in Fig. 3.1, we developed and tested a Langmuir-Hinshelwood model for TCE HDC after assuming the reaction proceeded through the same sequential dechlorination pathway on all catalyst compositions [48] and correcting the measured reaction rates for mass transfer effects. We also assumed that the citrate salt species were bound loosely to the NP surface through electrostatics, such that the citrate provided access to the NP surface and colloidal stability to the NP suspensions [86, 87], and that citrate did not compete for adsorption sites with TCE and H_2. Citrate and other ionic ligands are unlike other NP stabilizers, like polymers [88, 89] and dendrimers [90, 91], that are bound strongly to the NP surface to block active sites [86].

The reaction rate equation of TCE HDC was derived as follows. Pd activity of HDC reactions for different chlorinated compounds is VC > DCEs > TCE > PCE (perchloroethene or tetrachloroethene) [59]. That is, to break the first C-Cl bond is the slowest step for the whole TCE HDC process [48, 63], which was shown in Scheme 3.2.

Scheme 3.2. Proposed reaction mechanism for aqueous-phase catalytic TCE HDC[a].

Adsorption:

$$H_2 + 2S \xleftrightarrow{K_{H_2}} 2H \cdot S \quad (18)$$

$$TCE + S \xleftrightarrow{K_{TCE}} TCE \cdot S \quad (19)$$

Surface reaction:

$$TCE \cdot S + H \cdot S \xrightarrow{k} DCE \cdot S + Cl \cdot S \quad (20)$$

$$DCE \cdot S + H \cdot S \rightarrow VC \cdot S + Cl \cdot S \quad (21)$$

$$VC \cdot S + H \cdot S \rightarrow Ethene \cdot S + Cl \cdot S \quad (22)$$

$$Ethene \cdot S + H \cdot S \rightarrow (C_2H_5) \cdot S + S \quad (23)$$

$$(C_2H_5) \cdot S + H \cdot S \rightarrow Ethane \cdot S + S \quad (24)$$

Desorption:

$$Ethane \cdot S \rightarrow Ethane + S \quad (25)$$

Overall reaction:

$$TCE + 4H_2 \rightarrow Ethane + 3HCl \quad (26)$$

[a] S = catalytic active sites, DCE = dichloroethenes, VC = vinyl chloride.

Therefore, it is reasonable to assume that the surface reaction Eq. 20 (TCE to DCEs) is the rate-limiting step. All the other surface reactions are so fast that the concentrations of the intermediates can be ignored. From the rate-limiting step (Eq. 20),

$$r_{corr} = k[H \cdot S][TCE \cdot S] \quad (27)$$

r_{corr} is applied in Eq. 27 in order to recognize that the rate here is the surface reaction rate without any mass transfer resistances. From the adsorption steps (Eqs. 18 and 19),

$$[H \cdot S] = K_{H_2}^{1/2}[H_2]^{1/2}[S] \quad (28)$$

$$[TCE \cdot S] = K_{TCE}[TCE][S] \quad (29)$$

From active site balance,

$$[S]_{total} = [S] + [H \cdot S] + [TCE \cdot S] + [Cl \cdot S] + [DCE \cdot S] + [VC \cdot S] + [Ethene \cdot S] + [(C_2H_5) \cdot S] + [Ethane \cdot S] \quad (30)$$

[DCE·S], [VC·S], [Ethene·S], and $[(C_2H_5)\cdot S]$ are all very small due to the rapid surface reactions. [Cl·S] and [Ethane·S] are also very small at the initial stage of the TCE HDC reaction. Therefore,

$$[S]_{total} = [S] + [H \cdot S] + [TCE \cdot S] \quad (31)$$

$$[S] = [S]_{total} - [H \cdot S] - [TCE \cdot S] \quad (32)$$

Apply Eqs. 28, 29, and 32 into Eq. 27 and then the general rate equation can be obtained:

$$\frac{-\mathrm{d}[TCE]}{\mathrm{d}t} = r_{corr} = \frac{kK_{H_2}^{1/2} K_{TCE} [S]_{total}^2 [H_2]^{1/2} [TCE]}{\left(1 + K_{H_2}^{1/2} [H_2]^{1/2} + K_{TCE}[TCE]\right)^2} \quad (33)$$

If the water-phase hydrogen concentration is in excess and approximately constant due to rapid hydrogen transport from the gas space, this simplifies to

$$\frac{-\mathrm{d}[TCE]}{\mathrm{d}t} = \frac{\alpha [TCE]}{\left(1 + \beta [TCE]\right)^2} \quad (34)$$

where

$$\alpha = \frac{kK_{H_2}^{1/2} K_{TCE} [S]_{total}^2 [H_2]^{1/2}}{\left(1 + K_{H_2}^{1/2} [H_2]^{1/2}\right)^2} \quad (35)$$

$$\beta = \frac{K_{TCE}}{1 + K_{H_2}^{1/2} [H_2]^{1/2}} \quad (36)$$

If TCE concentration is very low, Eq. 34 can be further simplified to

$$\frac{-\mathrm{d}[\mathrm{TCE}]}{\mathrm{d}t} = \alpha[\mathrm{TCE}] \tag{37}$$

which is consistent with the pseudo-first-order TCE HDC kinetics that are usually (but not always) observed.

3.3.2.2. Fitting of experimental data

Batch experiments at different initial TCE concentrations with catalytic NPs were carried out, according to conditions listed in Table 3.4. The maximum consumed amounts of hydrogen were <1.1% of the total amount charged to the reactor. The reaction rates (measured at 600 rpm, corrected for mass transfer effects, and normalized by surface Pd atoms) increased with [TCE] for Pd/Au NPs (Fig. 3.3a). However, the reaction rate profile for Pd NPs reached a maximum before decreasing at higher [TCE], an observation not reported before. The activity trend of Pd/Au NPs (0.6 ML) > Pd/Au NPs (0.3 ML) > Pd NPs was clear at all TCE concentrations. This trend was consistent with our previous work, which was performed at 60-70 ppm TCE [48, 50].

Table 3.4. Experimental conditions of kinetic studies with catalytic NPs.

Parameter	Pd/Au NPs (0.3 ML)	Pd/Au NPs (0.6 ML)	Pd NPs
Batch reactor total volume	250 mL	250 mL	250 mL
Liquid phase	173 mL	173 mL	173 mL
Gas phase	77 mL	77 mL	77 mL
Initial H_2 total amount	3.35×10^{-3} mol	3.35×10^{-3} mol	3.35×10^{-3} mol
Liquid phase	1.50×10^{-4} mol	1.50×10^{-4} mol	1.50×10^{-4} mol
Gas phase	3.20×10^{-3} mol	3.20×10^{-3} mol	3.20×10^{-3} mol
Max consumed H_2 amount (as a percentage of initial H_2 amount charged to reactor)	2.14×10^{-5} mol (0.64%)	3.64×10^{-5} mol (1.09%)	3.42×10^{-5} mol (1.02%)
Initial TCE total amount (86% in liquid, 14% in gas)	10^{-8}-10^{-4} mol	10^{-8}-10^{-4} mol	10^{-8}-10^{-4} mol
Initial [TCE] in liquid phase ($[TCE]_0$)	10^{-2}-10^{2} ppm	10^{-2}-10^{2} ppm	10^{-2}-10^{2} ppm
Pd total amount	1.25×10^{-8} mol	1.25×10^{-8} mol	2.30×10^{-7} mol
Surface Pd amount[a]	1.25×10^{-8} mol	1.25×10^{-8} mol	8.00×10^{-8} mol
Surface Pd concentration in liquid phase	7.23×10^{-8} mol/L	7.23×10^{-8} mol/L	4.62×10^{-7} mol/L
Au total amount	1.01×10^{-7} mol	5.03×10^{-8} mol	n/a

[a] Surface Pd amounts were calculated from the magic cluster model with 4-nm particles.

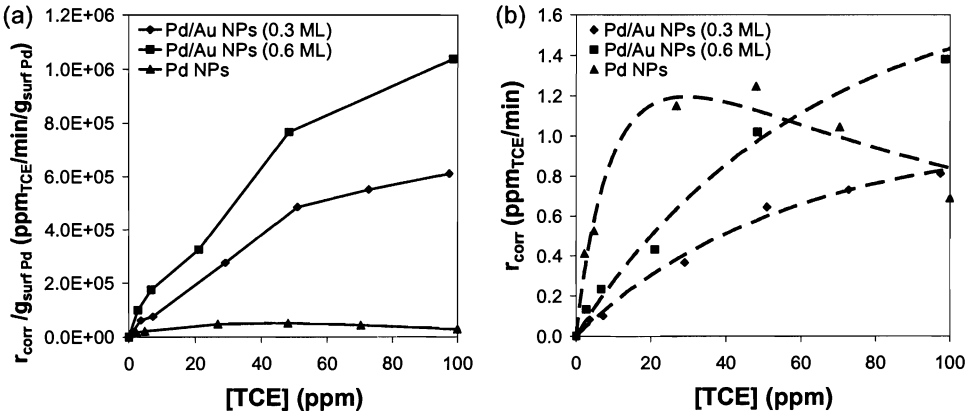

Figure 3.3. TCE HDC reaction rate profiles for Pd/Au NPs (0.3 ML), Pd/Au NPs (0.6 ML), and Pd NPs at different TCE concentrations: (a) normalized to surface Pd content, and (b) not normalized to surface Pd content, shown with fitted curves for reaction model (dashed line). The reaction rates were measured at 600 rpm, and corrected for mass transfer effects.

We performed non-linear regression of the reaction rate data to the simplified rate expression (Eq. 34), and found that the Langmuir-Hinshelwood reaction model fit

reasonably well (parameters shown in Table 3.5). Fig. 3.3b shows the fitted curves with the corrected reaction rates. Both Pd/Au NP compositions exhibited more similar to first-order behavior, as reflected by the much smaller β values compared to the β value for Pd NPs (Table 3.5). This suggested that TCE had a lower adsorption affinity for the Pd/Au NP surface, and/or that H_2 had a higher adsorption affinity, according to Eq. 34. The latter point is consistent with reports that hydrogen binding to Pd atoms supported on a Au substrate is stronger than that for a pure Pd substrate [92-94]. This enhancement in H_2 adsorption caused by Au may be correlated to its electronic effect on Pd [95-101]. In contrast, Pd NPs exhibited a maximum in TCE HDC activity, indicating a higher TCE adsorption affinity that contributes to competitive adsorption with itself, and/or a lower H_2 adsorption affinity compared to the Pd/Au NPs.

Table 3.5. Fitted parameters of the proposed Langmuir-Hinshelwood mechanism.

Fitted parameter	Pd/Au NPs (0.3 ML)	Pd/Au NPs (0.6 ML)	Pd NPs
α	0.0180	0.0295	0.163
β	0.00470	0.00436	0.0340
α'	3.44×10^{12}	5.64×10^{12}	7.64×10^{11}
γ	7.33×10^{14}	1.29×10^{15}	2.25×10^{13}

We gained information about relative H_2 adsorption affinities by examining the fitted parameters in the following way. We defined two parameters, α' and γ.

$$\alpha' = \frac{\alpha}{[S]_{total}^2} = \frac{kK_{H_2}^{1/2}K_{TCE}[H_2]^{1/2}}{\left(1+K_{H_2}^{1/2}[H_2]^{1/2}\right)^2} \tag{38}$$

$$\gamma = \frac{\alpha'}{\beta} = \frac{kK_{H_2}^{1/2}[H_2]^{1/2}}{1+K_{H_2}^{1/2}[H_2]^{1/2}} \tag{39}$$

α' is α normalized by square of the active site concentration, therefore becoming independent of the catalyst amount. We assumed that the number of active sites equaled the number of surface Pd atoms (Table 3.4). γ is the ratio of α' and β, and is proportional to k, the surface reaction rate constant of the rate-limiting step (the substitution of a Cl atom in TCE with a H atom). We then compared the γ and k values of the three catalysts by calculating their ratios for different pairs of catalysts (Table 3.6).

Table 3.6. Comparison among ratios of parameters in the TCE HDC reaction mechanism.

Ratio	Pd/Au NPs (0.3 ML) / Pd/Au NPs (0.6 ML)	Pd/Au NPs (0.3 ML) / Pd NPs	Pd/Au NPs (0.6 ML) / Pd NPs
$\gamma_{catalyst1}/\gamma_{catalyst2}$	0.57	33	58
$k_{catalyst1}/k_{catalyst2}$[a]	0.46	0.88	1.9

[a] $k_{catalyst1}/k_{catalyst2} = k_{cat,\ corr1}/k_{cat,\ corr2}$ from data in Table 3.3. Initial liquid-phase $[TCE]_0 = 2.18$ ppm.

By relating these ratio values to one another using Eq. 40,

$$\frac{\gamma_{catalyst1}}{\gamma_{catalyst2}} = \frac{k_{catalyst1}}{k_{catalyst2}} \times \frac{\dfrac{K_{H_2,\,catalyst1}^{1/2}[H_2]^{1/2}}{1+K_{H_2,\,catalyst1}^{1/2}[H_2]^{1/2}}}{\dfrac{K_{H_2,\,catalyst2}^{1/2}[H_2]^{1/2}}{1+K_{H_2,\,catalyst2}^{1/2}[H_2]^{1/2}}} \tag{40}$$

we determined that the H_2 adsorption equilibrium constants for each catalyst were related as $K_{H2,\ Pd/Au\ NPs\ (0.3\ ML)}$:$K_{H2,\ Pd/Au\ NPs\ (0.6\ ML)}$:$K_{H2,\ Pd\ NPs}$ = 71:49:1. The relative magnitudes indicated that H_2 had a higher adsorption affinity for Pd/Au NPs than for Pd NPs, and a higher adsorption affinity for 0.3-ML Pd/Au NPs than for 0.6-ML Pd/Au NPs.

3.4. Conclusions

A comprehensive analysis of aqueous-phase TCE HDC catalyzed by colloidal Pd-based NPs was carried out. The gas-liquid mass transfer coefficient, the liquid-solid mass transfer coefficient, and the surface reaction for each NP catalyst were experimentally quantified, with the gas-liquid transfer rate found to be a significant contributor to the observed reaction rate. At an initial liquid-phase TCE concentration of 2.18 ppm and a 600-rpm stirring rate, observed pseudo-first-order rate constants of Pd/Au NPs (0.6 ML), Pd/Au NPs (0.3 ML), and Pd NPs were 4560, 2530, and 775 $L/g_{Pd}/min$, and after correction for mass transfer, they were 6370, 2940, and 1170 $L/g_{Pd}/min$. At a higher initial liquid-phase TCE concentration of 21.8 ppm, the rate constants were lower and the Pd NPs lost their first-order dependence on TCE concentration. A Langmuir-Hinshelwood model with cleavage of the first C-Cl bond of TCE as the rate-limiting step was developed, which matched the mass-transfer-corrected kinetics of each of the three Pd-based NP catalysts. Analysis of the fitted parameters provided information for the first time about the adsorption affinities of the reactants for the various catalyst surfaces. Compared to Pd NPs, Pd/Au NPs had smaller equilibrium adsorption constants for TCE, which resulted in their first-order TCE concentration dependence. Pd NPs had a higher TCE equilibrium adsorption constant, which resulted in non-first-order dependence on TCE concentration at high TCE concentrations. Pd/Au NPs had higher H_2 equilibrium adsorption constants than Pd NPs. When developed and applied properly, this rigorous approach to kinetics analysis can be useful for a variety of liquid-phase reactions and catalytically active colloidal suspensions.

3.5. Symbols and notations

a_{gl}, a_s	Specific areas for gas-liquid interface and catalyst solid in overall batch reactor liquid volume
C_{li}, C_{liq}, C_s	Concentrations of TCE in liquid phase at gas-liquid interface, in liquid bulk, and at catalyst surface
d_p	Mean diameter of catalyst particle
D_{TCE}	Diffusivity of TCE in water
H	Henry's law constant
k	Rate constant for surface reaction
k_{cat}	Apparent rate constant obtained from uncorrected reaction rates
$k_{cat,\ corr}$	Rate constant after correction of mass transfer
k_g, k_{gl}, k_{ls}	Mass transfer coefficients for gas, gas-liquid, and liquid-solid
K	Equilibrium constant
P_g, P_{gi}	Partial pressures of TCE in gas bulk and gas film at gas-liquid interface
P_{li}, P_{liq}, P_s	Partial pressures of TCE in liquid film at gas-liquid interface, in liquid bulk, and at catalyst surface
ρ_p	Density of catalyst particle
ρ_{liq}	Density of liquid
r_{obs}	Observed reaction rate
r_{corr}	Corrected reaction rate (without mass transfer limitations)
$r_{diff,\ g}$, $r_{diff,\ gl}$, $r_{diff,\ ls}$	Rates of mass transfer through gas film, liquid film at gas-liquid interface, and liquid-solid interface
$r_{surf\ rxn}$	Rate of surface reaction
S	Active site on catalyst surface
w_s	Mass fraction of catalyst with respect to total liquid

Subscript:

0	Initial condition

3.6. References

[1] L.N. Lewis, Chem. Rev. 93 (1993) 2693-2730.

[2] D. Astruc, F. Lu, J.R. Aranzaes, Angew. Chem.-Int. Edit. 44 (2005) 7852-7872.

[3] D. Astruc (Ed.), Nanoparticles and Catalysis. Wiley, Weinheim, Germany, 2008.

[4] X. Chen, S.S. Mao, Chem. Rev. 107 (2007) 2891-2959.

[5] J. Yu, V.S. Murthy, R.K. Rana, M.S. Wong, Chem. Commun. (2006) 1097-1099.

[6] G. Schmid, Chem. Rev. 92 (1992) 1709-1727.

[7] A.L. Efros, M. Rosen, Annu. Rev. Mater. Sci. 30 (2000) 475-521.

[8] S. Asokan, K.M. Krueger, V.L. Colvin, M.S. Wong, Small 3 (2007) 1164-1169.

[9] D.V. Talapin, I. Mekis, S. Gotzinger, A. Kornowski, O. Benson, H. Weller, J. Phys. Chem. B 108 (2004) 18826-18831.

[10] A. Roucoux, J. Schulz, H. Patin, Chem. Rev. 102 (2002) 3757-3778.

[11] H. Bonnemann, R.M. Richards, Eur. J. Inorg. Chem. (2001) 2455-2480.

[12] M. Haruta, J. New Mat.Electrochem. Syst. 7 (2004) 163-172.

[13] A.S.K. Hashmi, G.J. Hutchings, Angew. Chem.-Int. Edit. 45 (2006) 7896-7936.

[14] N. Weiher, E. Bus, L. Delannoy, C. Louis, D.E. Ramaker, J.T. Miller, J.A. van Bokhoven, J. Catal. 240 (2006) 100-107.

[15] J. Grunes, J. Zhu, E.A. Anderson, G.A. Somorjai, J. Phys. Chem. B 106 (2002) 11463-11468.

[16] C. Bianchini, V. Dal Santo, A. Meli, S. Moneti, M. Moreno, W. Oberhauser, R. Psaro, L. Sordelli, F. Vizza, J. Catal. 213 (2003) 47-62.

[17] A.G. Boudjahem, S. Monteverdi, M. Mercy, M.M. Bettahar, J. Catal. 221 (2004) 325-334.

[18] N.R. Jana, Z.L. Wang, T. Pal, Langmuir 16 (2000) 2457-2463.

[19] T.K. Sau, A. Pal, T. Pal, J. Phys. Chem. B 105 (2001) 9266-9272.

[20] S.K. Ghosh, M. Mandal, S. Kundu, S. Nath, T. Pal, Appl. Catal. A-Gen. 268 (2004) 61-66.

[21] M. Comotti, C. Della Pina, R. Matarrese, M. Rossi, Angew. Chem.-Int. Edit. 43 (2004) 5812-5815.

[22] P. Beltrame, M. Comotti, C. Della Pina, M. Rossi, Appl. Catal. A-Gen. 297 (2006) 1-7.

[23] H. Tsunoyama, H. Sakurai, T. Tsukuda, Chem. Phys. Lett. 429 (2006) 528-532.

[24] N.N. Hoover, B.J. Auten, B.D. Chandler, J. Phys. Chem. B 110 (2006) 8606-8612.

[25] C.J. Crump, J.D. Gilbertson, B.D. Chandler, Top. Catal. 49 (2008) 233-240.

[26] L.M. Bronstein, D.M. Chernyshov, I.O. Volkov, M.G. Ezernitskaya, P.M. Valetsky, V.G. Matveeva, E.M. Sulman, J. Catal. 196 (2000) 302-314.

[27] S. Ozkar, R.G. Finke, J. Am. Chem. Soc. 124 (2002) 5796-5810.

[28] H. Bonnemann, G.A. Braun, Angew. Chem.-Int. Edit. Engl. 35 (1996) 1992-1995.

[29] H. Hirai, N. Yakura, Y. Seta, S. Hodoshima, React. Funct. Polym. 37 (1998) 121-131.

[30] P. Dash, N.A. Dehm, R.W.J. Scott, J. Mol. Catal. A-Chem. 286 (2008) 114-119.

[31] R. Narayanan, M.A. El-Sayed, J. Phys. Chem. B 107 (2003) 12416-12424.

[32] P.L. Freund, M. Spiro, J. Phys. Chem. 89 (1985) 1074-1077.

[33] R.K. Sharma, P. Sharma, A. Maitra, J. Colloid Interface Sci. 265 (2003) 134-140.

[34] I.P. Beletskaya, A.V. Cheprakov, Chem. Rev. 100 (2000) 3009-3066.

[35] F. Bellina, A. Carpita, R. Rossi, Synthesis (2004) 2419-2440.

[36] N.T.S. Phan, M. Van Der Sluys, C.W. Jones, Adv. Synth. Catal. 348 (2006) 609-679.

[37] J.G. de Vries, Dalton Trans. (2006) 421-429.

[38] D. Astruc, Inorg. Chem. 46 (2007) 1884-1894.

[39] R. Narayanan, M.A. El-Sayed, Top. Catal. 47 (2008) 15-21.

[40] J.D. Aiken, R.G. Finke, J. Mol. Catal. A-Chem. 145 (1999) 1-44.

[41] J.A. Widegren, R.G. Finke, J. Mol. Catal. A-Chem. 198 (2003) 317-341.

[42] R. Narayanan, M.A. El-Sayed, Nano Lett. 4 (2004) 1343-1348.

[43] S.K. Ghosh, S. Kundu, M. Mandal, T. Pal, Langmuir 18 (2002) 8756-8760.

[44] S. Panigrahi, S. Basu, S. Praharaj, S. Pande, S. Jana, A. Pal, S.K. Ghosh, T. Pal, J. Phys. Chem. C 111 (2007) 4596-4605.

[45] H.A. Wierenga, L. Soethout, J.W. Gerritsen, B.E.C. Vandeleemput, H. Vankempen, G. Schmid, Adv. Mater. 2 (1990) 482-484.

[46] H. Bonnemann, G.A. Braun, Chem.-Eur. J. 3 (1997) 1200-1202.

[47] S. Ozkar, R.G. Finke, J. Am. Chem. Soc. 127 (2005) 4800-4808.

[48] M.S. Wong, P.J.J. Alvarez, Y.-L. Fang, N. Akçin, M.O. Nutt, J.T. Miller, K.N. Heck, J. Chem. Technol. Biotechnol. 84 (2009) 158-166.

[49] M.O. Nutt, J.B. Hughes, M.S. Wong, Environ. Sci. Technol. 39 (2005) 1346-1353.

[50] M.O. Nutt, K.N. Heck, P. Alvarez, M.S. Wong, Appl. Catal. B-Environ. 69 (2006) 115-125.

[51] F.J. Urbano, J.M. Marinas, J. Mol. Catal. A-Chem. 173 (2001) 329-345.

[52] F. Alonso, I.P. Beletskaya, M. Yus, Chem. Rev. 102 (2002) 4009-4091.

[53] V.I. Kovalchuk, J.L. d'Itri, Appl. Catal. A-Gen. 271 (2004) 13-25.

[54] G.V. Lowry, M. Reinhard, Environ. Sci. Technol. 33 (1999) 1905-1910.

[55] G.V. Lowry, M. Reinhard, Environ. Sci. Technol. 34 (2000) 3217-3223.

[56] G.V. Lowry, M. Reinhard, Environ. Sci. Technol. 35 (2001) 696-702.

[57] N. Munakata, M. Reinhard, Appl. Catal. B-Environ. 75 (2007) 1-10.

[58] C. Schuth, N.A. Kummer, C. Weidenthaler, H. Schad, Appl. Catal. B-Environ. 52 (2004) 197-203.

[59] K. Mackenzie, H. Frenzel, F.D. Kopinke, Appl. Catal. B-Environ. 63 (2006) 161-167.

[60] J.C. Liu, F. He, E. Durham, D.Y. Zhao, C.B. Roberts, Langmuir 24 (2008) 328-336.

[61] C.D. Thompson, R.M. Rioux, N. Chen, F.H. Ribeiro, J. Phys. Chem. B 104 (2000) 3067-3077.

[62] N. Chen, R.M. Rioux, F.H. Ribeiro, J. Catal. 211 (2002) 192-197.

[63] N. Chen, R.M. Rioux, L.A.M.M. Barbosa, F.H. Ribeiro, Langmuir 26 (2010) 16615-16624.

[64] M.J. Moran, J.S. Zogorski, P.J. Squillace, Environ. Sci. Technol. 41 (2007) 74-81.

[65] H.H. Russell, J.E. Matthews, G.W. Sewell, Ground Water Issue, EPA/540/S-92/002. U. S. Environmental Protection Agency, Washington, DC, 1992.

[66] 2001 Toxics Release Inventory Public Data Release Report, 260-R-03-001. Office of Environmental Information, U. S. Environmental Protection Agency, Washington, DC, 2003.

[67] CERCLA Priority List of Hazardous Substances. Agency for Toxic Substances and Disease Registry, U. S. Department of Health and Human Services, Atlanta, GA, 2007.

[68] Toxicological Profile for Trichloroethylene. Agency for Toxic Substances and Disease Registry, U. S. Department of Health and Human Services, Atlanta, GA, 1997.

[69] 2006 Edition of the Drinking Water Standards and Health Advisories, 822-R-06-013. Office of Water, U. S. Environmental Protection Agency, Washington, DC, 2006.

[70] V. Ponec, G.C. Bond, Catalysis by Metals and Alloys. Elsevier, Amsterdam, The Netherlands, 1995.

[71] F. Maroun, F. Ozanam, O.M. Magnussen, R.J. Behm, Science 293 (2001) 1811-1814.

[72] R.J. Behm, Z. Phys. Chemie-Int. J. Res. Phys. Chem. Chem. Phys. 223 (2009) 9-36.

[73] K.N. Heck, M.O. Nutt, P.J.J. Alvarez, M.S. Wong, J. Catal. 267 (2009) 97-104.

[74] Y.-L. Fang, J.T. Miller, N. Guo, K.N. Heck, P.J.J. Alvarez, M.S. Wong, Catal. Today 160 (2011) 96-102.

[75] Y.-L. Fang, K.N. Heck, P.J.J. Alvarez, M.S. Wong, ACS Catalysis 1 (2011) 128-138.

[76] C.H. Bartholomew, R.J. Farrauto, Fundamentals of Industrial Catalytic Processes. Wiley, Hoboken, NJ, 2006, pp. 496-500.

[77] W. Brutsaert, G.H. Jirka, Gas Transfer at Water Surfaces. Springer, New York, NY, 1984, pp. 30.

[78] L. Cerveny (Ed.), Catalytic Hydrogenation. Elsevier, Amsterdam, The Netherlands, 1988.

[79] O. Levenspiel, The Chemical Reactor Omnibook. OSU Book Stores, Inc., Corvallis, OR, 1979.

[80] O. Levenspiel, Chemical Reaction Engineering. Wiley, New York, NY, 1999.

[81] F.D. Kopinke, K. Mackenzie, R. Kohler, Appl. Catal. B-Environ. 44 (2003) 15-24.

[82] İ. Tosun, Modelling in Transport Phenomena: A Conceptual Approach. Elsevier, Oxford, UK, 2002, pp. 84-86.

[83] R.P. Schwarzenbach, P.M. Gschwend, D.M. Imboden, Environmental Organic Chemistry. Wiley, Hoboken, NJ, 1993.

[84] M.A. Donelan, W.M. Drennan, E.S. Saltzman, R. Wanninkhof (Ed.), Gas Transfer at Water Surfaces. American Geophysical Union, Washington, DC, 2002.

[85] A.F. Mazarei, O.C. Sandall, Aiche J. 26 (1980) 154-157.

[86] M.C. Daniel, D. Astruc, Chem. Rev. 104 (2004) 293-346.

[87] J. Turkevich, P.C. Stevenson, J. Hillier, Discussions of the Faraday Society (1951) 55-&.

[88] H. Otsuka, Y. Nagasaki, K. Kataoka, Adv. Drug Deliv. Rev. 55 (2003) 403-419.

[89] H. Tsunoyama, H. Sakurai, Y. Negishi, T. Tsukuda, J. Am. Chem. Soc. 127 (2005) 9374-9375.

[90] V. Chechik, R.M. Crooks, Langmuir 15 (1999) 6364-6369.

[91] M.G. Weir, M.R. Knecht, A.I. Frenkel, R.M. Crooks, Langmuir 26 (2010) 1137-1146.

[92] M. Baldauf, D.M. Kolb, Electrochim. Acta 38 (1993) 2145-2153.

[93] S. Pandelov, U. Stimming, Electrochim. Acta 52 (2007) 5548-5555.

[94] L.A. Kibler, Electrochim. Acta 53 (2008) 6824-6828.

[95] P.A.P. Nascente, S.G.C. Decastro, R. Landers, G.G. Kleiman, Phys. Rev. B 43 (1991) 4659-4666.

[96] B.E. Koel, A. Sellidj, M.T. Paffett, Phys. Rev. B 46 (1992) 7846-7856.

[97] B. Hammer, Y. Morikawa, J.K. Norskov, Phys. Rev. Lett. 76 (1996) 2141-2144.

[98] A. Ruban, B. Hammer, P. Stoltze, H.L. Skriver, J.K. Norskov, J. Mol. Catal. A-Chem. 115 (1997) 421-429.

[99] A. Roudgar, A. Gross, Phys. Rev. B 67 (2003).

[100] D.I. Enache, J.K. Edwards, P. Landon, B. Solsona-Espriu, A.F. Carley, A.A. Herzing, M. Watanabe, C.J. Kiely, D.W. Knight, G.J. Hutchings, Science 311 (2006) 362-365.

[101] J.G. Chen, C.A. Menning, M.B. Zellner, Surf. Sci. Rep. 63 (2008) 201-254.

Chapter 4

Structural and Catalytic Properties of Thermal Annealed Palladium-decorated Gold Nanoparticles

4.1. Introduction

One way to test the hypothesis that palladium (Pd) ensembles on the gold nanoparticle (Au NP) surface or PdAu mixed sites are responsible for the enhanced catalysis observed for trichloroethene hydrodechlorination (TCE HDC) is to modify the Pd-on-Au nanostructure carefully and to assess the modification on catalysis. In this work, we performed a systematic study to exhibit structure evolution of palladium-decorated gold nanoparticles (Pd/Au NPs) with heat treatments, comparing with catalytic testing of TCE HDC, in order to understand how the nanostructure affects catalytic performance. Nanostructure was controlled by heat treatments and characterized with X-ray absorption spectroscopy (XAS). Pd islands (atomic ensembles) on the Au NP surface were shown as the major active sites, and such special structure would be "erased" by heat, leading to lower catalytic activity. Results supported that the geometric effect was dominant in the system. This work demonstrated the structure-property relationship of Pd/Au NPs, and could also be adapted to other bimetallic systems.

4.2. Experimental

4.2.1. Preparation of NP catalysts

4.2.1.1. Synthesis of colloidal NP catalysts

Pd/Au NPs in the colloidal form were prepared as in our previous works [1-3]; Au NPs were synthesized first, followed by Pd coating. For Au NPs, a gold salt solution was prepared by diluting 1 mL $HAuCl_4$ solution (0.236 M; $HAuCl_4 \cdot 3H_2O$, 99.9+%, Sigma-Aldrich; dissolved in water at room temperature) in 80 mL Nanopure water (>18.0 MΩ-cm, Barnstead NANOpure Diamond). A second solution was prepared by dissolving 0.04 g trisodium citrate (>99.5%, Fisher), 0.05 g tannic acid (>99.5%, Sigma-Aldrich), and 0.018 g potassium carbonate (>99.5%, Sigma-Aldrich) in 20 mL Nanopure water. Both solutions were heated in a 60-°C water bath and remained at 60 °C for at least 5 min before mixing together. The overall fluid was kept stirring vigorously, and was heated to boil for 20 min before removed from the heat source. The color of the heated overall fluid, as observed, changed with time—from light yellow to reddish, brown, and finally dark brown. Au NPs in the final fluid were of 4-nm size in diameter according to transmission electron microscopy (TEM) analysis as previously reported [1, 2]. Elemental analysis, conducted on randomly selected NP samples using a PerkinElmer inductively coupled plasma optical emission spectrometer (ICP-OES) Optima 4300 DV, indicated >95% of Au salt precursor was in the NP form [3]. The concentration of the final Au NP suspension was calculated to be 1.07×10^{14} NP/mL, based on a 100% reduction of Au precursor into NPs.

Pd coating was then applied on the Au NPs to form Pd/Au NPs. A certain amount (28.5-155.1 μL) of H_2PdCl_4 solution (0.00240 M; $PdCl_2$, 99.99%, Sigma-Aldrich;

dissolved in 0.005 M $HCl_{(aq)}$ at room temperature with moderate stirring) was mixed with 2 mL Au NP suspension (1.07×10^{14} NP/mL), followed by bobbling with hydrogen gas (99.99%, Matheson) for 2 min, and then left at room temperature (22 ± 2 °C) overnight. Previous TEM analysis showed no significant difference of size distribution after Pd coating [2]; ICP results indicated >95% of Pd salt precursor was reduced and incorporated into the Pd/Au NPs [3]. Assuming 100% conversion of Pd precursor, charged amounts of H_2PdCl_4 solution (28.5, 38.0, 57.0, 76.0, 95.0, and 155.1 μL) would lead to specific Pd surface monolayer (ML) coverages (30%, 40%, 60%, 80%, 100%, and 150% ML), with the modeled NP consisting of 7 complete shells of Au atoms and additional Pd shell(s) of different coverages [1].

Pd NPs were synthesized in the same manner as Au NPs, with the replacement of the gold salt solution by a palladium salt solution. The palladium salt solution was prepared by diluting 12 mL H_2PdCl_4 solution (0.00240 M) with 68 mL Nanopure water. The color of the heated overall fluid also changed with time, from light yellow to brown. TEM analysis confirmed the 4-nm size in diameter [2]; ICP results indicated >95% of Pd salt precursor was in the NP form [3]. The concentration of the final Pd NP suspension was calculated to be 1.22×10^{14} NP/mL, based on a 100% reduction of Pd precursor into NPs.

4.2.1.2. Immobilization of NP catalysts

Colloidal NPs were immobilized on carbon powder in the following procedure. 0.2 g carbon powder (Vulcan XC-72, Cabot) was dispersed in 5 mL Nanopure water under ultrasonication for 5 min. NP suspension (Pd/Au NPs with a certain Pd coverage, or Pd NPs) was added to the carbon powder dispersion; resulting mixture was ultrasonicated for

30 min and then stirred with a magnetic stir bar for 2 hr. Thereafter, the mixture was centrifuged under 12000 rpm (revolutions per minute) at 4 °C for 20 min (Thermo Scientific Sorvall Legend X1R centrifuge with FiberLite F15-8x50cy rotor); the precipitate was freeze-dried at −50 °C with a vacuum pressure 0.066 mbar (Labconco FreeZone 4.5 L console freeze dry system) to generate NP-containing carbon powders (NP/C). NP/C samples were stored at room temperature in a desiccation cabinet with $CaSO_4/CaCl_2$ desiccants (Drierite, W. A. Hammond). ICP results of NP/C samples indicated that >90% NPs were immobilized on the carbon powder. Table 4.1 shows the sample list with final solid compositions.

Table 4.1. Sample list with metal contents, dispersion, and charge amounts.

Catalyst	Au weight loading (wt%)	Pd weight loading (wt%)	Estimated Pd dispersion per NP (% surface Pd atoms)	Calculated amount of surface Pd atoms charged to reactor (μmol)
Pd/Au NPs (30% ML)/C	9.6	0.7	100[a]	3.2
Pd/Au NPs (40% ML)/C	9.6	0.9	100[a]	3.2
Pd/Au NPs (60% ML)/C	9.5	1.4	100[a]	3.2
Pd/Au NPs (80% ML)/C	9.5	1.9	100[a]	3.2
Pd/Au NPs (100% ML)/C	9.5	2.3	100[a]	3.2
Pd/Au NPs (150% ML)/C	9.3	3.7	69[b]	3.2
Pd NPs/C	0	4.7	27[c]	3.2

[a] Pd atoms assumed to be fully accessible on Au NP surface with Pd coverage ≤100% ML.
[b] Pd atoms assumed to be arranged as the magic cluster model [1]: 50% accessible in the fully occupied 8th shell (642 atoms), and 100% accessible in the half occupied 9th shell (406 atoms). ((642 × 50%) + 406) / (642 + 406) = 69%.
[c] Calculated from dispersion $D = c/d$ (c is a constant 1.1 for Pd; d is the particle size 4 nm) [4, 5].

4.2.2. Catalyst characterization

4.2.2.1. Transmission electron microscopy (TEM)

Selected samples were characterized with a JEOL 2010 transmission electron microscope to show the particle size and morphology before and after heat treatment; two sets of Pd/Au NPs (60% ML)/C were chosen: (1) as prepared, and (2) after heated in H_2 flow at

400 °C (samples taken from the heat treatment process in Sec. 4.2.3). NP/C powder was dispersed in isopropanol with ultrasonication, then deposited on a 200-mesh carbon/formvar TEM grid, and air-dried at room temperature. TEM was done with help from Ms. L. A. Pretzer.

4.2.2.2. Thermo-gravimetric analysis (TGA)

Decomposition of compounds in NP/C samples at high temperatures was measured with a TA Instruments SDT Q600 simultaneous thermo-gravimetric analysis and differential scanning calorimetry (TGA/DSC). Pd/Au NPs (60% ML)/C and the carbon support (Vulcan XC-72) were selected to show weight loss during heat treatment; two processes were performed: (1) heated from room temperature (~22 °C) to 410 °C at temperature ramp 3 °C/min in Ar flow (100 mL/min), and (2) heated from room temperature (~22 °C) to 410 °C at temperature ramp 3 °C/min in Ar flow (100 mL/min) with additional 30-min isothermal intervals at 100 °C, 200 °C, 300 °C, and 400 °C.

4.2.2.3. X-ray absorption spectroscopy (XAS)

X-ray absorption measurements were conducted on the insertion-device beamline 10-ID-B of the Materials Research Collaborative Access Team (MRCAT) at the Advanced Photon Source at Argonne National Laboratory. A cryogenically cooled double-crystal Si (111) monochromator was used in conjunction with an uncoated glass mirror to minimize the presence of harmonics. The monochromator was scanned continuously during the measurements with data points integrated over 0.5 eV for 0.07 sec per data point. Measurements were made in transmission mode with the ionization chambers optimized for the maximum current with linear response (~10^{10} photons detected per sec) using a mixture of N_2 and He in the incident X-ray detector and a mixture of ~20% Ar in N_2 in

the transmission X-ray detector. Absorption was measured at both Au and Pd edges; a Au or Pd foil spectrum was acquired simultaneously with each measurement for energy calibration.

NP/C samples were pressed into a cylindrical holder with a thickness chosen to give a total absorbance (μx) at the Au L_{III} (11.918 keV) and Pd K (24.350 keV) edges of ca. 2.0, and an edge step ($\Delta\mu x$) of ca. 0.5. The sample holder was placed in a continuous-flow reactor cell (glass tube, length 18 in., diameter 0.75 in.) fitted at both ends with polyimide windows and stainless steel valves to isolate the reactor from the atmosphere. Each sample was treated and measured with the following procedure. (1) The reactor cell was first filled with H_2, and samples were analyzed as-prepared in H_2 at room temperature (RT). (2) The reactor cell was applied with a H_2 flow (100 mL/min) and placed in a 100-°C furnace. After reaching 100 °C for 30 min, the reactor cell was cooled down to room temperature, and then sealed with H_2 filled inside, followed by XAS measurements. (3) Repeat Step 2 but at 200 °C. (4) Repeat Step 2 but at 300 °C. (5) Repeat Step 2 but in He (100 mL/min) at 300 °C. (6) Repeat Step 2 but in air (100 mL/min) at 300 °C. (7) Repeat Step 2 but in H_2 (100 mL/min) at 400 °C. All spectra were obtained at room temperature.

Experimental phase shifts and back-scattering amplitudes were obtained from reference compounds: Au foil for Au-Au bonding, Pd foil for Pd-Pd bonding, and $Pd(NH_3)_4(NO_3)_2$ (Aldrich) for Pd-O bonding. Experimental data of Au and Pd foil were used to determine the best fit of Debye-Waller factors (DWF's) and amplitude reduction factors (S_o) for phase shifts and back-scattering amplitudes in the FEFF fitting [6]. Along with the bond distance for Au and Pd foil, these values were used for determining the Au-

Pd and Pd-Au FEFF phase shifts and back-scattering amplitudes. Standard procedures based on the WINXAS97 software [6] were used to extract the data [7]. The coordination parameters were obtained by a least-square fit in the *k*- and *R*-spaces of the nearest-neighbor, k^2-weighted Fourier transform (FT) data (*k*: photoelectron wave number, *R*: bond distance). The data fitted equally well with both k^1 and k^3 weightings. For the bimetallic Pd/Au samples, the EXAFS fitting was verified that, within error, the data from both Au and Pd edges led to the same bond distances, the same DWF's, and self-consistent coordination numbers for Au-Pd and Pd-Au bonds [8].

4.2.3. Catalyst testing

NP/C samples underwent a series of heat treatment processes as shown in Scheme 4.1. (1) Samples were placed in a glass tube with a H_2 flow (100 mL/min), heated in a furnace from room temperature (~22 °C) to 100 °C at temperature ramp 3 °C/min, and then remained at 100 °C for 30 min. Samples were cooled down to room temperature in the tube with the H_2 flow before a fraction was taken for the catalyst testing. (2) Repeat Step 1 but to 200 °C, for the remaining sample. (3) Repeat Step 1 but to 300 °C, for the remaining sample. (4) Repeat Step 1 but to 400 °C for the remaining sample. (5) Repeat Step 1-4 but in a He flow (100 mL/min). Such cumulative process was used in order to make it the same as the process for XAS samples.

The model reaction for catalyst testing was room-temperature aqueous-phase hydrodechlorination (HDC) of trichloroethene (TCE); batch tests were performed similar to our previous studies [1, 2, 9]. A screw-cap bottle (250 mL, Alltech), containing 165 mL Nanopure water, 3 mL $NaHCO_{3(aq)}$ buffer (0.08 M; $NaHCO_3$, 99%, Fisher), and a magnetic stir bar, were sealed with PTFE-sealed threads and a PTFE-silicone septum.

Hydrogen gas was bubbled into the bottle for 15 min to displace dissolved oxygen and to fill the headspace with a hydrogen atmosphere (1 atm). Then, 7 μL TCE (99.5%, Sigma-Aldrich) and 0.2 μL pentane (99.7%, Burdick and Jackson), as the internal standard, were injected into the sealed bottle. The overall solution was stirred for at least 3 hr to reach equilibrium.

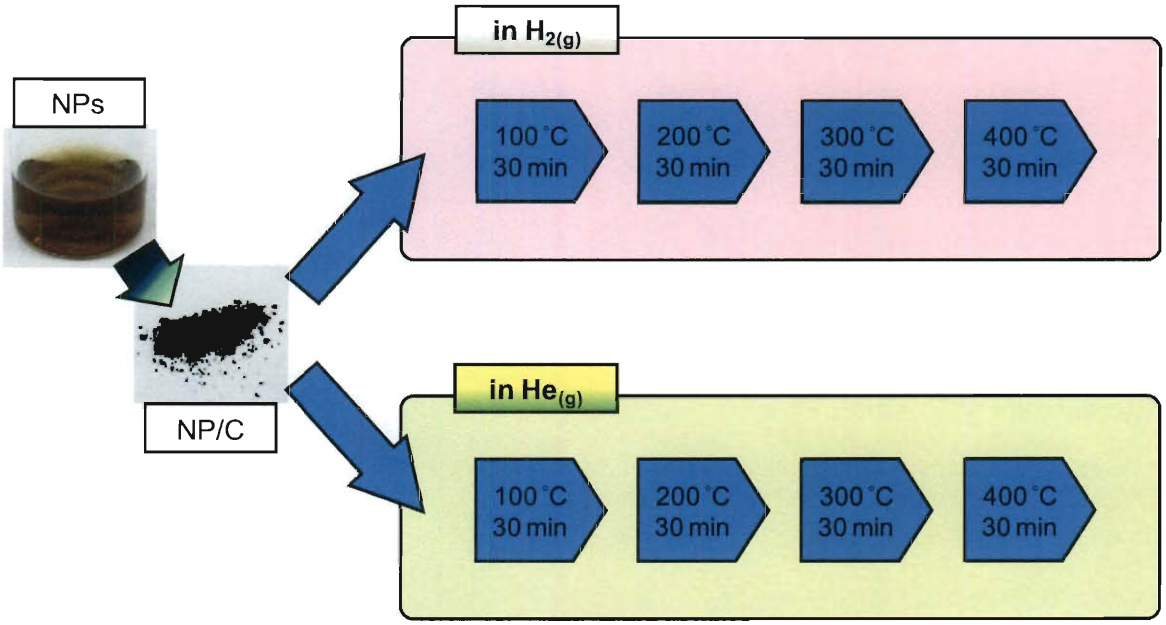

Scheme 4.1. Procedure of heat treatment processes for NP/C samples.

In a separate vial, ~50 mg catalyst powder was dispersed in a mixture of 4.5 mL Nanopure water and 0.5 mL isopropanol with ultrasonication for 1 min. Charged catalyst amounts were controlled to have the same surface Pd charge (3.2 μmol, Table 4.1) among all the samples. At time $t = 0$, catalyst suspension was injected into the bottle with the stir rate at 600 rpm. The initial TCE concentration in liquid phase was 50.9 ppm, far below the saturation concentration of 1200 ppm in water at 25 °C [10].

The reaction was monitored through headspace gas chromatography (GC) using an Agilent Technologies 6890N GC with a flame ionization detector (FID) and a 60/80 Carbopack B/1% SP-1000 packed column (Supelco 12487, Sigma-Aldrich). Samples were taken from the headspace (gas phase) of the reactor, and then injected into GC to determine quantities of TCE and other compounds (>90% selectivity to ethane [1]). Reaction rates were determined from changes of TCE concentrations in the headspace. All reactions were performed at room temperature.

4.3. Results and discussion

4.3.1. Particle size and morphology

Selected as-prepared NP/C exhibited spherical NPs around 4 nm (Fig. 4.1a); 400-°C heat-treated NP/C showed ~30% particles became larger around 10-20 nm with a little irregular shapes while others remained spherical around 4 nm (Fig. 4.1b). EXAFS results also suggested the particle sizes became larger above 200 °C since the total coordination numbers of Au ($N_{Au} = N_{Au\text{-}Au} + N_{Au\text{-}Pd}$) for each sample increased with the treatment temperatures (see below, Sec. 4.3.3 and Table 4.4). As the Pd/Au NPs were mainly composed of Au, larger particle sizes would lead to higher N_{Au} values [2, 11].

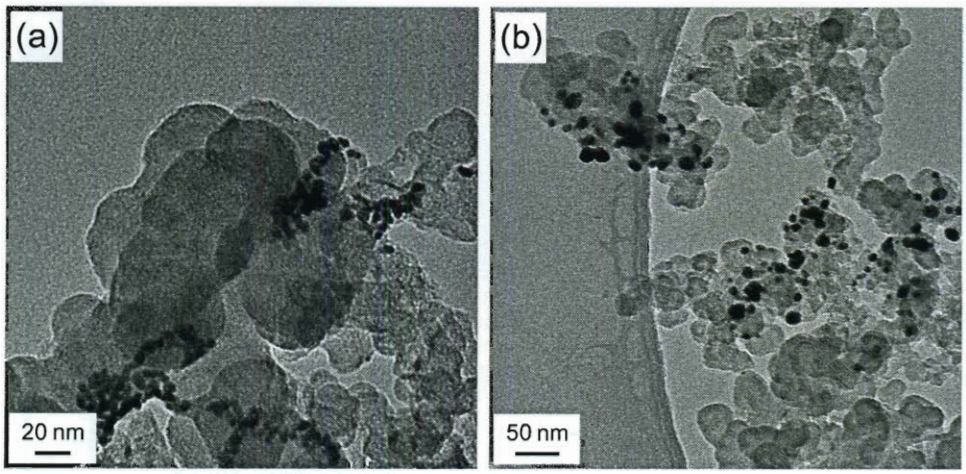

Figure 4.1. Representative TEM images of Pd/Au NPs (60% ML)/C (a) as prepared, and (b) after heated in H_2 flow at 400 °C. (Courtesy of Ms. L. A. Pretzer)

Table 4.2. EXAFS fit parameters (*N*: coordination number, *R*: bond distance, RT: room temperature).

Catalyst	Edge	Treatment for XAS	Scattering path	*N* (±10%)	*R* (Å) (±0.02 Å)
Pd/Au NPs (30% ML)/C	Au	H_2 RT	Au-Au	8.9	2.85
			Au-Pd	1.1	2.79
		H_2 100 °C	Au-Au	8.9	2.85
			Au-Pd	1.2	2.79
		H_2 200 °C	Au-Au	9.5	2.85
			Au-Pd	1.6	2.80
		H_2 300 °C	Au-Au	9.5	2.85
			Au-Pd	1.7	2.81
		H_2 400 °C	Au-Au	9.5	2.85
			Au-Pd	1.9	2.81
	Pd	H_2 RT	Pd-Pd	1.7	2.76
			Pd-Au	8.9	2.81
		H_2 100 °C	Pd-Pd	1.8	2.76
			Pd-Au	8.9	2.81
		H_2 200 °C	Pd-Pd	1.4	2.76
			Pd-Au	9.6	2.81
		H_2 300 °C	Pd-Pd	1.3	2.76
			Pd-Au	10.7	2.81
		He 300 °C	Pd-Pd	1.2	2.76
			Pd-Au	10.8	2.81
		H_2 400 °C	Pd-Pd	1.2	2.76
			Pd-Au	10.7	2.81
Pd/Au NPs (60% ML)/C	Au	H_2 RT	Au-Au	9.6	2.86
			Au-Pd	1.3	2.80
		H_2 100 °C	Au-Au	9.2	2.85
			Au-Pd	1.6	2.80
		H_2 200 °C	Au-Au	9.2	2.85
			Au-Pd	2.3	2.80
		H_2 300 °C	Au-Au	9.2	2.84
			Au-Pd	2.7	2.80

		He 300 °C	Au-Au	9.2	2.84
			Au-Pd	2.6	2.79
		Air 300 °C	Au-Au	9.2	2.84
			Au-Pd	2.6	2.80
		H_2 400 °C	Au-Au	9.6	2.84
			Au-Pd	2.7	2.80
	Pd	H_2 RT	Pd-Pd	2.9	2.76
			Pd-Au	6.7	2.81
		H_2 100 °C	Pd-Pd	3.1	2.76
			Pd-Au	6.7	2.81
		H_2 200 °C	Pd-Pd	3.0	2.76
			Pd-Au	9.3	2.81
		H_2 300 °C	Pd-Pd	2.3	2.76
			Pd-Au	10.3	2.81
		He 300 °C	Pd-Pd	2.4	2.76
			Pd-Au	10.4	2.81
		Air 300 °C	Pd-Pd	2.5	2.76
			Pd-Au	10.6	2.81
		H_2 400 °C	Pd-Pd	2.1	2.76
			Pd-Au	9.9	2.81
Pd/Au NPs (80% ML)/C	Au	H_2 RT	Au-Au	9.7	2.86
			Au-Pd	1.4	2.79
		H_2 100 °C	Au-Au	9.4	2.85
			Au-Pd	1.6	2.79
		H_2 200 °C	Au-Au	9.4	2.85
			Au-Pd	2.1	2.79
		H_2 300 °C	Au-Au	9.6	2.84
			Au-Pd	2.6	2.79
		He 300 °C	Au-Au	9.5	2.84
			Au-Pd	2.6	2.79
		Air 300 °C	Au-Au	9.3	2.84
			Au-Pd	2.7	2.80
		H_2 400 °C	Au-Au	9.6	2.84
			Au-Pd	3.0	2.80
	Pd	H_2 RT	Pd-Pd	3.3	2.76
			Pd-Au	6.2	2.81
		H_2 100 °C	Pd-Pd	3.3	2.76
			Pd-Au	6.1	2.81
		H_2 200 °C	Pd-Pd	3.5	2.76
			Pd-Au	8.0	2.81
		H_2 300 °C	Pd-Pd	3.3	2.76
			Pd-Au	9.3	2.81
		He 300 °C	Pd-Pd	3.5	2.76
			Pd-Au	8.8	2.81
		Air 300 °C	Pd-Pd	3.1	2.76
			Pd-Au	8.0	2.81
		H_2 400 °C	Pd-Pd	2.8	2.76
			Pd-Au	9.0	2.81
Pd/Au NPs (150% ML)/C	Au	H_2 RT	Au-Au	9.6	2.85
			Au-Pd	1.6	2.79
		H_2 100 °C	Au-Au	9.3	2.85
			Au-Pd	1.9	2.79
		H_2 200 °C	Au-Au	9.1	2.84
			Au-Pd	2.4	2.79

		H_2 300 °C	Au-Au	9.3	2.84
			Au-Pd	3.1	2.80
		He 300 °C	Au-Au	9.1	2.84
			Au-Pd	3.1	2.80
		Air 300 °C	Au-Au	9.5	2.84
			Au-Pd	3.1	2.79
		H_2 400 °C	Au-Au	9.5	2.84
			Au-Pd	3.5	2.80
	Pd	H_2 RT	Pd-Pd	5.6	2.79
			Pd-Au	4.6	2.81
		H_2 200 °C	Pd-Pd	5.2	2.79
			Pd-Au	4.6	2.81
		H_2 300 °C	Pd-Pd	5.1	2.79
			Pd-Au	6.1	2.81
		He 300 °C	Pd-Pd	5.6	2.76
			Pd-Au	5.8	2.81
		Air 300 °C	Pd-Pd	5.4	2.76
			Pd-Au	5.5	2.81
		H_2 400 °C	Pd-Pd	5.0	2.79
			Pd-Au	6.3	2.81

4.3.2. Weight loss due to heat treatment

TGA results showed that NP/C had weight loss at higher temperatures while the carbon support was stable with little weight loss below 400 °C (Fig. 4.2a). Such weight loss was possibly due to decomposition of the organic compounds as reducing agents and surface stabilizers for the colloidal NPs. For the quantification purpose in the TCE HDC testing, the step-type heat treatment was conducted to show weight loss (0.0%, 1.6%, 4.5%, and 6.3%) after 30-min isothermal intervals at 100 °C, 200 °C, 300 °C, and 400 °C, separately (Fig. 4.2b). The weight profile indicated that 30-min heating was long enough to reach a steady state of weight at a certain temperature (Fig. 4.2b).

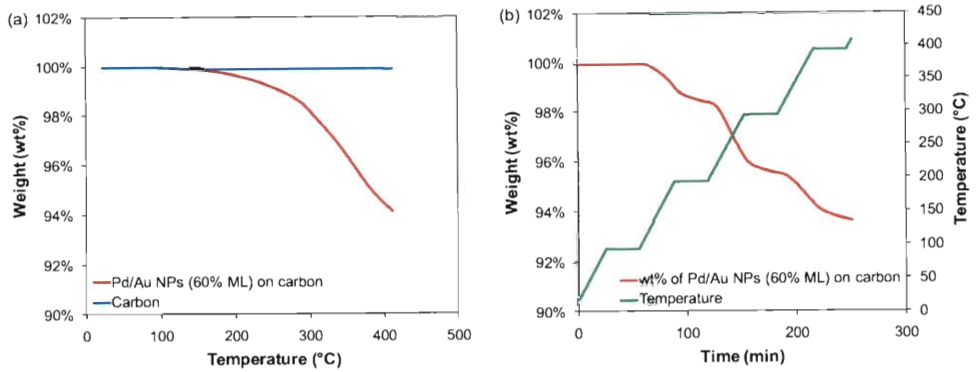

Figure 4.2. TGA weight loss profiles of (a) Pd/Au NPs (60% ML)/C and the carbon support (XC-72) under heat treatment from room temperature (~22 °C) to 410 °C at temperature ramp 3 °C/min in Ar flow (100 mL/min), and (b) Pd/Au NPs (60% ML)/C heated from room temperature (~22 °C) to 410 °C at temperature ramp 3 °C/min in Ar flow (100 mL/min) with additional 30-min isothermal intervals at 100 °C, 200 °C, 300 °C, and 400 °C.

4.3.3. Catalyst nanostructure from XAS measurements

As one of the powerful techniques for catalyst characterization, XAS has the ability to acquire detailed structural and electronic information at an atomic level for monometallic NPs [12-14] and bimetallic NPs [2, 15-26]. XAS contains two regions: (1) the X-ray absorption near-edge structure (XANES) region, revealing information about oxidation state and electron distribution, and (2) the extended X-ray absorption fine structure (EXAFS) region, providing local structural information including neighboring atom (in terms of scattering path), coordination number (*N*), and bond distance (*R*).

Fig. 4.3 shows representative XANES and EXAFS data for Pd/Au NPs/C. For XANES (Fig. 4.3a), the identical intensities of the first peak between the Pd/Au sample and Pd foil indicated that Pd was fully reduced for the Pd/Au sample; the shifts in position and shape suggested a second metallic scattering, which resulted from the bimetallic Pd/Au composition. For EXAFS (Fig. 4.3b), the magnitude and imaginary components of the Fourier transform data were very different between the Pd/Au sample

and Pd foil, indicating the presence of Au neighbors around Pd atoms. All Pd/Au samples exhibited above major characteristics; detailed results of EXAFS fitting were listed in Table 4.2.

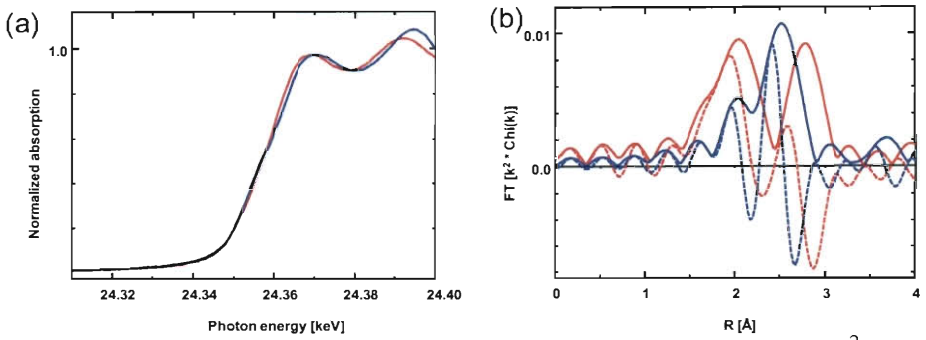

Figure 4.3. (a) XANES spectra of Pd K edge and (b) Fourier transform (k^2 weighted, Δk = 2.8-11.0 Å^{-1}; solid line: magnitude, dotted line: imaginary components) of Pd K edge EXAFS data for Pd foil (blue) and Pd/Au NPs (80% ML)/C (red; after heated in He at 300 °C). Values of Fourier transform of Pd foil were ×0.25 of original data for comparison purpose.

With analysis of EXAFS fitting results, bimetallic catalyst nanostructures can be revealed in the ways including core-shell, surface alloy, or bulk alloy; we reported such method previously [2] and applied in this work. For our bimetallic Pd/Au NP system, the total coordination number of Au or Pd (N_{Au} or N_{Pd}) can be calculated as follows.

$$N_{Au} = N_{Au\text{-}Au} + N_{Au\text{-}Pd} \quad (1)$$

$$N_{Pd} = N_{Pd\text{-}Pd} + N_{Pd\text{-}Au} \quad (2)$$

If the bimetallic Pd-Au system is bulk alloy—all atoms are randomly distributed, the coordination number of each bonding to a certain element should be proportional to the molar fraction (x) of the element; that is,

$$N_{Au\text{-}Au,\,bulk} = N_{Au} \times x_{Au} \quad (3)$$

$$N_{\text{Au-Pd, bulk}} = N_{\text{Au}} \times x_{\text{Pd}} \quad (4)$$

$$N_{\text{Pd-Pd, bulk}} = N_{\text{Pd}} \times x_{\text{Pd}} \quad (5)$$

$$N_{\text{Pd-Au, bulk}} = N_{\text{Pd}} \times x_{\text{Au}} \quad (6)$$

Au is the major composition, decorated with some Pd atoms, in our Pd/Au NP system. From the Au edge, if the measured $N_{\text{Au-Au}}$ is greater than $N_{\text{Au-Au, bulk}}$ and the measured $N_{\text{Au-Pd}}$ is less than $N_{\text{Au-Pd, bulk}}$, the Pd/Au NPs can be suggested as a Au-rich core (and, therefore, a Pd-rich shell). If the measured $N_{\text{Au-Au}}$ and $N_{\text{Au-Pd}}$ are similar to $N_{\text{Au-Au, bulk}}$ and $N_{\text{Au-Pd, bulk}}$, the Pd/Au NPs can be suggested as a bulk alloy structure.

From the Pd edge, if the measured $N_{\text{Pd-Pd}}$ is greater than $N_{\text{Pd-Pd, bulk}}$ and the measured $N_{\text{Pd-Au}}$ is less than $N_{\text{Pd-Au, bulk}}$, the Pd/Au NPs can be suggested to have Pd islands (or ensembles, aggregates). If the measured $N_{\text{Pd-Pd}}$ and $N_{\text{Pd-Au}}$ are similar to $N_{\text{Pd-Pd, bulk}}$ and $N_{\text{Pd-Au, bulk}}$, Pd atoms in the Pd/Au NPs can be suggested to have neighbor atoms randomly distributed as Au or Pd (local alloy).

Coordination number percentage ($N\%$) was defined for simpler presentation.

$$N\%_{\text{Au-Au}} = N_{\text{Au-Au}} / N_{\text{Au}} = N_{\text{Au-Au}} / (N_{\text{Au-Au}} + N_{\text{Au-Pd}}) \quad (7)$$

$$N\%_{\text{Pd-Pd}} = N_{\text{Pd-Pd}} / N_{\text{Pd}} = N_{\text{Pd-Pd}} / (N_{\text{Pd-Pd}} + N_{\text{Pd-Au}}) \quad (8)$$

$$N\%_{\text{Au-Au, bulk}} = N_{\text{Au-Au, bulk}} / N_{\text{Au}} = x_{\text{Au}} \quad (9)$$

$$N\%_{\text{Pd-Pd, bulk}} = N_{\text{Pd-Pd, bulk}} / N_{\text{Pd}} = x_{\text{Pd}} \quad (10)$$

Therefore, guidelines for determining catalyst nanostructures can be summarized as follows: (1) $N\%_{\text{Au-Au}} > x_{\text{Au}}$: Au-rich core, Pd-rich shell; (2) $N\%_{\text{Au-Au}} \approx x_{\text{Au}}$: bulk PdAu alloy; (3) $N\%_{\text{Pd-Pd}} > x_{\text{Pd}}$: Pd islands; (4) $N\%_{\text{Pd-Pd}} \approx x_{\text{Pd}}$: local PdAu alloy. Table 4.3 shows

molar fractions in NP/C samples. Table 4.4 and 4.5 list calculated results of the *N%* parameters mentioned above for the Au and Pd edges, separately. Fig. 4.4 shows plots demonstrating changes of *N%* after treatments at different temperatures. Table 4.6 concludes catalyst nanostructures of samples with different treatments, according to the above guidelines.

Table 4.3. Molar fractions (x) of metal elements in Pd/Au NP samples.

Catalyst	x_{Au}	x_{Pd}
Pd/Au NPs (30% ML)/C	88%	12%
Pd/Au NPs (60% ML)/C	79%	21%
Pd/Au NPs (80% ML)/C	73%	27%
Pd/Au NPs (150% ML)/C	57%	43%

Table 4.4. Analysis of coordination numbers (*N*) for Au edge.

Catalyst	Treatment for XAS	N_{Au-Au}	N_{Au-Pd}	N_{Au}	$N\%_{Au-Au}$
Pd/Au NPs (30% ML)/C	H_2 RT	8.9	1.1	10.0	89%
	H_2 100 °C	8.9	1.2	10.1	88%
	H_2 200 °C	9.5	1.6	11.1	86%
	H_2 300 °C	9.5	1.7	11.2	85%
	H_2 400 °C	9.5	1.9	11.4	83%
Pd/Au NPs (60% ML)/C	H_2 RT	9.6	1.3	10.9	88%
	H_2 100 °C	9.2	1.6	10.8	85%
	H_2 200 °C	9.2	2.3	11.5	80%
	H_2 300 °C	9.2	2.7	11.9	77%
	H_2 400 °C	9.6	2.7	12.3	78%
Pd/Au NPs (80% ML)/C	H_2 RT	9.7	1.4	11.1	87%
	H_2 100 °C	9.4	1.6	11.0	85%
	H_2 200 °C	9.4	2.1	11.5	82%
	H_2 300 °C	9.6	2.6	12.2	79%
	H_2 400 °C	9.6	3.0	12.6	76%
Pd/Au NPs (150% ML)/C	H_2 RT	9.6	1.6	11.2	86%
	H_2 100 °C	9.3	1.9	11.2	83%
	H_2 200 °C	9.1	2.4	11.5	79%
	H_2 300 °C	9.3	3.1	12.4	75%
	H_2 400 °C	9.5	3.5	13.0	73%

Table 4.5. Analysis of coordination numbers (*N*) for Pd edge.

Catalyst	Treatment for XAS	N_{Pd-Pd}	N_{Pd-Au}	N_{Pd}	$N\%_{Pd-Pd}$
Pd/Au NPs (30% ML)/C	H_2 RT	1.7	8.9	10.6	16%
	H_2 100 °C	1.8	8.9	10.7	17%
	H_2 200 °C	1.4	9.6	11.0	13%
	H_2 300 °C	1.3	10.7	12.0	11%
	H_2 400 °C	1.2	10.7	11.9	10%
Pd/Au NPs (60% ML)/C	H_2 RT	2.9	6.7	9.6	30%
	H_2 100 °C	3.1	6.7	9.8	32%
	H_2 200 °C	3.0	9.3	12.3	24%
	H_2 300 °C	2.3	10.3	12.6	18%
	H_2 400 °C	2.1	9.9	12.0	18%
Pd/Au NPs (80% ML)/C	H_2 RT	3.3	6.2	9.5	35%
	H_2 100 °C	3.3	6.1	9.4	35%
	H_2 200 °C	3.5	8.0	11.5	30%
	H_2 300 °C	3.3	9.3	12.6	26%
	H_2 400 °C	2.8	9.0	11.8	24%
Pd/Au NPs (150% ML)/C	H_2 RT	5.6	4.6	10.2	55%
	H_2 200 °C	5.2	4.6	9.8	53%
	H_2 300 °C	5.1	6.1	11.2	46%
	H_2 400 °C	5.0	6.3	11.3	44%

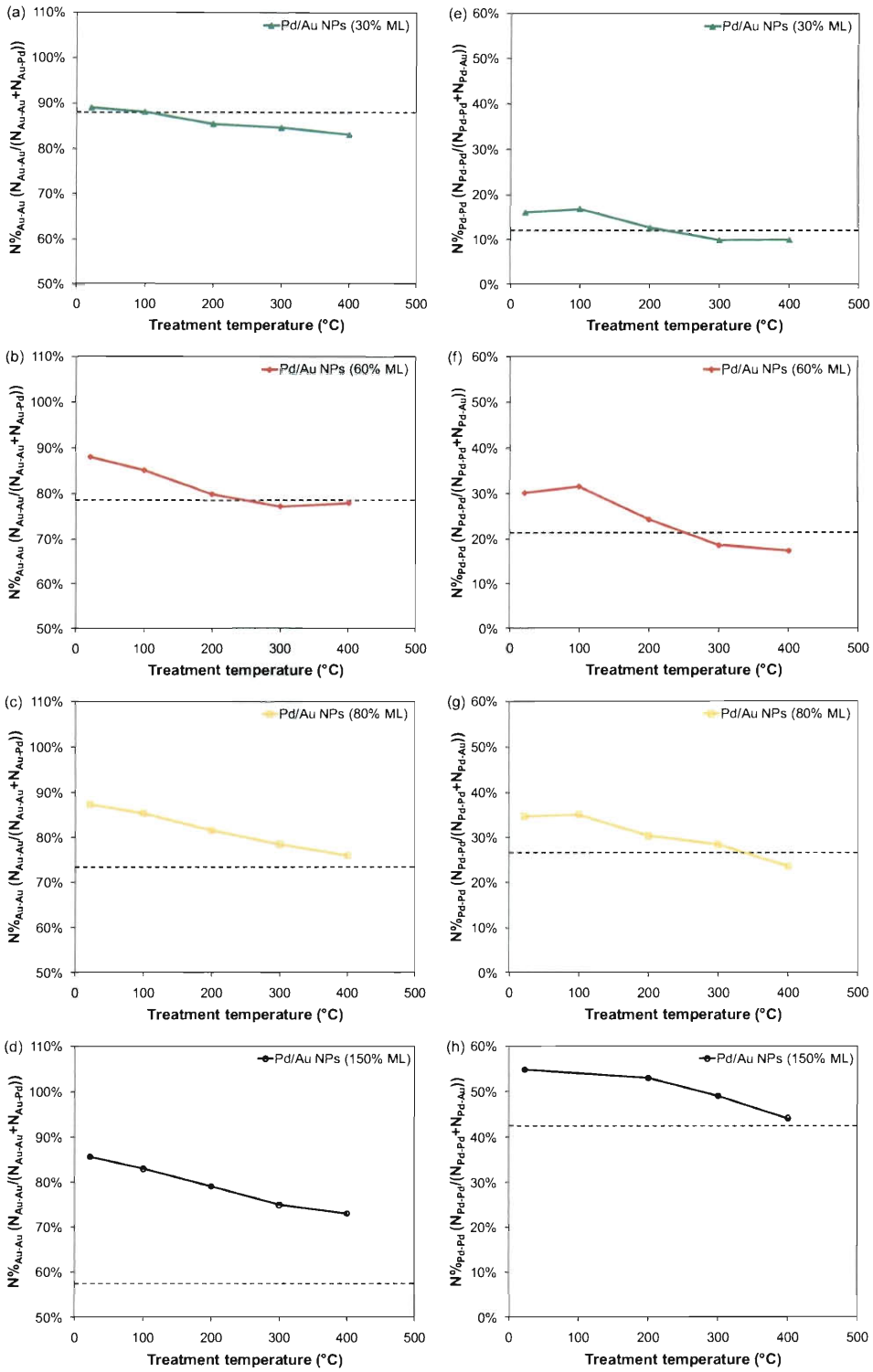

Figure 4.4. Profiles of coordination number percentages (N%) at different treatment temperatures for (a-d) $N\%_{Au\text{-}Au}$ at Au edge and (e-h) $N\%_{Pd\text{-}Pd}$ at Pd edge of Pd/Au NPs/C samples with (a, e) 30% ML, (b, f) 60% ML, (c, g) 80% ML, and (d, h) 150% ML (dotted line: molar fractions of Au at Au edge or of Pd at Pd edge).

Table 4.6. Proposed catalyst nanostructures of samples with different treatment temperatures (C: Au-rich core, Pd-rich shell; B: bulk PdAu alloy; I: Pd islands; L: local PdAu alloy).

Catalyst	Treatment temperature				
	RT	100 °C	200 °C	300 °C	400 °C
Pd/Au NPs (30% ML)/C	C / I	C / I	B / L	B / L	B / L
Pd/Au NPs (60% ML)/C	C / I	C / I	B / L	B / L	B / L
Pd/Au NPs (80% ML)/C	C / I	C / I	C / I	C / L	B / L
Pd/Au NPs (150% ML)/C	C / I	C / I	C / I	C / I	C / L

As shown in Fig. 4.4a-d, $N\%_{Au\text{-}Au}$ values decreased with treatment temperatures for all coverages, indicating nanostructure transition from Au-rich core with Pd-rich shell to bulk PdAu alloy; in Fig. 4.4e-h, $N\%_{Pd\text{-}Pd}$ values also decreased with treatment temperatures for all coverages, indicating nanostructure transition from Pd islands to local PdAu alloy. Combining information from the Au and Pd edges, Table 4.6 shows that as-prepared Pd/Au NPs of all coverages had a core-shell (Au-rich core, Pd-rich shell) structure with Pd islands on the shell (C / I); at higher temperatures, Pd islands would mix with Au to form surface PdAu alloy (C / L) and further full bulk PdAu alloy (B / L). Pd islands at lower coverages tended to mix with Au more easily; that is, samples could become surface or bulk PdAu alloy at lower temperatures. For a simplified expression, samples with $N\% = x \pm 3\%$ would be recognized as $N\% \approx x$ and applied for the guidelines (Table 4.6), except for Pd/Au 30% ML at the Au edge. As shown in Fig. 4.4a, all $N\%_{Au\text{-}Au}$ points of Pd/Au 30% ML at the Au edge were close to x_{Au} or below x_{Au} ~5%. The minimum of $N\%_{Au\text{-}Au}$ should be around x_{Au} theoretically, as for the bulk alloy case. We speculate that $N\%_{Au\text{-}Au}$ values of Pd/Au 30% ML were underestimated and actual values should be higher for ~5% to make the smallest $N\%_{Au\text{-}Au}$ value close to x_{Au}; results in Table 4.6 were determined according to this speculation. Such shifts might be due to the

large fraction of Au (x_{Au} ~90%) and the small fraction of Pd (x_{Pd} ~10%) in Pd/Au 30% ML, in which EXAFS was less sensitive for the bimetallic samples. Nevertheless, the downtrends of N% values in all samples at both Au and Pd edges confirmed that as-prepared Pd/Au NPs of all coverages had a core-shell (Au-rich core, Pd-rich shell) structure with Pd islands on the shell, and such Pd islands would gradually mix with Au to form surface and bulk PdAu alloy above 200 °C. Scheme 4.2 shows illustration for this structure change.

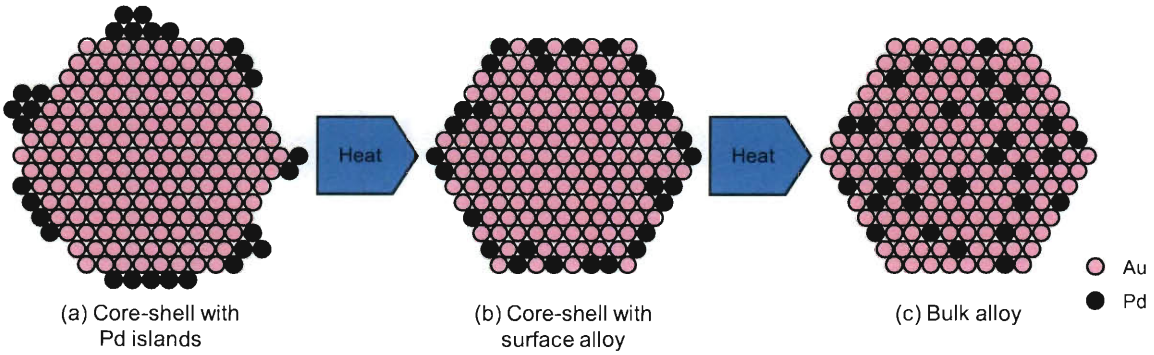

Scheme 4.2. Structure transition of Pd/Au NPs with heat treatment, as idealized cross-sections, for (a) core-shell (Au-rich core, Pd-rich shell) structure with Pd islands on the shell, (b) core-shell (Au-rich core, Pd-rich shell) structure with surface PdAu alloy, and (c) bulk PdAu alloy.

Oxidation resistance of Pd atoms was observed for all Pd coverages. No Pd-O was detected for as-prepared Pd/Au NP samples by EXAFS in H_2 at room temperature or above (Table 4.2) while Pd NPs showed almost fully oxidized surface Pd atoms at room temperature and could only be reduced in H_2 above 300 °C [2]. For better demonstration, Pd/Au samples of each coverage underwent heat processes at 300 °C in H_2, He, or air before XAS measurements. As listed in Table 4.2, EXFAS results were very similar among H_2, He, and air treatments; no Pd-O was detected for all tests, showing that Au

could stabilize metallic Pd atoms and prevent them from being oxidized in the Pd/Au NPs of different Pd coverages.

$R_{Au\text{-}Au}$ values of all Pd/Au samples with different treatments were similar (2.84-2.86 Å) and slightly less than Au foil (2.88 Å), which is typical for NPs. $R_{Pd\text{-}Pd}$ values of Pd/Au samples with different treatments were the same (2.76 Å), similar to Pd foil (2.75 Å), with exception for 150% ML in H_2 (2.79 Å), similar to Pd-H (2.80 Å) [27]. EXAFS data in He were for comparison purpose to see if there was Pd-H formed in H_2, as $R_{Pd\text{-}Pd}$ would become larger with Pd-H. For less Pd coverage (30%-80% ML), $R_{Pd\text{-}Pd}$ values were the same in H_2 and in He (2.76 Å), indicating no Pd-H formed in H_2; for 150% ML, $R_{Pd\text{-}Pd}$ value in H_2 (2.79 Å) was larger than in He (2.76 Å) and similar to Pd-H (2.80 Å), indicating Pd-H formed in H_2 atmosphere. Fig. 4.5 shows the FT imaginary part at the Pd edge of the 150%-ML sample in H_2 was shifted to higher R values, compared to that in He. This was an indication for longer bond distances ($R_{Pd\text{-}Pd}$) and multilayers of Pd atoms on the surface which could form Pd-H.

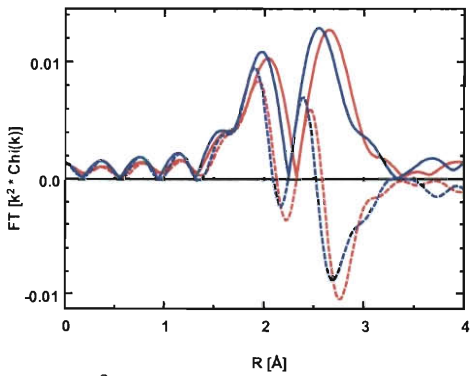

Figure 4.5. Fourier transform (k^2 weighted, Δk = 2.0-10.9 $Å^{-1}$; solid line: magnitude, dotted line: imaginary components) of Pd K edge EXAFS data for Pd/Au NPs (150% ML)/C after heated in He at 300 °C (blue) and after heated in H_2 at 300 °C (red).

Compared to our previous results [2], Pd/Au NPs (60% ML) showed some difference in this work. The 60%-ML sample in the previous work exhibited only surface PdAu alloy after heated in H_2 at 300 °C while the sample in this work exhibited bulk PdAu alloy. The reason might be that the heating process was 30 min at 300 °C in the previous work, and was 90 min (30 min each at 100, 200, 300 °C) in this work. Heat duration might be an issue for the structure transition. On the other hand, the as-prepared 60%-ML sample showed ~20% Pd oxidation in the previous work while it showed no observed Pd oxidation in this work. Since we did not prepare samples on site for XAS, there might be some unexpected situations during sample transportation in the previous work, resulting in slight oxidation. However, even 20% Pd oxidation was still showing much better oxidation resistance than ~100% surface oxidation in the Pd NPs [2], which was consistent of the finding in this work.

4.3.4. Catalytic activity for TCE HDC reaction

For the model reaction of TCE HDC, reaction activities were determined as rate constant k_{cat} and initial turnover frequency (TOF, number of reacted TCE molecules per Pd atom per second), with the implicit assumption of first-order dependence in TCE and zero-order in H_2 [1, 28-30]. Both expressions are used in related research articles [1, 28-31]; therefore, we report both for easier comparison with other works. k_{cat} is the Pd-normalized reaction rate constant (with unit of $L/g_{Pd}/min$), derived from Eqs. 11-12:

$$\text{reaction rate} = \frac{-\mathrm{d}C_{TCE}}{\mathrm{d}t} = k_{meas} C_{TCE} \tag{11}$$

$$k_{meas} = k_{cat} C_{cat} \tag{12}$$

where k_{meas} is the measured first-order rate constant, C_{TCE} and C_{cat} are the concentrations of TCE and Pd in the liquid phase in the reactor, respectively. Pd amounts used in both k_{cat} and initial TOF were the Pd atoms on the surface. Pd/Au NPs were modeled as magic clusters with face-centered cubic (FCC) structure; that is, one Pd/Au NP was consisted of 7 complete shells of gold atoms and an additional Pd shell of different coverages as we reported previously [1]. Therefore, Pd atoms were assumed to be fully accessible on the Au NP surface with Pd coverage ≤100% ML while they were 50% accessible in the fully occupied 8^{th} shell (642 atoms), and 100% accessible in the half occupied 9^{th} shell (406 atoms). For Pd NPs, surface Pd amounts were calculated from dispersion $D = c/d$ (c is a constant 1.1 for Pd; d is the particle size 4 nm) [4, 5]. Dispersion and calculated surface Pd amounts for each sample were listed in Table 4.1.

It is true that the real kinetics is more complicated [3]; nevertheless, rate constants and initial TOF's can be used to compare catalytic activities at a given TCE concentration and at an excess concentration of H_2 in the system [2, 3]. Dilute $NaHCO_{3(aq)}$ (~1.4 mM in the reactor) was chosen as the buffer, and pH was controlled between 8.3-6.0 for all the tests in order to minimize possible effects from salts and pH changes [32, 33]. All reactions with Pd/Au NPs or Pd NPs could reach >90% TCE conversion and show >90% product selectivity to ethane as we reported previously [1].

Results of catalyst activities are listed in Table 4.7; data points of initial TOF's with different Pd coverages and treatments are plotted in Fig. 4.6. Treatment in H_2 or He showed no significant difference between each other, and exhibited similar profiles of activity change with different Pd coverages and treatment temperatures. As-prepared Pd/Au NPs with 60-80% ML were the most active while Pd/Au NPs with more or less Pd

coverage led to lower activities. Such coverage dependence has been investigated in our previous work as the volcano-shape property of Pd/Au NPs [1]. Pd/Au NPs became less active with increasing treatment temperatures, especially above 200 °C, and finally reached common values above 300 °C for various coverages of Pd/Au NPs as well as Pd NPs.

Table 4.7. Reaction rates of catalyst samples with different treatments (rate constant k_{cat} and initial turnover frequency (TOF) determined from aqueous-phase TCE HDC with initial $[TCE]_{(aq)}$ = 50.9 ppm at room temperature 22 ± 2 °C; Pd amounts counted as surface Pd atoms listed in Table 4.1).

Catalyst	Treatment	Rate constant k_{cat} ($L/g_{Pd}/min$)	Initial TOF (10^{-3} $mol_{TCE}/mol_{Pd}/s$)
Pd/Au NPs (30% ML)/C	Air RT	36	25
	H_2 100 °C	39	27
	H_2 200 °C	34	23
	H_2 300 °C	140	99
	H_2 400 °C	210	140
	He 100 °C	32	22
	He 200 °C	30	21
	He 300 °C	160	110
	He 400 °C	190	130
Pd/Au NPs (40% ML)/C	Air RT	290	200
	H_2 100 °C	310	210
	H_2 200 °C	220	150
	H_2 300 °C	170	110
	H_2 400 °C	200	140
	He 100 °C	300	210
	He 200 °C	230	160
	He 300 °C	170	120
	He 400 °C	220	150
Pd/Au NPs (60% ML)/C	Air RT	1200	830
	H_2 100 °C	1200	820
	H_2 200 °C	360	250
	H_2 300 °C	150	100
	H_2 400 °C	200	140
	He 100 °C	1200	850
	He 200 °C	370	250
	He 300 °C	150	100
	He 400 °C	190	130
Pd/Au NPs (80% ML)/C	Air RT	1200	820
	H_2 100 °C	1200	840

	H_2 200 °C	280	190
	H_2 300 °C	150	100
	H_2 400 °C	210	140
	He 100 °C	1300	860
	He 200 °C	300	200
	He 300 °C	140	98
	He 400 °C	200	140
Pd/Au NPs (100% ML)/C	Air RT	760	520
	H_2 100 °C	750	510
	H_2 200 °C	210	140
	H_2 300 °C	170	120
	H_2 400 °C	210	140
	He 100 °C	760	520
	He 200 °C	220	150
	He 300 °C	160	110
	He 400 °C	200	140
Pd/Au NPs (150% ML)/C	Air RT	950	660
	H_2 100 °C	890	610
	H_2 200 °C	270	190
	H_2 300 °C	170	120
	H_2 400 °C	190	130
	He 100 °C	870	600
	He 200 °C	280	190
	He 300 °C	170	120
	He 400 °C	200	140
Pd NPs/C	Air RT	32	22
	H_2 100 °C	30	20
	H_2 200 °C	38	26
	H_2 300 °C	150	110
	H_2 400 °C	200	140
	He 100 °C	27	18
	He 200 °C	31	21
	He 300 °C	160	110
	He 400 °C	200	140

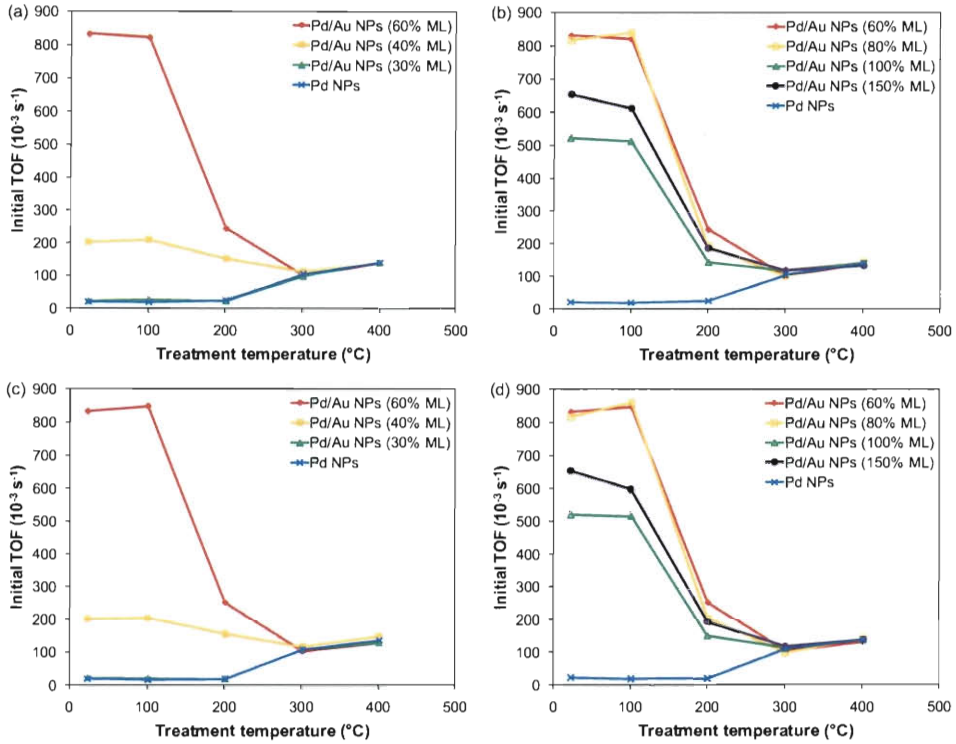

Figure 4.6. TCE HDC reaction activity profiles of catalyst samples with different treatments: (a) in H_2, Pd/Au ≤60% ML, (b) in H_2, Pd/Au ≥60% ML, (c) in He, Pd/Au ≤60% ML, and (d) in He, Pd/Au ≥60% ML.

4.3.5. Relationship between structure and catalytic activity

Structure of Pd/Au NPs was controlled by heat treatments with different temperatures and gases, and treated samples were tested with TCE HDC to show changes of catalytic activity. As shown in Fig. 4.6, treatment in H_2 or He did not have significant difference of activity between each other. XAS results confirmed that nanostructure information (*N* and *R*) of Pd/Au NPs treated at a certain temperature was the same in H_2 or He, except for 150% ML which had multilayers of Pd atoms, leading to Pd-H in H_2 but not in He. However, such Pd-H would always exist in the H_2-saturated reaction condition. Thus, the same nanostructures of Pd/Au NPs treated in H_2 or He could explain the same activity profiles.

As-prepared Pd/Au NPs exhibited activity dependence on Pd coverage, which was discovered by our group [1]. Pd/Au NPs with an incomplete shell of Pd atoms (60-80% ML) were the most active compositions; Pd coverage below or above 60-80% ML led to smaller reaction rates (Fig. 4.6). We have proposed that such dependence was mainly due to the geometric effect, indicating that Pd islands (or ensembles) on the Au NP surface were the active sites. By comparing results from XAS and TCE HDC testing with heat-treated samples, relationships between structure and catalytic activity could be confirmed and support this geometric effect.

As shown in Fig. 4.4, both $N\%_{Au\text{-}Au}$ and $N\%_{Pd\text{-}Pd}$ of Pd/Au NPs with different coverages decreased with treatment temperatures. The downtrend of $N\%_{Au\text{-}Au}$ values indicated that the structure of Pd/Au NPs changed from core-shell (Au-rich core, Pd-rich shell) to bulk PdAu alloy; The downtrend of $N\%_{Pd\text{-}Pd}$ values indicated that Pd islands became mixed with Au to form local PdAu alloy. Table 4.6 concludes that as-prepared Pd/Au NPs of all coverages had gradual structure evolution with treatment temperatures: from a core-shell (Au-rich core, Pd-rich shell) structure with Pd islands on the shell, to surface PdAu alloy, and finally to full bulk PdAu alloy. On the other hand, Fig. 4.6 shows that reaction activities of Pd/Au NPs also decreased with treatment temperatures. Results suggested that activities were generally proportional to $N\%_{Au\text{-}Au}$ and $N\%_{Pd\text{-}Pd}$; that is, a core-shell (Au-rich core, Pd-rich shell) structure with Pd islands on the shell was important for the activity enhancement. As the structure was becoming more like alloy, samples of different Pd coverages went toward the same activity, indicating that the atomic structure arrangement was critical to the activity and alloy would erase such special structure properties. Furthermore, the $N\%_{Pd\text{-}Pd}$ profiles (Fig. 4.4e-h) were more

similar to the activity profiles (Fig. 4.6), as the data points at room temperature and 100 °C were very close and those data points above 200 °C dropped significantly. Such similarity was not found for the $N\%_{Au\text{-}Au}$ profiles (Fig. 4.4a-d), as the data points dropped with increasing temperatures, even at 100 °C. These results suggested that the activity was more related to Pd islands which might serve as major active sites.

Therefore, the significant drop of activity above 200 °C (Fig. 4.6) could be correlated to transition of Pd islands to PdAu alloy; the similar values of activity above 300 °C could be correlated to formation of PdAu alloy (surface or bulk alloy). Although higher Pd coverages could keep Pd islands from forming alloy (Table 4.6), Pd islands indeed started to mix with Au above 200 °C, leading to lower $N\%_{Pd\text{-}Pd}$ (Fig. 4.4e-h) and activity (Fig. 4.6) for different Pd coverages. Above 300 °C, the results suggested that critical Pd islands on the Au NP surface, as major active sites, disappeared and mixed with Au toward surface and bulk PdAu alloy; the activities of all Pd/Au NP samples became very similar to Pd NPs, also indicating that Pd islands on the Au NP surface and the geometric effect were the major factor for the enhanced activity. Pd/Au NPs with 30% ML, unlike higher coverages, did not show better activity for the reaction (Fig. 4.6). Such result was reasonable if we consider that 30% ML might not have enough Pd atoms to form critical Pd islands as Fig. 4.4e shows all $N\%_{Pd\text{-}Pd}$ values were close to x_{Pd}.

It is true that organic compounds (probably from tannic acid and citrate, as reducing agents and surface stabilizers) on the NP surface might affect the activity. From the TGA results (Fig. 4.2), these compounds started decomposing above 200 °C. The activity profile of Pd NPs (Fig. 4.6) served as a comparison standard for such surface ligand effect. Above 200 °C, the reaction rates of Pd NPs started to increase due to

decomposition of surface organic compounds and reduction of Pd atoms. Therefore, the reaction rates of Pd/Au NPs might be also underestimated at lower treatment temperatures. Nevertheless, the activity downtrend of Pd/Au NPs with increasing treatment temperatures still held and was consistent with the structure-activity analysis. Such surface ligand effect also suggested that critical Pd islands of Pd/Au NPs were all eliminated at 300 °C and the slight increase of activity at 400 °C probably resulted from decomposition of more surface ligands.

Based on the above analysis, Pd islands on the Au NP surface have been demonstrated as major active sites for the water-phase TCE HDC reaction. Pd islands (atomic ensembles) on the Au surface have also been investigated to show adsorption and activation of TCE [34, 35] and H_2 [35-37] molecules, further supporting our findings. In addition, hydrogen chemisorption and infrared spectroscopy with CO as the probe molecule [38, 39] can provide information about configuration and quantification of Pd islands on the Au NP surface, which can support the XAS results and the structure-activity analysis; these studies are currently underway.

4.4. Conclusions

The relationship between structure and catalytic activity of bimetallic Pd/Au NPs were investigated. Structure evolution of Pd/Au NPs with different Pd coverages was achieved by heat treatments and characterized with XAS and other techniques while catalytic activity was evaluated with the water-phase TCE HDC reaction at room temperature. As-prepared Pd/Au NPs possessed a core-shell (Au-rich core, Pd-rich shell) structure with Pd islands (atomic ensembles) on the shell; such Pd islands would start to mix with Au to

form surface PdAu alloy and then full bulk PdAu alloy above 200 °C. Pd islands on the Au NP surface were demonstrated to be major active sites for TCE HDC as the reaction rates exhibited an intimate proportional relation to $N\%_{Pd\text{-}Pd}$, which was an indication of the existence of Pd islands. Both reaction rates and $N\%_{Pd\text{-}Pd}$ started to decrease significantly above 200-°C treatment. Reaction rates of Pd/Au NPs with different Pd coverages or Pd NPs became similar values after heated above 300 °C, also indicating that major active sites were composed of Pd islands on the Au NP surface which were almost dislocated above 300 °C. The results and analysis supported that the geometric effect, Pd islands on the Au NP surface as active sites, was dominant for the Pd/Au NPs in the TCE HDC system. In addition, Au NPs showed an ability to stabilize surface Pd atoms in the metallic form, resulting in another benefit for bimetallic PdAu catalysts.

4.5. References

[1] M.O. Nutt, K.N. Heck, P. Alvarez, M.S. Wong, Appl. Catal. B-Environ. 69 (2006) 115-125.

[2] Y.-L. Fang, J.T. Miller, N. Guo, K.N. Heck, P.J.J. Alvarez, M.S. Wong, Catal. Today 160 (2011) 96-102.

[3] Y.-L. Fang, K.N. Heck, P.J.J. Alvarez, M.S. Wong, ACS Catalysis 1 (2011) 128-138.

[4] D. Roth, P. Gelin, A. Kaddouri, E. Garbowski, M. Primet, E. Tena, Catal. Today 112 (2006) 134-138.

[5] P. Castellazzi, G. Groppi, P. Forzatti, A. Baylet, P. Marecot, D. Duprez, Catal. Today 155 (2010) 18-26.

[6] T. Ressler, J. Synchrot. Radiat. 5 (1998) 118-122.

[7] F.W. Lytle, D.E. Sayers, E.A. Stern, Physica B 158 (1989) 701-722.

[8] G.H. Via, K.F. Drake, G. Meitzner, F.W. Lytle, J.H. Sinfelt, Catal. Lett. 5 (1990) 25-33.

[9] K.N. Heck, M.O. Nutt, P.J.J. Alvarez, M.S. Wong, J. Catal. 267 (2009) 97-104.

[10] R.P. Schwarzenbach, P.M. Gschwend, D.M. Imboden, Environmental Organic Chemistry. Wiley, Hoboken, NJ, 1993.

[11] J.T. Miller, A.J. Kropf, Y. Zha, J.R. Regalbuto, L. Delannoy, C. Louis, E. Bus, J.A. van Bokhoven, J. Catal. 240 (2006) 222-234.

[12] J.T. Miller, M.K. Neylon, C.L. Marshall, A.J. Kropf, in: C.I. Contescu, K. Putyera, (Eds.), Dekker Encyclopedia of Nanoscience and Nanotechnology, CRC Press, Boca Raton, FL, 2004, 3953-3972.

[13] G. Vlaic, D. Andreatta, P.E. Colavita, Catal. Today 41 (1998) 261-275.

[14] G. Meitzner, Catal. Today 39 (1998) 281-291.

[15] J.H. Sinfelt, Accounts Chem. Res. 20 (1987) 134-139.

[16] N. Toshima, M. Harada, Y. Yamazaki, K. Asakura, J. Phys. Chem. 96 (1992) 9927-9933.

[17] J.S. Bradley, G.H. Via, L. Bonneviot, E.W. Hill, Chem. Mat. 8 (1996) 1895-1903.

[18] A. Frenkel, Z. Kristall. 222 (2007) 605-611.

[19] W.C. Ketchie, M. Murayama, R.J. Davis, J. Catal. 250 (2007) 264-273.

[20] C.H. Chen, L.S. Sarma, J.M. Chen, S.C. Shih, G.R. Wang, D.G. Liu, M.T. Tang, J.F. Lee, B.J. Hwang, ACS Nano 1 (2007) 114-125.

[21] P. Dash, T. Bond, C. Fowler, W. Hou, N. Coombs, R.W.J. Scott, J. Phys. Chem. C 113 (2009) 12719-12730.

[22] M.G. Weir, M.R. Knecht, A.I. Frenkel, R.M. Crooks, Langmuir 26 (2010) 1137-1146.

[23] S.M. Oxford, P.L. Lee, P.J. Chupas, K.W. Chapman, M.C. Kung, H.H. Kung, J. Phys. Chem. C 114 (2010) 17085-17091.

[24] R.J. Davis, M. Boudart, J. Phys. Chem. 98 (1994) 5471-5477.

[25] S.N. Reifsnyder, H.H. Lamb, J. Phys. Chem. B 103 (1999) 321-329.

[26] M.R. Knecht, M.G. Weir, A.I. Frenkel, R.M. Crooks, Chem. Mat. 20 (2008) 1019-1028.

[27] M.W. Tew, J.T. Miller, J.A. van Bokhoven, J. Phys. Chem. C 113 (2009) 15140-15147.

[28] G.V. Lowry, M. Reinhard, Environ. Sci. Technol. 33 (1999) 1905-1910.

[29] M.O. Nutt, J.B. Hughes, M.S. Wong, Environ. Sci. Technol. 39 (2005) 1346-1353.

[30] K. Mackenzie, H. Frenzel, F.D. Kopinke, Appl. Catal. B-Environ. 63 (2006) 161-167.

[31] J.C. Liu, F. He, E. Durham, D.Y. Zhao, C.B. Roberts, Langmuir 24 (2008) 328-336.

[32] G.V. Lowry, M. Reinhard, Environ. Sci. Technol. 34 (2000) 3217-3223.

[33] S. Ordonez, B.P. Vivas, F.V. Diez, Appl. Catal. B-Environ. 95 (2010) 288-296.

[34] K.T. Park, K. Klier, C.B. Wang, W.X. Zhang, J. Phys. Chem. B 101 (1997) 5420-5428.

[35] J. Andersin, K. Honkala, Phys. Chem. Chem. Phys. 13 (2011) 1386-1394.

[36] F. Maroun, F. Ozanam, O.M. Magnussen, R.J. Behm, Science 293 (2001) 1811-1814.

[37] R.J. Behm, Z. Phys. Chemie-Int. J. Res. Phys. Chem. Chem. Phys. 223 (2009) 9-36.

[38] H.G. Lang, S. Maldonado, K.J. Stevenson, B.D. Chandler, J. Am. Chem. Soc. 126 (2004) 12949-12956.

[39] J. Rebelli, M. Detwiler, S. Ma, C.T. Williams, J.R. Monnier, J. Catal. 270 (2010) 224-233.

Chapter 5

Doping Supported Palladium Catalysts with Gold for Activity Enhancement

5.1. Introduction

For palladium-gold (PdAu) catalysts, there is a gap between fundamental researches and practical applications. It is true that scientists have the ability to synthesize colloidal PdAu nanoparticle (NP) catalysts with desired and uniform nanostructures by delicate chemistry—usually with reducing agents and stabilizers like ligands [1, 2], polymers [3-5], or dendrimers [6, 7]. For possible real applications, people have also tried to immobilize these NPs directly on a solid support [8-10], or entrap them into a support matrix by sol-gel chemistry [11-13]. However, such colloidal synthesis may be only practical on a laboratory basis because of scale-up difficulties, additional removal of surface stabilizers and solvents, as well as resulting higher costs. To avoid these problems, researchers have investigated direct synthesis of PdAu NPs on a support. Monnier and coworkers prepared supported Au-shell/Pd-core catalysts by the electroless deposition (ED) method which can obtain core-shell bimetallic nanostructures at room temperature without stabilizers, but a special setup of ED bath (including choice of metal salts, reducing agents, and pH values) is necessary [14, 15]. A synthesis route with common processes of industrial catalyst manufacture is more desirable [16, 17]. Hutchings and coworkers have shown that supported PdAu catalysts, with a Pd-shell/Au-core

nanostructure, could be synthesized with common processes such as impregnation, drying, calcination, and reduction [18-21]. They did co-impregnation of Pd and gold salts on titania (TiO_2) or alumina (Al_2O_3), followed by drying and calcination, and then confirmed the core-shell nanostructure by X-ray photoelectron spectroscopy (XPS) and scanning transmission electron microscopy (STEM) with high-angle annular dark field (HAADF) images and X-ray energy dispersive spectroscopy (XEDS) mapping.

In this work, we conducted a systematic study to exhibit that adding Au to pre-synthesized supported Pd catalysts could still improve catalytic activities and alter catalyst nanostructures through different treatments. We did impregnation of gold salt on the carbon-supported Pd catalyst, followed with common industrial processes including drying, calcination, and reduction. Catalysts were characterized with inductively coupled plasma spectrometry (ICP), transmission electron microscopy (TEM), and X-ray absorption spectroscopy (XAS). Catalytic activities were evaluated with the room-temperature, aqueous-phase hydrodechlorination (HDC) of trichloroethene (TCE). We would like to transmit the bimetallic enhancement from colloidal NPs to supported catalysts in this work. Results showed that improved activities and controlled nanostructures could be achieved by adding Au to pre-existed supported Pd catalysts through common industrial processes.

5.2. Experimental

5.2.1. Catalyst preparation and treatments

All types of carbon-supported PdAu catalysts (PdAu/C) were prepared from the commercial Pd-on-carbon (Pd/C, 1 wt% Pd, Alfa Aesar) catalysts, with addition of Au

and different treatments. Scheme 5.1 shows preparation routes of samples. Pd/C powder was pretreated with calcination in flowing air (100 sccm (standard cubic centimeters per minute, cm^3/min), breathing quality, Matheson) at 400 °C for 3 hr and cooling to room temperature in flowing air, followed by reduction in flowing hydrogen gas (100 sccm, 99.99%, Matheson) at 400 °C for 3 hr and cooling to room temperature in flowing hydrogen gas. For each batch, 2 g Pd/C powder was dispersed in a mixture of 4-5 mL Nanopure water (>18.0 MΩ-cm, Barnstead NANOpure Diamond) and 0.2 mL isopropanol (>95%, ACS reagent, Fisher) at room temperature (22 ± 2 °C), followed by ultrasonication for 1 min. Gold salt $HAuCl_4$ solution (0.236 M; $HAuCl_4 \cdot 3H_2O$, 99.9+%, Sigma-Aldrich; dissolved in water at room temperature) was then added into the mixture with stirring. Volume of Nanopure water was adjusted to make 5 mL final solution including Nanopure water, isopropanol, and $HAuCl_4$ solution. Volume of $HAuCl_4$ solution (60-800 μL) was chosen for target Au loadings. The final powder suspension was kept stirring in the dark at room temperature for 6 hr before drying in a 90-°C oven for 16 hr.

Dried catalyst powder was divided into four equal piles; each pile was treated with one of the following procedures: (1) calcination in flowing air at 400 °C for 3 hr and cooling to room temperature in flowing air (Dried/Air), (2) calcination in flowing air at 400 °C for 3 hr and cooling to room temperature in flowing air, then reduction in flowing hydrogen gas at 400 °C for 3 hr and cooling to room temperature in flowing hydrogen gas (Dried/Air/H_2), (3) reduction in flowing hydrogen gas at 400 °C for 3 hr and cooling to room temperature in flowing hydrogen gas (Dried/H_2), and (4) reduction in flowing hydrogen gas at 400 °C for 3 hr and cooling to room temperature in flowing hydrogen

gas, then calcination in flowing air at 400 °C for 3 hr and cooling to room temperature in flowing air (Dried/H_2/Air). Sample codes are listed in Table 5.1. Products were stored in air, in the dark, and at room temperature.

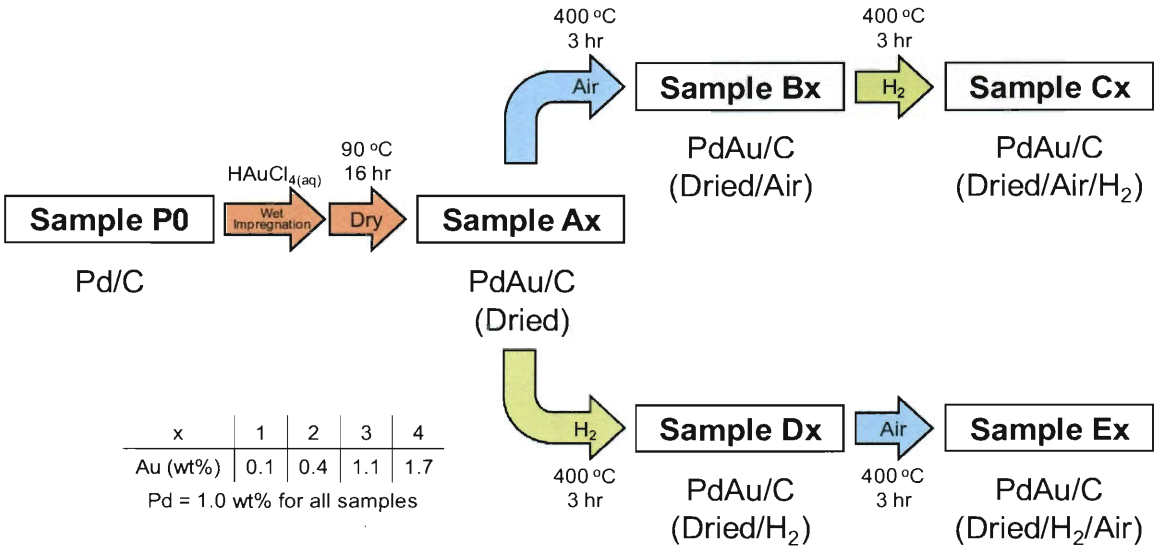

Scheme 5.1. Preparation routes of PdAu/C samples.

5.2.2. Catalyst characterization

5.2.2.1. Inductively coupled plasma spectrometry (ICP)

Elemental analysis of catalysts was conducted with a PerkinElmer inductively coupled plasma optical emission spectrometer (ICP-OES) Optima 4300 DV. Catalyst powder was mixed with aqua regia containing 10 mL $HCl_{(aq)}$ (1 N, Fisher), and 0.3 mL $HNO_{3(aq)}$ (70 wt%, Fisher); then heated at 90 °C for 30 min. After cooling down to room temperature, the solution was treated with a 0.45-μm filter before ICP analysis of Pd and Au loadings.

5.2.2.2. Transmission electron microscopy (TEM)

Particle size and morphology of catalysts were characterized with a JEOL 2100 transmission electron microscope. Catalyst powder was dispersed in isopropanol with

ultrasonication, then deposited on a 200-mesh carbon/formvar TEM grid, and air-dried at room temperature. TEM was done with help from Dr. H. G. Bagaria.

5.2.2.3. X-ray absorption spectroscopy (XAS)

X-ray absorption measurements were performed on the insertion-device beamline 10-ID-B of the Materials Research Collaborative Access Team (MRCAT) at the Advanced Photon Source at Argonne National Laboratory. The presence of harmonics was minimized with a cryogenically cooled double-crystal Si (111) monochromator in conjunction with an uncoated glass mirror. The monochromator was scanned continuously during the measurements with data points integrated over 0.5 eV for 0.07 sec per data point. Measurements were made in transmission mode with the ionization chambers optimized for the maximum current with linear response (~10^{10} photons detected per sec) using a mixture of nitrogen and helium in the incident X-ray detector and a mixture of ~20% argon in nitrogen in the transmission X-ray detector. Absorption was measured at both Pd and Au edges; a Pd or Au foil spectrum was acquired simultaneously with each measurement for energy calibration.

Samples of catalyst powder were pressed into a cylindrical holder with a thickness chosen to give a total absorbance (μx) at the Pd K (24.350 keV) and Au L_{III} (11.918 keV) edges of ca. 2.0, and an edge step ($\Delta\mu x$) of ca. 0.5. The sample holder was placed in a reactor cell (glass tube, length 18 in., diameter 0.75 in.) fitted at both ends with polyimide windows and stainless steel valves to isolate the reactor from the atmosphere. The reactor was purged with flowing hydrogen gas for 10 min and then sealed, in order to mimic the hydrogen atmosphere during HDC reactions. All spectra were measured at room temperature.

Experimental phase shifts and back-scattering amplitudes were obtained from reference compounds: Pd foil for Pd-Pd bonding, $Pd(NH_3)_4(NO_3)_2$ (Aldrich) for Pd-O bonding, and Au foil for Au-Au bonding. Experimental data of Pd and Au foil were used to determine the best fit of Debye-Waller factors (DWF) and amplitude reduction factors (S_o) for phase shifts and back-scattering amplitudes in the FEFF fitting [22]. Along with the bond distances for Pd and Au foil, these values were used for determining the Pd-Au and Au-Pd FEFF phase shifts and back-scattering amplitudes. Standard procedures based on the WINXAS97 software [22] were used to extract the data [23]. The coordination parameters were obtained by a least-square fit in *k*- and *R*-space of the nearest-neighbor, k^2-weighted Fourier transform (FT) data (*k*: photoelectron wave number, *R*: bond distance). The data fitted equally well with both k^1 and k^3 weightings.

5.2.3. Catalyst testing

Aqueous-phase hydrodechlorination (HDC) of trichloroethene (TCE) at room temperature was chosen as the model reaction for catalytic testing. Batch reaction was performed similar to the previous studies [24-26]. A screw-cap bottle (250 mL, Alltech), containing 165 mL Nanopure water, 3 mL $NaHCO_{3(aq)}$ buffer (0.08 M; $NaHCO_3$, 99%, Fisher), and a magnetic stir bar, were sealed with PTFE-sealed threads and a PTFE-silicone septum. Hydrogen gas was bubbled into the bottle for 15 min to displace dissolved oxygen and to fill the headspace with a hydrogen atmosphere (1 atm). Then, 7 μL TCE (99.5%, Sigma-Aldrich) and 0.2 μL pentane (99.7%, Burdick and Jackson), as the internal standard, were injected into the sealed bottle. The overall solution was stirred for at least 3 hr to reach equilibrium. In a separate vial, ~50 mg catalyst powder was dispersed in a mixture of 4.5 mL Nanopure water and 0.5 mL isopropanol with

ultrasonication for 1 min. At time t = 0, catalyst suspension was injected into the bottle with the stir rate at 600 rpm. The initial TCE concentration in liquid phase was 50.9 ppm, far below the saturation concentration of 1200 ppm in water at 25 °C [27]. The reaction was monitored through headspace gas chromatography (GC) using an Agilent Technologies 6890N GC with a flame ionization detector (FID) and a 60/80 Carbopack B/1% SP-1000 packed column (Supelco 12487, Sigma-Aldrich). Samples were taken from the headspace (gas phase) of the reactor, and then injected into GC to determine quantities of TCE and other compounds (>90% selectivity to ethane [24]). Reaction rates were determined from changes of TCE concentrations in the headspace. All reactions were performed at room temperature.

5.3. Results and discussion

5.3.1. Elemental analysis and particle morphology

ICP results of Pd and Au loadings are listed in Table 5.1. Pd loadings remained the same (~1 wt%) for all the samples, compared to the control Sample P0 (1 wt% Pd/C with only pretreatments). Au loadings were 0.1 wt%, 0.4 wt%, 1.1 wt%, and 1.7 wt% for Sample Group 1, 2, 3, and 4, respectively.

Fig. 5.1 shows representative TEM images of PdAu/C samples, indicating that metal particles have roughly spherical morphology and a broad size distribution from ~5 nm (Fig. 5.1a) to over 50 nm (Fig. 5.1b). Thus, it is difficult to obtain an accurate size profile of PdAu/C samples by analyzing TEM images because larger particles would block the visibility of smaller particles. Chemisorption with H_2 or CO might reveal more details about accessible Pd active sites on the catalyst surface; this work is currently

underway. Current TEM images implied a bimodal size distribution for metal particles on PdAu/C samples, with smaller particles around 5-10 nm (Fig. 5.1a) and larger particles around 30-100 nm (Fig. 5.1b). More images will be taken to support this point. If this hypothesis is true, such bimodal distribution is consistent with co-impregnated PdAu catalysts by Hutchings and co-workers [21].

Table 5.1. Catalyst compositions, treatments, and reaction rates (metal weight loading determined by ICP, rate constant k_{cat} and initial turnover frequency (TOF) determined from aqueous-phase TCE HDC with initial $[TCE]_{(aq)}$ = 50.9 ppm at room temperature 22 ± 2 °C).

#	Catalyst	Pd weight loading (wt%)	Au weight loading (wt%)	Treatment	Rate constant k_{cat} ($L/g_{Pd}/min$)	Initial TOF (10^{-3} $mol_{TCE}/mol_{Pd}/s$)
A1	PdAu/C	1.0	0.1	Dried	29	20
A2	PdAu/C	1.0	0.4	Dried	85	58
A3	PdAu/C	1.0	1.1	Dried	89	61
A4	PdAu/C	1.0	1.7	Dried	33	22
B1	PdAu/C	1.0	0.1	Dried/Air	39	27
B2	PdAu/C	1.0	0.4	Dried/Air	130	88
B3	PdAu/C	1.0	1.1	Dried/Air	110	75
B4	PdAu/C	1.0	1.7	Dried/Air	22	15
C1	PdAu/C	1.0	0.1	Dried/Air/H_2	84	58
C2	PdAu/C	1.0	0.4	Dried/Air/H_2	310	210
C3	PdAu/C	1.0	1.1	Dried/Air/H_2	490	340
C4	PdAu/C	1.0	1.7	Dried/Air/H_2	310	210
D1	PdAu/C	1.0	0.1	Dried/H_2	64	44
D2	PdAu/C	1.0	0.4	Dried/H_2	71	49
D3	PdAu/C	1.0	1.1	Dried/H_2	59	41
D4	PdAu/C	1.0	1.7	Dried/H_2	63	43
E1	PdAu/C	1.0	0.1	Dried/H_2/Air	46	32
E2	PdAu/C	1.0	0.4	Dried/H_2/Air	71	49
E3	PdAu/C	1.0	1.1	Dried/H_2/Air	120	82
E4	PdAu/C	1.0	1.7	Dried/H_2/Air	210	140
P0	Pd/C	1.0	0	(pretreatments only, control sample)	32	22

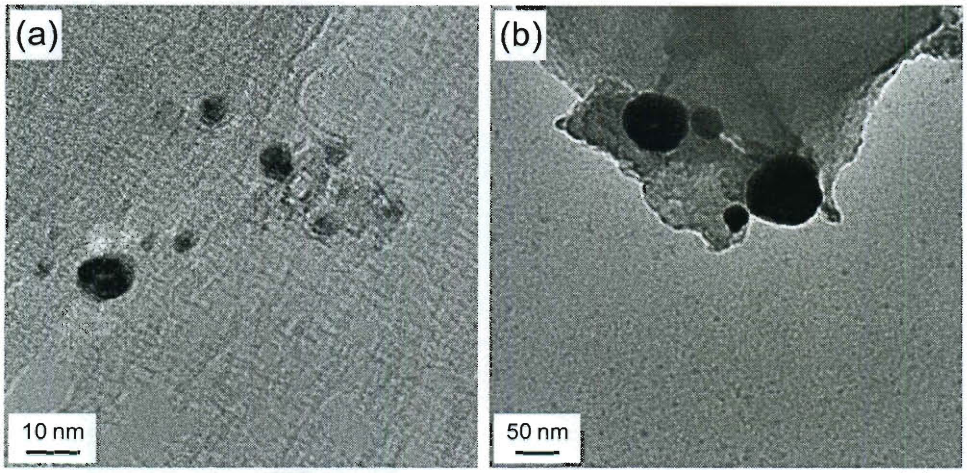

Figure 5.1. Representative TEM images of Sample C3 with (a) smaller particles around 5-10 nm and (b) larger particles around 30-100 nm. (Courtesy of Dr. H. G. Bagaria)

5.3.2. Catalytic activity for TCE HDC reaction

Reaction rates of TCE HDC were determined as rate constant k_{cat} and initial turnover frequency (TOF, number of reacted TCE molecules per Pd atom per sec), with the implicit assumption of first-order dependence in TCE and zero-order in H_2 [24, 28-30]. Both expressions are used in related research articles [24, 28-31]; therefore, we report both for easier comparison with other works. k_{cat} is the Pd-normalized reaction rate constant (with unit of $L/g_{Pd}/min$), derived from Eqs. 1-2:

$$\text{reaction rate} = \frac{-\mathrm{d}C_{TCE}}{\mathrm{d}t} = k_{meas} C_{TCE} \tag{1}$$

$$k_{meas} = k_{cat} C_{cat} \tag{2}$$

where k_{meas} is the measured first-order rate constant, C_{TCE} and C_{cat} are the concentrations of TCE and Pd in the liquid phase in the reactor, respectively. It is true that the real kinetics is more complicated [32]; nevertheless, rate constants and initial TOF's can be used to compare catalytic activities at a given TCE concentration and at an excess

concentration of H_2 in the system [26, 32]. Dilute $NaHCO_{3(aq)}$ (~1.4 mM in the reactor) was chosen as the buffer, and pH was controlled between 8.3-6.0 for all the tests in order to minimize possible effects from salts and pH [33, 34]. All reactions could reach >90% TCE conversion and show >90% product selectivity to ethane as we reported previously [24].

Results of catalyst activities are listed in Table 5.1; data points of initial TOF's at different compositions and treatments are plotted in Fig. 5.2. Most of the bimetallic PdAu/C samples showed higher activities than Pd/C (Sample P0), indicating that catalytic enhancement could be achieved by addition of Au with simple treatment processes. Sample C3 (initial TOF = 340 × 10^{-3} $mol_{TCE}/mol_{Pd}/s$) was the most active one, with the initial TOF value >15 times higher than Pd/C (initial TOF = 22 × 10^{-3} $mol_{TCE}/mol_{Pd}/s$).

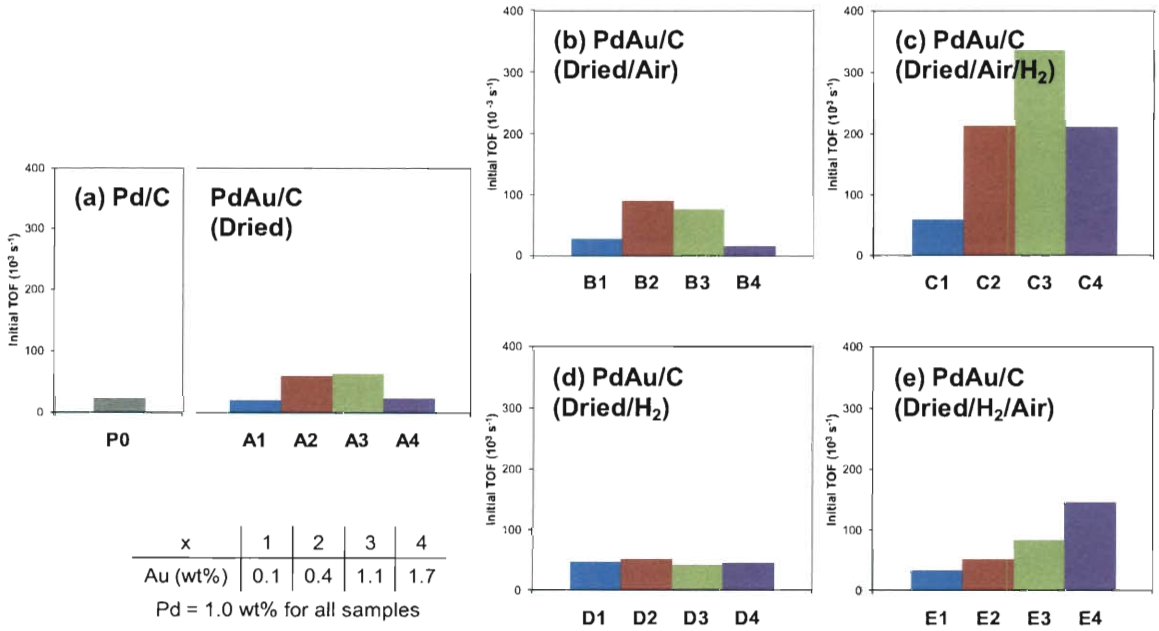

Figure 5.2. TCE HDC reaction activity profiles of PdAu/C catalysts with different Au loadings and treatment processes: (a) PdAu/C (Dried) and Pd/C, (b) PdAu/C (Dried/Air), (c) PdAu/C (Dried/Air/H_2), (d) PdAu/C (Dried/H_2), and (e) PdAu/C (Dried/H_2/Air).

5.3.3. Local atomic information from XAS measurements

XAS is among one of the powerful techniques which have the ability to acquire detailed structural and electronic information at an atomic level for monometallic NPs [35-37] and bimetallic NPs [3, 6, 7, 13, 26, 38-45]. While XAS contains two regions—the x-ray absorption near-edge structure (XANES) and extended x-ray absorption fine structure (EXAFS) regions, we are more interested in the EXAFS region which provides local structural information including neighboring atom (in terms of scattering path), coordination number (*N*), and bond distance (*R*). Table 5.2 shows results of EXAFS fitting.

Table 5.2. EXAFS fit parameters (*N*: coordination number, *R*: bond distance, RT: room temperature).

#	Catalyst	Edge	Treatment for XAS	Scattering path	*N* (±10%)	*R* (Å) (±0.02 Å)
A1	PdAu/C	Pd	H_2 RT	Pd-Pd	9.7	2.75
		Au	H_2 RT	Au-Au	10.8	2.87
A2	PdAu/C	Pd	H_2 RT	Pd-Pd	10.0	2.74
		Au	H_2 RT	Au-Au	10.3	2.84
A3	PdAu/C	Pd	H_2 RT	Pd-Pd	11.1	2.75
		Au	H_2 RT	Au-Au	10.1	2.87
				Au-Pd	2.0	2.79
A4	PdAu/C	Pd	H_2 RT	Pd-Pd	9.8	2.79
		Au	H_2 RT	Au-Au	9.4	2.83
A5	PdAu/C	Pd	H_2 RT	Pd-Pd	10.2	2.75
		Au	H_2 RT	Au-Au	9.4	2.84
B1	PdAu/C	Pd	H_2 RT	Pd-Pd	9.2	2.75
		Au	H_2 RT	Au-Au	11.0	2.86
B2	PdAu/C	Pd	H_2 RT	Pd-Pd	6.1	2.75
				Pd-Au	5.3	2.79
		Au	H_2 RT	Au-Au	9.1	2.86
				Au-Pd	2.6	2.80
B3	PdAu/C	Pd	H_2 RT	Pd-Pd	6.4	2.75
				Pd-Au	5.5	2.80
		Au	H_2 RT	Au-Au	9.7	2.84

				Au-Pd	2.2	2.79
B4	PdAu/C	Pd	H_2 RT	Pd-Pd	6.6	2.76
				Pd-Au	5.2	2.79
		Au	H_2 RT	Au-Au	10.9	2.85
B5	PdAu/C	Pd	H_2 RT	Pd-Pd	9.0	2.75
		Au	H_2 RT	Au-Au	10.8	2.86
C1	PdAu/C	Pd	H_2 RT	Pd-Cl	3.8	2.33
		Au	H_2 RT	Au-Au	10.7	2.86
C2	PdAu/C	Pd	H_2 RT	Pd-Pd	3.5	2.75
				Pd-Au	7.0	2.79
		Au	H_2 RT	Au-Au	10.3	2.83
C3	PdAu/C	Pd	H_2 RT	Pd-Pd	4.8	2.75
				Pd-Au	6.4	2.79
		Au	H_2 RT	Au-Au	10.3	2.86
				Au-Pd	1.7	2.79
C4	PdAu/C	Pd	H_2 RT	Pd-Pd	4.4	2.75
				Pd-Au	7.0	2.79
		Au	H_2 RT	Au-Au	11.0	2.86
C5	PdAu/C	Pd	H_2 RT	Pd-Pd	4.4	2.75
				Pd-Au	7.0	2.79
		Au	H_2 RT	Au-Au	10.9	2.84
D1	PdAu/C	Pd	H_2 RT	Pd-Cl	4.0	2.33
		Au	H_2 RT	Au-Au	9.5	2.86
				Au-Cl	0.8	2.29
D2	PdAu/C	Pd	H_2 RT	Pd-Pd	2.1	2.75
				Pd-Au	5.7	2.80
				Pd-O	1.3	2.04
		Au	H_2 RT	Au-Au	11.1	2.86
D3	PdAu/C	Pd	H_2 RT	Pd-Pd	4.5	2.75
				Pd-Au	6.5	2.79
		Au	H_2 RT	Au-Au	11.0	2.86
D4	PdAu/C	Pd	H_2 RT	Pd-Pd	4.3	2.74
				Pd-Au	7.5	2.79
		Au	H_2 RT	Au-Au	11.0	2.86
D5	PdAu/C	Pd	H_2 RT	Pd-Pd	2.9	2.75
				Pd-Au	5.4	2.80
				Pd-O	0.9	2.04
		Au	H_2 RT	Au-Au	10.9	2.85
P0	Pd/C	Pd	H_2 RT	Pd-Pd	10.5	2.80

5.3.4. Effect of Au loading on catalytic activity

From the Pd edge, coordination numbers of bimetallic Pd-Au bonding ($N_{Pd\text{-}Au}$) increased with higher Au loadings as a general trend (Table 5.2). $N_{Pd\text{-}Au}$ could go up to 7.0-7.5 which was 60-70% of total coordination number of Pd (N_{Pd}). FT results from the EXAFS data also indicated this dependence between bimetallic interaction and Au loadings, by comparison among samples with different Au loadings under the same Dried/Air/H_2 treatments (Fig. 5.3). Sample C1 (Au 0.1 wt%) exhibited FT results almost the same as Pd foil (Fig. 5.3a), implying no or very little Pd-Au interaction. Sample C2 (Au 0.4 wt%) exhibited change in the ratio of the two characteristic Pd peaks (the two highest FT magnitude peaks) and small shifts in the node positions (y-axis = 0 intercept) of the FT imaginary parts (Fig. 5.3b); both are due to interference from the Pd-Pd and Pd-Au contributions, indicating bimetallic Pd-Au bonding. Sample C3 (Au 1.1 wt%) and C4 (Au 1.7 wt%) both showed nearly equal ratios of the two characteristic Pd peaks (Fig. 5.3c, d), indicating more Pd-Au interaction.

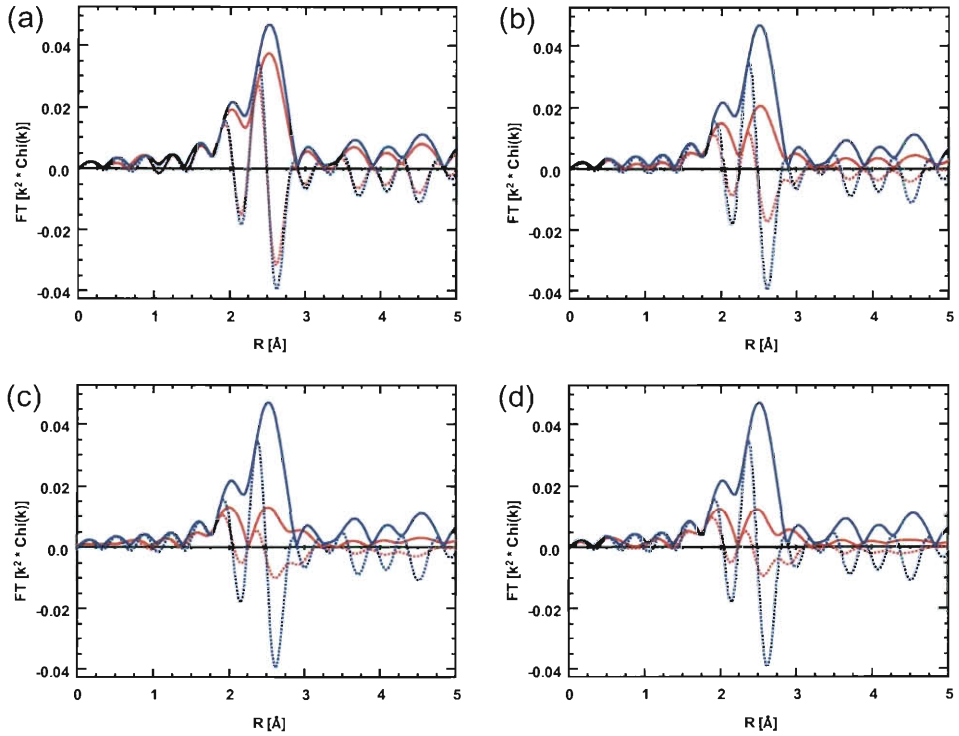

Figure 5.3. Fourier transform (k^2 weighted, Δk = 2.7-11.8 Å^{-1}; solid line: magnitude, dotted line: imaginary components) of Pd K edge EXAFS data for Pd foil (blue) and PdAu/C samples (red): (a) Sample C1, (b) Sample C2, (c) Sample C3, and (d) Sample C4.

However, from the Au edge, Au-Pd interaction could not be obtained for most PdAu/C samples (Table 5.2), except for Sample C1, B2, C2, and C3 with small $N_{\text{Au-Pd}}$ values ($N_{\text{Au-Pd}}$ = 1.7-2.6, 14-22% of total coordination number of Au). That is, the major part of Au atoms was in the monometallic Au-Au structure, not in the bimetallic structure; however, a significant part of Pd atoms was in the bimetallic structure with increasing Au loadings. As an example, Fig. 5.4 shows FT results from the EXAFS data of samples with different Au loadings under the same Dried/Air/H_2 treatments. Compared to Au foil, samples with lower Au loadings (C1, C2, and C3) exhibited noticeable difference in shapes and relative intensities of the magnitude peaks, and in node positions of the imaginary parts (Fig. 5.4a, b, c), as affected from Au-Pd interaction. On the other hand,

Sample C4 with a higher Au loading exhibited only little difference from Au foil (Fig. 5.4d), showing no significant Au-Pd interaction. The small shift in the imaginary part of C4 was due to $R_{Au\text{-}Au}$ change between C4 (2.86 Å) and Au foil (2.88 Å), indicating C4 was very much like Au foil but with a smaller size. With increasing Au loadings, most Au atoms formed monometallic Au particles; therefore, diluted the Au-Pd interaction which happened only in a small part of Au atoms. Indeed, the Dried/Air/H_2 process could enhance the bimetallic Au-Pd interaction (see Sec. 5.3.5) while other processes led to no or little Au-Pd interaction even at low Au loadings. The above explanation implies that most Pd-Au interaction was in smaller particles, and almost only Au presented in larger particles, in accordance with the observed bimodal size distribution from TEM. This interpretation is consistent with the work by Hutchings and co-workers [21]. They synthesized supported PdAu catalysts by co-impregnation, also resulting in bimodal size distribution; they further confirmed the structure with PdAu alloys in smaller particles and Au in larger particles by STEM-XEDS.

One significant remark, as observed in Table 5.2, is that Au could stabilize metallic Pd under high-temperature calcination. Based on our experience, Pd/C could be fully oxidized after calcination in flowing air at 400 °C; could not be reduced in H_2 at room temperature and showed no activity for TCE HDC. However, addition of Au, as low as 0.1 wt%, could improve Pd oxidization resistance notably. Sample B1, E1 (Au 0.1 wt%), B2, E2 (Au 0.4 wt%), and B3, E3 (Au 1.1 wt%) all exhibited no detectable oxidized Pd, and also showed catalytic activities (Table 5.1, 5.2). This stabilization effect was also found in our previous investigation for colloidal Pd/Au NPs [26]. On the other hand, Sample B4 and E4 (Au 1.7 wt%) still showed partial Pd oxidation (~33% for B4,

~23% for E4; percentages calculated from the ratio between $N_{Pd\text{-}O}$ of the sample and $N_{Pd\text{-}O}$ (= 4) of fully oxidized PdO), and this might be due to excess Cl^- ions from the gold salt. It is known that Cl^- ions can be oxidatively adsorbed to Pd under acidic conditions and therefore reduce Pd activity [25, 46]. We previously reported that such Cl binding affinity and Pd deactivation could be lowered in the presence of Au [24, 25]. However, Sample Group D might have too many Cl^- ions (0.73 mmol Cl atoms for 2 g PdAu/C, atomic ratio Cl:Pd = 3.9:1) so that major Pd-Cl bonding could still form and then reduce Pd-Au contact as well as Pd oxidization resistance.

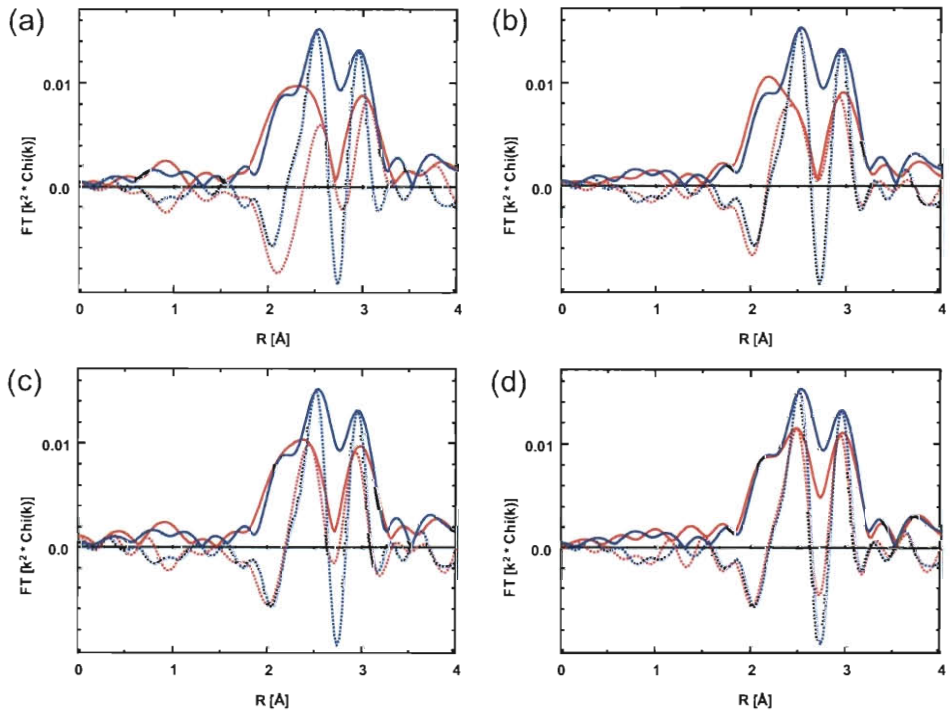

Figure 5.4. Fourier transform (k^2 weighted; solid line: magnitude, dotted line: imaginary components) of Au L_{III} edge EXAFS data for Au foil (blue) and PdAu/C samples (red): (a) Sample C1 (Δk = 2.7-11.8 $Å^{-1}$), (b) Sample C2 (Δk = 2.6-11.7 $Å^{-1}$), (c) Sample C3 (Δk = 2.6-11.5 $Å^{-1}$), and (d) Sample C4 (Δk = 2.6-12.0 $Å^{-1}$).

Total coordination numbers can be used to estimate average sizes of NPs [47]. The control sample Pd/C (Sample P0) with $N_{Pd} = N_{Pd\text{-}Pd} = 10.5$ was estimated as 6.5 nm, slightly larger than the 4-5 nm diameter observed from TEM, which might be attributed to EXAFS being more sensitive to larger particles. For PdAu/C samples, this estimation was not suitable due to the bimodal size distribution.

The Au-Au bond distances of all PdAu/C samples were similar (2.83-2.87 Å) and slightly less than Au foil (2.88 Å), which is typical for NPs. The Pd-Pd bond distance of Pd/C (2.80 Å) was larger than Pd foil (2.75 Å) and similar to Pd-H [48], which was reasonable since XAS measurements were conducted in a hydrogen atmosphere. Such hydride behavior disappeared with the addition of Au. PdAu/C samples ($N_{Pd\text{-}Pd}$ = 2.74-2.76 Å) became similar to Pd foil except that Sample D1 ($N_{Pd\text{-}Pd}$ = 2.79 Å) was still more like Pd-H due to its low Au loading and no bimetallic interaction.

Fig. 5.5 provides proposed catalyst structures, summarizing the general effect of Au loadings; Fig. 5.6 shows profiles of reaction activities and bimetallic interaction (Pd-Au and Au-Pd) at different Au loadings under the same treatment process (Dried/Air/H_2, as an example). Higher Au loadings led to more Pd-Au interaction (higher $N_{Pd\text{-}Au}$) but less Au-Pd interaction (lower $N_{Au\text{-}Pd}$). Sample C3 (Au 1.1 wt%, $N_{Pd\text{-}Au}$ = 6.4, $N_{Au\text{-}Pd}$ = 1.7) was the most active one (initial TOF = 340×10^{-3} $mol_{TCE}/mol_{Pd}/s$). The Dried/Air/H_2 process provided the highest activities than other processes, and exhibited a volcano-shape curve for activities among different Au loadings. While initial TOF's were proportional to Au loadings for samples with Au ≤1.1 wt%, Sample C4 became less active (initial TOF = 210×10^{-3} $mol_{TCE}/mol_{Pd}/s$) with a higher Au loading 1.7 wt%. By comparing Sample C3 and C4 (Table 5.2 and Fig. 5.6), we found that C3 and C4 were similar from the Pd edge

(C3: $N_{Pd\text{-}Pd}$ = 4.8, $N_{Pd\text{-}Au}$ = 6.4; C4: $N_{Pd\text{-}Pd}$ = 4.5, $N_{Pd\text{-}Au}$ = 6.5), but more different from the Au edge (C3: $N_{Au\text{-}Au}$ = 10.3, $N_{Au\text{-}Pd}$ = 1.7; C4: $N_{Au\text{-}Au}$ = 11.0, $N_{Au\text{-}Pd}$ = 0). This suggests that a certain amount of Au could interact with Pd so that C3 and C4 were similar from the Pd edge; on the other hand, excess Au in C4 might form big Au clusters and block nearby Pd sites so that C4 had no $N_{Au\text{-}Pd}$, a larger $N_{Au\text{-}Au}$, and a lower activity.

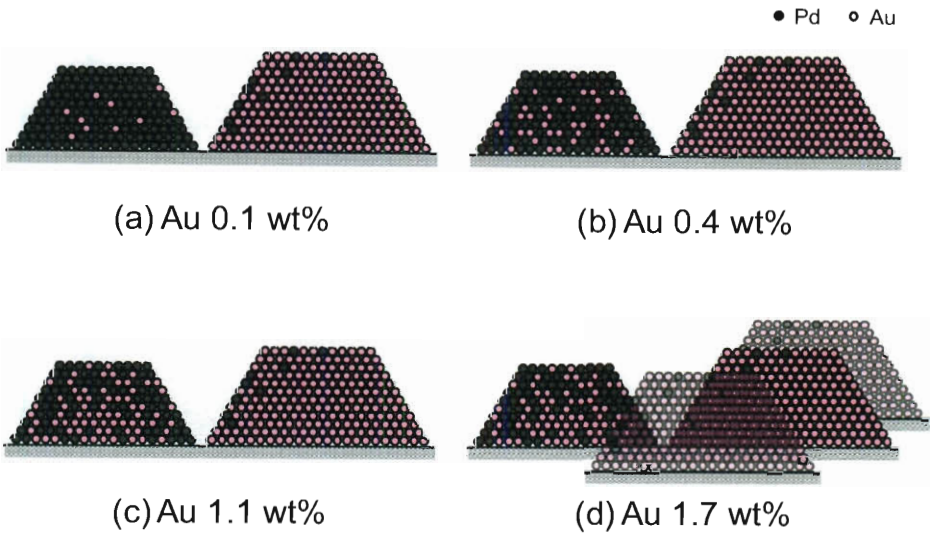

Figure 5.5. Illustration of proposed cross-section structures of PdAu/C samples with different Au loadings: (a) Au 0.1 wt%, (b) Au 0.4 wt%, (c) Au 1.1 wt%, and (d) Au 1.7 wt%.

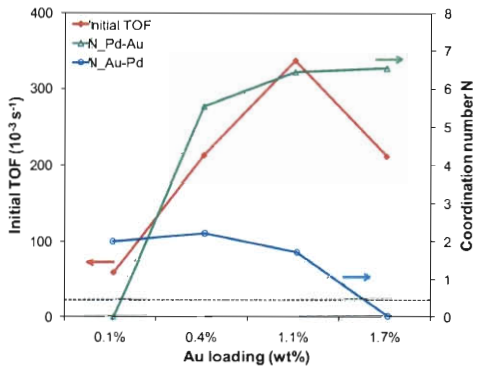

Figure 5.6. Relationship between TCE HDC reaction activities and bimetallic interaction (Pd-Au and Au-Pd) at different Au loadings under the Dried/Air/H_2 process (dotted line: initial TOF (22×10^{-3} $mol_{TCE}/mol_{Pd}/s$) value of the control Sample P0 Pd/C).

5.3.5. Effect of treatment on catalytic activity

As shown in Fig. 5.2, catalytic activities were influenced by different treatments, even at the same PdAu composition. Such activity changes could be correlated to catalyst nanostructures as EXAFS results revealed. Fig. 5.7 shows proposed catalyst structures under different treatments, as a summary of the following discussion. Fig. 5.8 serves as an example to exhibit relationships among reaction activities, bimetallic interaction (Pd-Au and Au-Pd), and different treatments at the same Au loading (1.1 wt%).

Samples with drying only (A1, A2, A3, A4) showed no bimetallic interaction since the temperature (90 °C) was low and no significant Pd-Au or Au-Pd bonding was observed (Table 5.2); the catalytic activities were slightly promoted (A2, A3) or remained similar to Pd/C (A1, A4) (Table 5.1). EXAFS results (Table 5.2) suggest that Pd helped reduction of Au and underwent a redox reaction with Au; therefore, Pd-Pd became Pd-Cl with increasing Au loadings (A3, A4), and all Au was in the Au-Au form except for A4 which did not have enough metallic Pd^0 atoms to reduce Au, resulting in some Au-Cl bonding. This is in accordance with that Au has a higher reduction potential than Pd ($Au^{3+} + 3\ e^-$ Au^0, $E° = +1.52$ V; $Pd^{2+} + 2\ e^-$ Pd^0, $E° = +0.915$ V [49]). The slightly higher activities for A2 and A3 might be due to promotion from nearby Au^0 atoms. A1 might have too dilute Au^0 atoms, and A4 might have excess Cl^- ions, as mentioned in Sec. 5.3.4, so that Au promotion was not obvious.

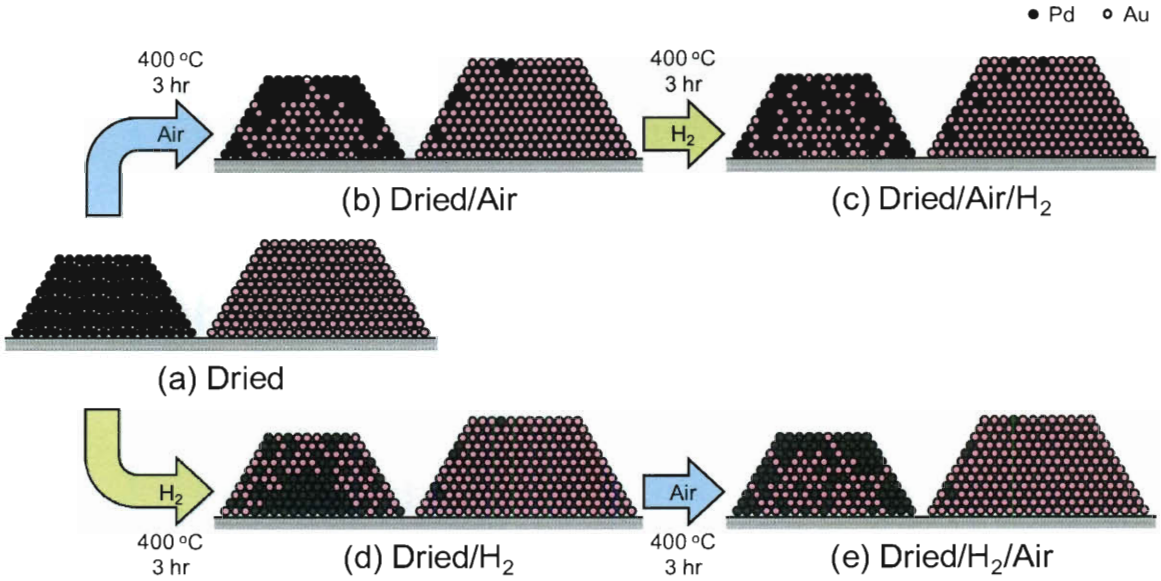

Figure 5.7. Schematic illustration of proposed cross-section structures of PdAu/C samples with different treatments: (a) Dried, (b) Dried/Air, (c) Dried/Air/H_2, (d) Dried/H_2, and (e) Dried/H_2/Air.

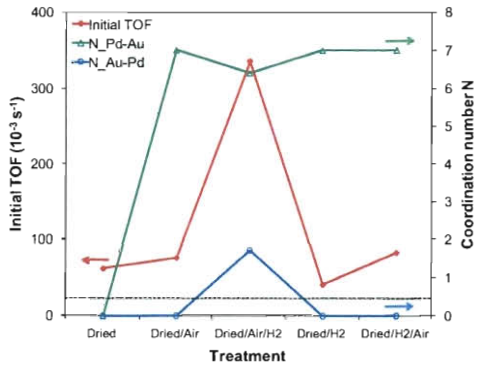

Figure 5.8. Relationship between TCE HDC reaction activities and bimetallic interaction (Pd-Au and Au-Pd) with different treatment processes at the same 1.1 wt% Au loading (dotted line: initial TOF value (22×10^{-3} $mol_{TCE}/mol_{Pd}/s$) of the control Sample P0 Pd/C).

Samples with the Dried/Air process (B1, B2, B3, B4) generally exhibited significant bimetallic interaction (Pd-Au and Au-Pd) and the Au stabilization effect for Pd oxidization resistance. Pd and Au are thermodynamically miscible over the entire composition [50]; thus, it is reasonable to have more bimetallic interaction after high-temperature treatment. B1 did not have detectable Pd-Au and Au-Pd probably due to its

low Au loading. B3 and B4 had Pd-Au but no Au-Pd because most Au presented in the larger Au-rich particles, as mentioned in Sec. 5.3.4; therefore, Au-Pd became even negligible compared to the overwhelming Au-Au at high Au loadings. The Au stabilization effect, also mentioned in Sec. 5.3.4, led to no detectable Pd-O except for B4 with effects from initial excess Cl^- ions. The catalytic activities were promoted for B2 and B3 most likely due to bimetallic interaction. B1, with the low Au loading, remained similar to Pd/C. B4 had a slightly lower activity than Pd/C because of initial excess Cl^- ions and resulting Pd-O and lower Pd-Au.

Samples with the Dried/Air/H_2 process (C1, C2, C3, C4) also had significant bimetallic interaction (Pd-Au and Au-Pd) except for C1 with the low Au loading. C2 and C3 showed both Pd-Au and Au-Pd while C4 did not have Au-Pd due to the larger Au-rich particles. Compared to the Dried/Air samples with only B2 showing both Pd-Au and Au-Pd, the Dried/Air/H_2 process might have the ability to provide better atomic rearrangement between Pd and Au atoms—possible local alloying in H_2 at high temperature, leading to more bimetallic interaction at both Pd-Au and Au-Pd bonding. No oxidized Pd or Au bonding was detected, in accordance with the high-temperature H_2 treatment. The catalytic activities of the Dried/Air/H_2 samples were among the highest at different compositions.

Samples with the Dried/H_2 process (D1, D2, D3, D4) showed Pd-Au bimetallic interaction except for D1 with the low Au loading. No Au-Pd bonding was detected, indicating that most Au atoms formed large Au particles with little interaction with Pd atoms. No oxidized Pd or Au bonding was detected, in accordance with the high-

temperature H_2 treatment. The catalytic activities of the Dried/Air/H_2 samples were slightly higher than Pd/C and similar with each other.

Samples with the Dried/H_2/Air process (E1, E2, E3, E4) showed bimetallic interaction with only Pd-Au for E3 and E4. Like the Dried/H_2 samples, no Au-Pd bonding was detected, indicating that most Au atoms were still in large Au particles with little interaction with Pd atoms. E4 had some Pd-O bonding probably because initial excess Cl^- ions prevented some Pd atoms from contacting Au atoms, leading to less Pd oxidization resistance and similar EXAFS results as B4 with the Dried/Air process. However, different from B4 and other Dried/Air samples, the catalytic activities of the Dried/H_2/Air samples increased with Au loadings, and E4 was the most active one. The explanation for this difference is not understood.

Hilaire et al. reported that PdAu alloy equilibrium would be reached only above 500 °C [51], which was higher than the temperature we used (400 °C). Several researchers observed that, for PdAu materials under high-temperature calcination, Pd tended to be on the outer shell while Au remained in the core because Pd was more readily to be oxidized than Au [20, 51, 52]. Therefore, we speculate that our samples with the air calcination process might have atomic migration to form a Pd-rich shell/Au-rich core structure. On the contrary, samples with the H_2 reduction process should not have such migration since there was no air in the 400-°C treatment; addition of Au should lead to Au atoms deposited on the surface of Pd particles.

In combination with the above discussion, we further summarize the following interpretation of the structure-activity relationships under different treatments. The Dried/Air process led to a possible Pd-rich shell/Au-rich core structure due to atomic

migration in air at high temperature, but the activities did not increase too much. The Dried/Air/H_2 process had the core-shell structure followed by local alloying in H_2 at high temperature, apparently resulting in better bimetallic interaction and the highest activities among all the samples. The Dried/H_2 process made a small amount of Au atoms interact with Pd atoms to form a possible Au-rich shell/Pd-rich core structure since heating in H_2 would not have atomic migration as in calcination; the activities were only slightly promoted and similar among different compositions since fewer Pd atoms were on the surface, leading to fewer active sites and offsetting Au promotion. The Dried/H_2/Air process might increase surface Pd amount due to atomic migration in calcination; so the activities became higher than the Dried/H_2 samples. As shown in Fig. 5.8, different treatments might lead to similar bimetallic interaction but also very different reaction activities, which could be explained by the above analysis. Nevertheless, further characterization including chemisorption (with H_2 or CO as probe molecules) and advanced electron microscopy should be considered to support this work.

5.4. Conclusions

Bimetallic supported PdAu catalysts, by adding gold salt to existing supported Pd catalysts, were investigated for the higher activities and corresponding nanostructures. Bimetallic PdAu/C catalysts were successfully synthesized with well-established industrial processes of catalyst manufacture, including impregnation, drying, calcination, and reduction, which are commercially viable for large scale production. Systematic studies about different compositions and treatments revealed more information of catalytic performance and nanostructure. The most active PdAu/C catalyst (Pd 1.0 wt%,

Au 1.1 wt%, Dried/Air/H_2 process, initial TOF = 340 × 10^{-3} $mol_{TCE}/mol_{Pd}/s$) showed an activity for >15 times higher than Pd/C (Pd 1.0 wt%, initial TOF = 22 × 10^{-3} $mol_{TCE}/mol_{Pd}/s$), with the room-temperature, aqueous-phase TCE HDC as the model reaction. TEM images indicated that PdAu/C catalysts might have a bimodal size distribution with smaller particles around 5-10 nm and larger particles around 30-100 nm. XAS results further suggested that larger particles might be Au-rich particles and bimetallic interaction might occur mainly at smaller particles. Au could stabilize metallic Pd and prevent Pd from being oxidized even under calcination at 400 °C; however, initial excess Cl^- ions would depress this stabilization effect. Nanostructure models were proposed for effects of Au loading and treatment, in accordance with EXAFS data and catalytic results, exhibiting the structure-activity relationships. Among all the treatments tested, the Dried/Air/H_2 process led to a probable Pd-rich shell/Au-rich core structure with higher bimetallic interaction and the most active catalytic performance.

5.5. References

[1] G. Schmid, A. Lehnert, J.O. Malm, J.O. Bovin, Angew. Chem.-Int. Edit. Engl. 30 (1991) 874-876.

[2] G. Schmid, H. West, J.O. Malm, J.O. Bovin, C. Grenthe, Chem.-Eur. J. 2 (1996) 1099-1103.

[3] N. Toshima, M. Harada, Y. Yamazaki, K. Asakura, J. Phys. Chem. 96 (1992) 9927-9933.

[4] M. Harada, K. Asakura, N. Toshima, J. Phys. Chem. 97 (1993) 5103-5114.

[5] Y. Wang, N. Toshima, J. Phys. Chem. B 101 (1997) 5301-5306.

[6] M.R. Knecht, M.G. Weir, A.I. Frenkel, R.M. Crooks, Chem. Mat. 20 (2008) 1019-1028.

[7] M.G. Weir, M.R. Knecht, A.I. Frenkel, R.M. Crooks, Langmuir 26 (2010) 1137-1146.

[8] C.L. Bianchi, P. Canton, N. Dimitratos, F. Porta, L. Prati, Catal. Today 102 (2005) 203-212.

[9] J.A. Lopez-Sanchez, N. Dimitratos, P. Miedziak, E. Ntainjua, J.K. Edwards, D. Morgan, A.F. Carley, R. Tiruvalam, C.J. Kiely, G.J. Hutchings, Phys. Chem. Chem. Phys. 10 (2008) 1921-1930.

[10] L. Kesavan, R. Tiruvalam, M.H. Ab Rahim, M.I. bin Saiman, D.I. Enache, R.L. Jenkins, N. Dimitratos, J.A. Lopez-Sanchez, S.H. Taylor, D.W. Knight, C.J. Kiely, G.J. Hutchings, Science 331 (2011) 195-199.

[11] H. Bonnemann, U. Endruschat, B. Tesche, A. Rufinska, C.W. Lehmann, F.E. Wagner, G. Filoti, V. Parvulescu, V.I. Parvulescu, Eur. J. Inorg. Chem. (2000) 819-822.

[12] R.W.J. Scott, C. Sivadinarayana, O.M. Wilson, Z. Yan, D.W. Goodman, R.M. Crooks, J. Am. Chem. Soc. 127 (2005) 1380-1381.

[13] P. Dash, T. Bond, C. Fowler, W. Hou, N. Coombs, R.W.J. Scott, J. Phys. Chem. C 113 (2009) 12719-12730.

[14] K.D. Beard, D. Borrelli, A.M. Cramer, D. Blom, J.W. Van Zee, J.R. Monnier, ACS Nano 3 (2009) 2841-2853.

[15] J. Rebelli, M. Detwiler, S. Ma, C.T. Williams, J.R. Monnier, J. Catal. 270 (2010) 224-233.

[16] F. Pinna, Catal. Today 41 (1998) 129-137.

[17] J. Regalbuto (Ed.), Catalyst Preparation: Science and Engineering. CRC Press, Boca Raton, FL, 2006.

[18] D.I. Enache, J.K. Edwards, P. Landon, B. Solsona-Espriu, A.F. Carley, A.A. Herzing, M. Watanabe, C.J. Kiely, D.W. Knight, G.J. Hutchings, Science 311 (2006) 362-365.

[19] G.J. Hutchings, Chem. Commun. (2008) 1148-1164.

[20] A.A. Herzing, A.F. Carley, J.K. Edwards, G.J. Hutchings, C.J. Kiely, Chem. Mat. 20 (2008) 1492-1501.

[21] J.C. Pritchard, Q. He, E.N. Ntainjua, M. Piccinini, J.K. Edwards, A.A. Herzing, A.F. Carley, J.A. Moulijn, C.J. Kiely, G.J. Hutchings, Green Chem. 12 (2010) 915-921.

[22] T. Ressler, J. Synchrot. Radiat. 5 (1998) 118-122.

[23] F.W. Lytle, D.E. Sayers, E.A. Stern, Physica B 158 (1989) 701-722.

[24] M.O. Nutt, K.N. Heck, P. Alvarez, M.S. Wong, Appl. Catal. B-Environ. 69 (2006) 115-125.

[25] K.N. Heck, M.O. Nutt, P.J.J. Alvarez, M.S. Wong, J. Catal. 267 (2009) 97-104.

[26] Y.-L. Fang, J.T. Miller, N. Guo, K.N. Heck, P.J.J. Alvarez, M.S. Wong, Catal. Today 160 (2011) 96-102.

[27] R.P. Schwarzenbach, P.M. Gschwend, D.M. Imboden, Environmental Organic Chemistry. Wiley, Hoboken, NJ, 1993.

[28] G.V. Lowry, M. Reinhard, Environ. Sci. Technol. 33 (1999) 1905-1910.

[29] M.O. Nutt, J.B. Hughes, M.S. Wong, Environ. Sci. Technol. 39 (2005) 1346-1353.

[30] K. Mackenzie, H. Frenzel, F.D. Kopinke, Appl. Catal. B-Environ. 63 (2006) 161-167.

[31] J.C. Liu, F. He, E. Durham, D.Y. Zhao, C.B. Roberts, Langmuir 24 (2008) 328-336.

[32] Y.-L. Fang, K.N. Heck, P.J.J. Alvarez, M.S. Wong, ACS Catalysis 1 (2011) 128-138.

[33] G.V. Lowry, M. Reinhard, Environ. Sci. Technol. 34 (2000) 3217-3223.

[34] S. Ordonez, B.P. Vivas, F.V. Diez, Appl. Catal. B-Environ. 95 (2010) 288-296.

[35] J.T. Miller, M.K. Neylon, C.L. Marshall, A.J. Kropf, in: C.I. Contescu, K. Putyera, (Eds.), Dekker Encyclopedia of Nanoscience and Nanotechnology, CRC Press, Boca Raton, FL, 2004, 3953-3972.

[36] G. Vlaic, D. Andreatta, P.E. Colavita, Catal. Today 41 (1998) 261-275.

[37] G. Meitzner, Catal. Today 39 (1998) 281-291.

[38] J.H. Sinfelt, Accounts Chem. Res. 20 (1987) 134-139.

[39] J.S. Bradley, G.H. Via, L. Bonneviot, E.W. Hill, Chem. Mat. 8 (1996) 1895-1903.

[40] A. Frenkel, Z. Kristall. 222 (2007) 605-611.

[41] W.C. Ketchie, M. Murayama, R.J. Davis, J. Catal. 250 (2007) 264-273.

[42] C.H. Chen, L.S. Sarma, J.M. Chen, S.C. Shih, G.R. Wang, D.G. Liu, M.T. Tang, J.F. Lee, B.J. Hwang, ACS Nano 1 (2007) 114-125.

[43] S.M. Oxford, P.L. Lee, P.J. Chupas, K.W. Chapman, M.C. Kung, H.H. Kung, J. Phys. Chem. C 114 (2010) 17085-17091.

[44] R.J. Davis, M. Boudart, J. Phys. Chem. 98 (1994) 5471-5477.

[45] S.N. Reifsnyder, H.H. Lamb, J. Phys. Chem. B 103 (1999) 321-329.

[46] A. Carrasquillo, J.J. Jeng, R.J. Barriga, W.F. Temesghen, M.P. Soriaga, Inorg. Chim. Acta 255 (1997) 249-254.

[47] J.T. Miller, A.J. Kropf, Y. Zha, J.R. Regalbuto, L. Delannoy, C. Louis, E. Bus, J.A. van Bokhoven, J. Catal. 240 (2006) 222-234.

[48] M.W. Tew, J.T. Miller, J.A. van Bokhoven, J. Phys. Chem. C 113 (2009) 15140-15147.

[49] A.J. Bard, L.R. Faulkner, Electrochemical Methods: Fundamentals and Applications. Wiley, Hoboken, NJ, 2001.

[50] J.H. Sinfelt, Bimetallic Catalysts. Wiley, Hoboken, NJ, 1983.

[51] L. Hilaire, P. Legare, Y. Holl, G. Maire, Surf. Sci. 103 (1981) 125-140.

[52] Y. Shiraishi, D. Ikenaga, N. Toshima, Aust. J. Chem. 56 (2003) 1025-1029.

Chapter 6

Recommendations for Future Work

6.1. Recommendations for future work

Structure-property relationships for palladium-gold (PdAu) nanoparticle (NP) catalysts in water-phase reactions, with hydrodechlorination (HDC) of trichloroethene (TCE) as the model reaction, were investigated and addressed in this thesis. The geometric effect, in which Pd ensembles on the Au NP surface act as major active sites, was demonstrated to dominate over other effects like the electronic effect or the mix metal site effect for the bimetallic enhancement. Kinetics analysis and reaction mechanism of TCE HDC with Pd-based NPs were developed; a Langmuir-Hinshelwood model was proposed and evaluated to be more appropriate than the previous first-order model. A new way to promote Pd catalysis by post-impregnation of gold salt was explored; structure and catalytic performance of PdAu catalysts could be controlled by heat treatment. Following this work, several unrevealed scientific issues and novel application approaches are recommended for future effort, including surface characterization, material visualization, in-situ observation, environmental practice, and further application. Continuing work and collaboration in these aspects are being conducted in the Wong research group.

X-ray absorption spectroscopy (XAS) revealed the local atomic environment of catalysts, which led to the conclusion that Pd ensembles on the Au NP surface were

important for TCE HDC. A next question coming out thereafter would be how the configuration of surface ensembles is. While XAS might not provide much information about the catalyst surface, characterization techniques with molecule probes could be helpful to unveil it. Chemisorption with H_2 and infrared spectroscopy with CO as the probe molecule can provide direct measurements of surface Pd atoms, in terms of surface Pd amounts and surface Pd ensemble configuration (size, shape, etc) [1-3]. Such information could be useful to understand more about the structure of active sites, and correlate to the findings in this work.

On the other hand, it is true that images give more clear explanation than words. Good visualization can provide better understanding and lead to precious insight. Visualization techniques, such as advanced electron microscopy (like scanning transmission electron microscopy, STEM), elemental mapping, and three-dimensional morphology, could lead to more vivid and intuitive expression of catalyst structure [4, 5].

The Langmuir-Hinshelwood model for TCE HDC was established in this work. To know more about the reaction mechanism, especially down to the molecule level, in-situ observation via XAS could be very helpful. XAS can monitor changes of bondings and adsorbed molecules on the catalyst surface under reaction conditions, which could help verify or modify the reaction mechanism [6, 7].

For the environmental practice, long-term continuous flow reactor testing with PdAu catalysts is currently underway in the Wong group. Flow reactor systems for lab scale and real field tests are both being constructed. While PdAu catalysts have been shown to be active for TCE, the Wong group is extending target compounds to other

chlorinated hydrocarbons, including tetrachloroethylene (perchloroethene, PCE) and chloroform. Studies of deactivation and regeneration are also being investigated.

The advantages of PdAu catalysts detailed in this thesis could have the potential to be applied to other desired reactions. In addition to environmental pollution control, possible applications include selective oxidation of hydrocarbons [8-15], direct synthesis of hydrogen peroxide (H_2O_2) [16-18], and fuel cells [19-23]. The Wong group has started exploring several cases.

6.2. References

[1] F. Maroun, F. Ozanam, O.M. Magnussen, R.J. Behm, Science 293 (2001) 1811-1814.

[2] H.G. Lang, S. Maldonado, K.J. Stevenson, B.D. Chandler, J. Am. Chem. Soc. 126 (2004) 12949-12956.

[3] J. Rebelli, M. Detwiler, S. Ma, C.T. Williams, J.R. Monnier, J. Catal. 270 (2010) 224-233.

[4] I. Arslan, J.C. Walmsley, E. Rytter, E. Bergene, P.A. Midgley, J. Am. Chem. Soc. 130 (2008) 5716-5719.

[5] K.D. Beard, D. Borrelli, A.M. Cramer, D. Blom, J.W. Van Zee, J.R. Monnier, ACS Nano 3 (2009) 2841-2853.

[6] B.R. Fingland, F.H. Ribeiro, J.T. Miller, Catalysis Letters 131 (2009) 1-6.

[7] N. Guo, B.R. Fingland, W.D. Williams, V.F. Kispersky, J. Jelic, W.N. Delgass, F.H. Ribeiro, R.J. Meyer, J.T. Miller, Phys. Chem. Chem. Phys. 12 (2010) 5678-5693.

[8] M.S. Chen, D. Kumar, C.W. Yi, D.W. Goodman, Science 310 (2005) 291-293.

[9] W.C. Ketchie, M. Murayama, R.J. Davis, J. Catal. 250 (2007) 264-273.

[10] C. Della Pina, E. Falletta, L. Prati, M. Rossi, Chem. Soc. Rev. 37 (2008) 2077-2095.

[11] D. Wang, A. Villa, F. Porta, L. Prati, D.S. Su, J. Phys. Chem. C 112 (2008) 8617-8622.

[12] A. Villa, N. Janjic, P. Spontoni, D. Wang, D.S. Su, L. Prati, Appl. Catal. A-Gen. 364 (2009) 221-228.

[13] A. Villa, D. Wang, D.S. Su, G.M. Veith, L. Prati, Phys. Chem. Chem. Phys. 12 (2010) 2183-2189.

[14] J.S. McPherson, D.T. Thompson, Top. Catal. 52 (2009) 743-750.

[15] L. Kesavan, R. Tiruvalam, M.H. Ab Rahim, M.I. bin Saiman, D.I. Enache, R.L. Jenkins, N. Dimitratos, J.A. Lopez-Sanchez, S.H. Taylor, D.W. Knight, C.J. Kiely, G.J. Hutchings, Science 331 (2011) 195-199.

[16] G.J. Hutchings, Chem. Commun. (2008) 1148-1164.

[17] J.K. Edwards, B. Solsona, E.N. N, A.F. Carley, A.A. Herzing, C.J. Kiely, G.J. Hutchings, Science 323 (2009) 1037-1041.

[18] J.C. Pritchard, Q. He, E.N. Ntainjua, M. Piccinini, J.K. Edwards, A.A. Herzing, A.F. Carley, J.A. Moulijn, C.J. Kiely, G.J. Hutchings, Green Chem. 12 (2010) 915-921.

[19] M.H. Shao, T. Huang, P. Liu, J. Zhang, K. Sasaki, M.B. Vukmirovic, R.R. Adzic, Langmuir 22 (2006) 10409-10415.

[20] J. Zhang, K. Sasaki, E. Sutter, R.R. Adzic, Science 315 (2007) 220-222.

[21] J.B. Xu, T.S. Zhao, S.Y. Shen, Y.S. Li, Int. J. Hydrog. Energy 35 (2010) 6490-6500.

[22] V. Mazumder, Y. Lee, S.H. Sun, Adv. Funct. Mater. 20 (2010) 1224-1231.

[23] C.J. Zhong, J. Luo, B. Fang, B.N. Wanjala, P.N. Njoki, R. Loukrakpam, J. Yin, Nanotechnology 21 (2010).